Dynamics of Convective Structures at the Solar Photosphere

Takayoshi OBA

Space and Astronautical Science, School of Physical science, SOKENDAI

Abstract

We investigated the dynamics of the solar granulation by using the bisector analysis with high-spatial and temporal spectral data obtained by *Hinode* satellite.

The solar photosphere is a visible surface of the Sun, where numerous numbers of bright granules, called granulation, are observed anywhere. The granules are surrounded by dark narrow channels, called intergranular lanes. The granulation is a manifestation of the gas convection, which takes an important role to transfer the energy from the interior to the solar surface, the photosphere. The recent high-resolution observations suggest that each granule evolves in more complicated dynamical processes, but we are lack of knowledge on details of the dynamical processes in those gas convection.

One of missing but critical observational knowledge is dynamical behaviors of the gas in the direction vertical to the solar surface. However, there are three difficulties for investigation. First, it is difficult to derive the velocity field at different height. Second, lower spatial resolution degrades the signal of Doppler shift. Third, in addition to convective velocity, global oscillatory motion is included in the velocity field. To solve these problems, I used the bisector analysis to determine the Doppler velocity as a function of the vertical direction in the formation layer of a spectral line emerging from the photosphere. Next, I separate the derived velocity field into pure convective motion and 5-min oscillations which is a global eigenmode of the compressive sound wave. These methods were applied to high-cadence time series of an Fe I spectral lines at 630.15 nm with high spatial resolution, acquired with the *Hinode* / Solar Optical Telescope.

With the derived time-distance diagrams of velocities, I found several properties of the velocity structures of convection, as summarized below. i) Upflow velocity field in granule is kept alive for the duration much longer than 10 minutes. ii) The number distribution of convective vertical velocities shows larger asymmetry toward the upward (or blue-shifted wavelength) direction, as going to the higher portion of the photosphere. iii) The RMS of downward velocity increases from 0.2 km/s to 0.6 km/s with depth.

The finding i) suggests that hot upward materials are successively supplied from below the photosphere, and it forms granules. ii) suggests the following phenomenological picture: The strong upward velocity in bright granule reaches the higher portion of the atmosphere with less decreasing of the upward velocity. iii) means that intergranular lanes cannot be explained by the standard solar model. The photosphere in the standard model is regarded as a convective stable layer, which decelerates the downward motion. One following scenario can explain this: Radiative cooling materials tend to become high density and are more pulled down by gravity, resulting in accelerating downward motion.
These dynamical properties of the gas convection given in findings i) - iii) have not been investigated so far. In particular, we succeeded in newly finding the difference of convective structure between at granules and intergranular lanes.

The RMS velocity of separated 5-min oscillations by our method increases with height from 0.3 km/s to 0.4 km/s. These values are consistent with previous works. The amplitude of 5-min oscillations is increased because of the density decreasing with height.

Using the pure convective motion with high time resolution data, we newly found the common character of dynamical evolution near the center of fragmenting granules. A downward motion appears at higher layer and it is extended toward the lower layer in less than 30 second which is very short period, and at the same time, a dark area appears in the continuum images. This represents that the radiative cooling works more effectively at higher layer, resulting in the first appearance of a downward gas flow near the center of granules and subsequent development of a downflow in the entire range of the line formation layer in a short timescale.

Acknowledgement

I am deeply grateful to my supervisor, Assoc. prof. T. Shimizu. He continues to gives insightful comments and suggestions. Without his guidance and persistent help this master thesis would not have been possible.

Y. Iida gives me constructive comments and warm encouragement. My deep heartfelt appreciation goes to him.

I would like to express my gratitude to Assoc. prof. T. Sakao, T. J. Okamoto, K. Watanabe, T. Matsumoto and K. S. Lee for giving me useful comments or taught me analysis. I acknowledge H. Uitenbroek, T. Sekii and N. E. Hurlburt for discussions. I have had the support and encouragement of K. Daiguzi, Y. Bamba, R. Kanoh and Y. Kawabata. I also wish to express my thanks to all members at laboratory, and Space and Astronautical Science, School of Physical science, SOKENDAI.

Hinode is a Japanese mission developed and launched by ISAS/JAXA, collaborating with NAOJ as a domestic partner, NASA and STFC (UK) as international partners. Scientific operation of the *Hinode* mission is conducted by the *Hinode* science team organized at ISAS/JAXA. This team mainly consists of scientists from institutes in the partner countries. Support for the post-launch operation is provided by JAXA and NAOJ (Japan), STFC (U.K.), NASA, ESA, and NSC (Norway).

Contents

Chapter 1

Introduction

1.1 The solar photosphere

The solar photosphere is a surface observed in the visible light, where well-known dark features, namely sunspots, may be observed on the monotonous bright disk, as seen in Fig. 1.1. High spatial resolution observations show that the monotonous solar disk is covered by *granules*, which can be identified in an enlarged view of the photosphere (Fig. 1.2).

On the photosphere, the granules are bright patterns surrounded by dark channels called intergranular lanes. The size of granules is typically 1.0", while the width of intergranular lanes is 0.3 "(Roudier & Muller 1986). Granules continuously change their shape and repeat the birth and disappearance. Their typical lifetime is 6-12 minutes (Title et al. 1986, Dialetis et al. 1986). Their temperature is around 6000 K. Large aperture telescopes are needed to observe the granules and interegranular lanes separately. The spectroscopic data from the large aperture telescopes has taken essential roles in unveiling the dynamical behaviors of granules (Hirzberger et al. 1997, Berrilli et al. 1999, Roudier et al. 2003). Upflow velocities are well observed inside granules, whereas downflow velocities exist in intergranular lanes. Both velocities are around 1 km s^{-1}. The granules are a manifestation of gas convection at the photosphere. The convection is the main physical mechanism to transfer the solar energy from the outer part of the interier to the photosphere. The energy flux the turbulent convective flows have is roughly 10^8 erg cm^{-2} s^{-1}, which is estimated by $F = \rho\langle\delta v^2\rangle\langle\delta v\rangle$, where averaged turbulent velocity on the solar surface $\langle\delta v\rangle$ is 1 km s^{-1}, and photospheric density ρ is 10^{-7} g cm^{-3}.

The gas convection is dominant in the outer part of the interior, which is called convection zone. In this layer, some parcels overshoot to the convective stable layer with their energy. They reach the photosphere and spread around horizontally, where the dynamical behaviors of granules can be observed with telescopes. The photosphere is a thin layer which meats convective stability condition so that it serves to moderate the vertical convective motion at the solar surface and strengthen the horizontal motion. The temperature of convective hot gas is gradually decreased by radiative cooling, as it goes toward the upper atmosphere. Subsequently the gas is turned back to the deeper layers in the photosphere. Hence, most energy is dissipated on the photosphere.

Even though at the most of the transferred energy is dissipated by radiation, high temperature atmosphere exists above the photosphere. While the photosphere has 6,000 K, the temperature is increased to 10, 000 K in the chromosphere and it is suddenly jumped over 10^6 K in the corona. The energy is supplied by non-thermal ways to maintain the temperature of the chromosphere and the corona. Since the photosphere has much amount of turbulent energy, some part of its energy is used to heat the upper atmosphere. It is at least certain that the magnetic field may be a career of gas convective energy to upper atmosphere, because the upper atmosphere have much amount of magnetic energy and less amount of gas pressure. Many people have tried to detect this process and suggested two candidates. One is the magnetohydrodynamics wave. Gas flows continuously shakes lines of magnetic force on their foot in the photosphere and it is propagated to upper atmosphere with their energy. Arriving at the corona, energy is efficiently released to heat the corona. Another is *nanoflare*. The feet of lines of magnetic force on the photosphere are continuously twisted and bended. Their configurations in the corona are entangled with each other. Complicated configuration tends to cause the small energy release called as nanoflare, leading to heat the corona everywhere. However, this process still remains unidentified. The physical links from the energy inputs by the convective motion to the heating of the upper atmosphere are the area where we have poorly understood observationally.

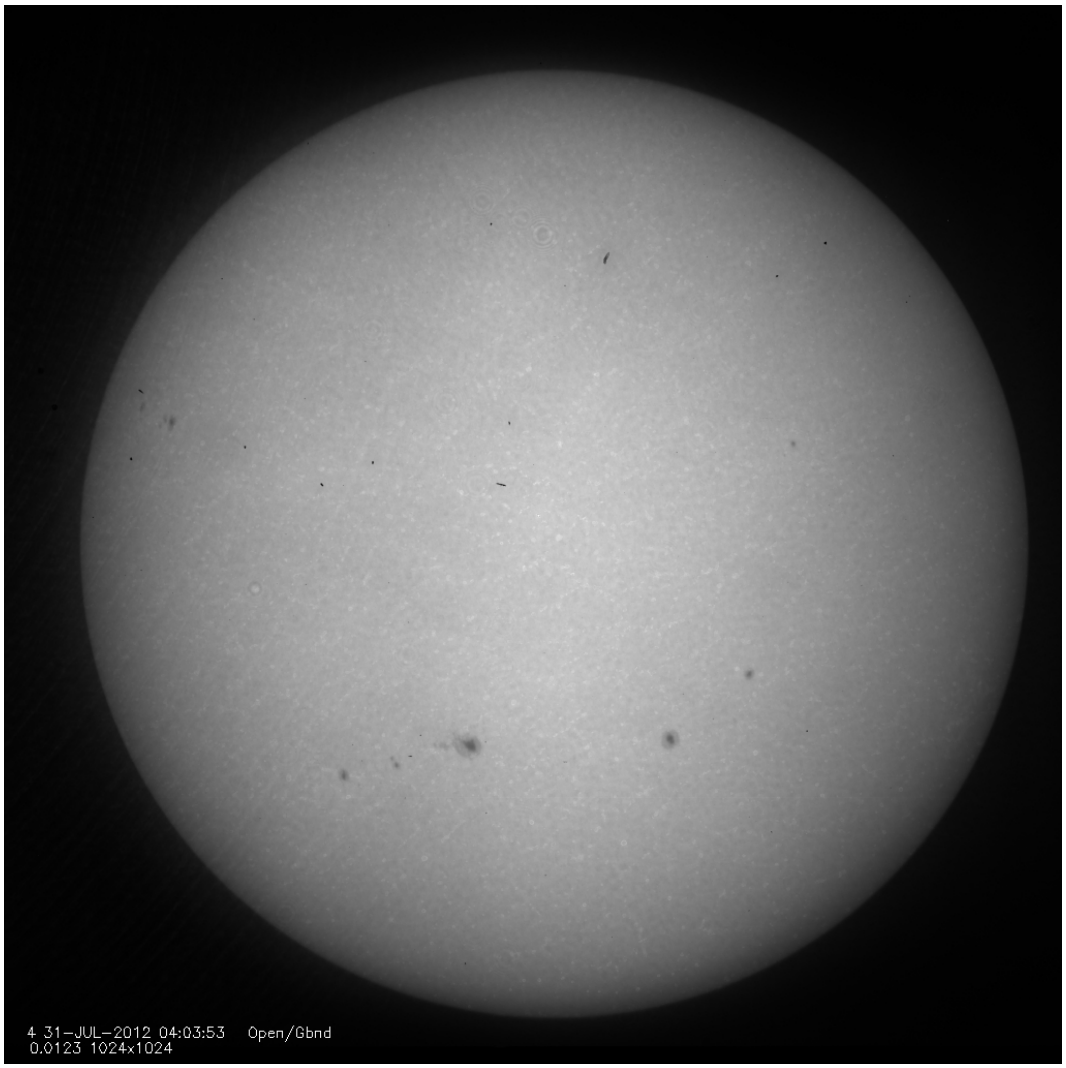

Figure 1.1: The sun observed *XRT* with the G-band on the *Hinode* spacecraft (http://hinode.nao.ac.jp/user/yaji/hinode/issho/).

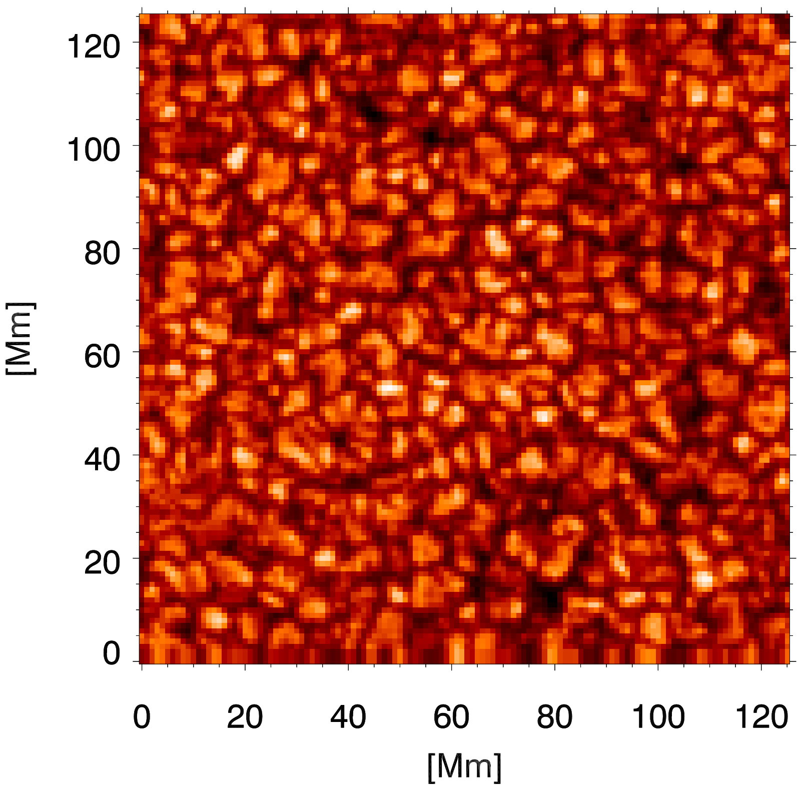

Figure 1.2: The photosphere observed by *Hinode* spacecraft. Bright patterns are granules, separated dark channels are intergranular lanes.

1.2 The solar granulation

Vertical structure is important for the convective stability. I want to begin from the basic theory of convective instability. Let us consider the situation that a gas parcel travels along vertical distance δr (Fig. 1.3). We put the density of parcel is ρ^*, and the density of environment is ρ_0^*. We assume the parcel behaves as adiabatic. Under the adiabatic condition, gas parcels locally adjust their internal pressure without interchanging the heat with surrounding environment. When gas parcel moves at $r + \delta r$, the density difference becomes $\rho^* - \rho_0^*$, which is a critical value as convective stability. When $\rho^* - \rho_0^*$ is negative, moving medium continue to ascend, which is convective instability. On the other hand, positive value in $\rho^* - \rho_0^*$ means that moving medium goes back to original center. At the first order approximation, ρ_* and ρ_0^* can be evaluated as $\delta r(d\rho/dr)_{adi}$ and $\delta r(d\rho/dr)$.

Thus, the condition for instability is

$$\rho^* - \rho_0^* = \delta r \left[\left(\frac{d\rho}{dr} \right)_{adi} - \frac{d\rho}{dr} \right] < 0, \tag{1.1}$$

where $(d\rho/dr)_{adi}$ is the density gradient under the adiabatic condition. If the parcel behaves as a perfect gas, $P = \rho RT/\mu$ is satisfied, T is temperature, the R is gas constant and μ is a mean molecular weight. Pressure equilibrium is assumed, ρ depends only on T. As a result, $(d\rho/dr)_{adi}$ and $(d\rho/dr)$ in (1.1) can be transformed, and we can derive the Schwarzschild criterion for convective instability,

$$\frac{dT}{dr} < \left(\frac{dT}{dr} \right)_{adi} \tag{1.2}$$

where $(dT/dr)_{adi}$ is the temperature gradient under adiabatic condition. It is clear from (1.2) that the vertical structure contributes to determine whether the layer is convective stable or not.

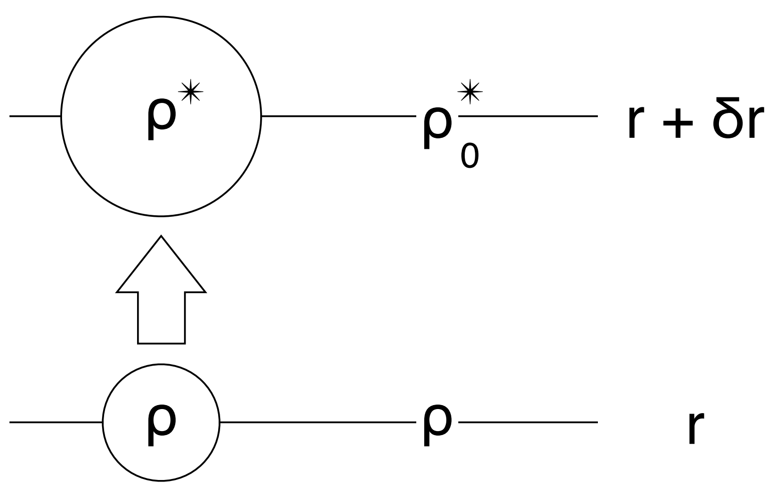

Figure 1.3: Schematic diagram of convective motion.

In the solar outer zone of 30% of the interior, the stratification satisfies the Schwarzschild criterion and is in the condition of convective unstable state. The temperature gradient becomes smaller toward the outer of the sun. It finally becomes convective stable at the solar photosphere. The convection overshoots the photosphere, and it is decelerated in the convective stable layer. After that, ascending materials are spread around horizontally, and this motion of hot gas is seen as bright cellular patterns.

Previous studies provided us with interpretation about convective motion at the photosphere. When a spectroscopic data including absorption lines formed at the photosphere is obtained, the spatial distribution of the Doppler velocity field is following: The absorption lines typically shifts toward shorter wavelength in granular regions, where high irradiance in the continuum. On the other hand, it shifts toward longer wavelength in intergranular lanes. The Doppler effect causes to shift these lines in wavelength (this phenomena will be treated on Sect.3.1). While there are hot ascending materials are located in granular region, descending materials are in intergranular lane. This reflects a phenomena that hot materials arising from below the photosphere forms a granule, and a relatively cold materials after going through radiative cooling go back into the below the photosphere (Fig. 1.4). These conventional interpretations of the solar convection has been widely accepted. Three-dimensional RMHD numerical simulations succeeded in reproducing the solar granulation. Moreover, recent technological improvement of large capacity for calculation enables numerical simulations to unveil granular dynamics including substructure where we cannot directly observe. Stein & Nordlund (1998) reproduced the dynamics of granulation (*Right* of Fig. 1.5). From their simulations, hot materials rise up in the granules, become cool though radiative cooling, diverge horizontally and back down pulled by gravity in the intergranular lanes (*Left* of Fig. 1.5).

Vertical structure is important for understanding the convective structure. Numerical simulations have provided us with some insights into the three-dimensional velocity structures. In contrast, we are lack of knowledge from observations on the velocity structures in the direction vertical to the surface, although there are numerous numbers of knowledge on the two-dimensional spatial distribution at a layer and its temporal evolution. There are three main difficulties to investigate the convective vertical structure. One difficult point is that it is difficult to derive the velocity field at different height. Second is achieving the high spatial resolution, because unresolved data degrades the signal of Doppler shift by blending blue shifted line formed in granular region and red shifted one in intergranular region.

Third is separating the signal of 5-min oscillations form velocity field. This oscillatory motion, a global eigenmode of the compressive sound wave, will be described in next section.

There are mainly two way to investigate the velocity field at different height. One is the way to use the multiple line analysis (Durrant et al. 1979 and Berrilli et al. 2002), because each line reflects different heights. Kiefer et al. 2000 show some results of vertical RMS (root-mean squares) velocity from multiple lines (Fig. 1.6). Using several lines formed at different heights respectively, they surveyed the vertical velocity field. They suggested a tendency of vertical RMS velocity to decrease with height. This method is, however, poor in continuity with height, because the coverage by the absorption lines has gaps at some heights. This method cannot observes those lines simultaneously because the observations need a fairly long time to switch one filter to another filter.

Another method is *bisector analysis* of a single spectral line. This analysis is based on the fact that the light at each wavelength position in the spectral line profile reflects a different height (see Sect.3.1). Its advantage is that we can obtain vertical structure at exactly same time using a spectral data, and the series of spectral data provides the temporal evolution of velocity structures in the vertical direction easily. However, this bisector analysis requires the high signal-to-noise spectral data, because it derives the vertical velocity at different heights from the line profile. With observations from large telescopes, a few authors derived vertical velocity. Using a ground-based telescope, Maltagliati & Righini (2003) reported the different character of line asymmetry at granular region and intergranular region. They captured decelerating upflow in granular region. On the other hand, in intergranular region, velocity fields are constant over height. Kostik & Khomenko (2007) investigated convective structure over 570 km on granular region and intergranular lane by using two Fe II 523.4 and Fe I 639.3 nm lines recorded simultaneously at the German Vacuum Tower telescope in Tenerife (VTT) . They have not found the typical velocity value difference between granular and intergranular region over height. Kostik et al. (2009) investigated convective structure by using Ba II 455.4 nm. This observation was done at the VTT. They reported that maximum of the number distribution of both velocity and intensity appears at 650-700 km granular size. Moreover, they found 40% of upflow preserving over 650 km.

However, observation with high spatial resolution is required to derive convective structure accurately. The past observations are based on ground-based telescopes, which are significantly affected by atmospheric seeing. Granule has typically the size larger than 1.0 ″, whereas intergranular lane is a narrow channel with the width less than 0.3 ″. Although a few recent ground-based telescopes have a larger aperture and attains the diffraction limit less than 0.5 ″, the atmospheric seeing effect degraded their spatial resolution to around from 0.3 ″ to 0.7 ″. Thus, it needs a high spatial resolution to distinguish velocity field between granular and intergarnular region. Basically, in the past the asymmetry of the spectral line profiles had been interpreted as a result of summation of spectral lines from granule and intergranular lane (Fig.1.7). Blue shifted line is formed on granular region and red shifted line is originated on intergranular region, assembling an asymmetric line when they are observed in a single pixel. With a spectral line formed by the spatial summation of spectral lines from granular and intergranular regions, we cannot derive wavelength shift for each of the region. The spatial resolution in order of 0.3" or better is a crucial point in studying granule and inter granular lane separately on the photosphere.

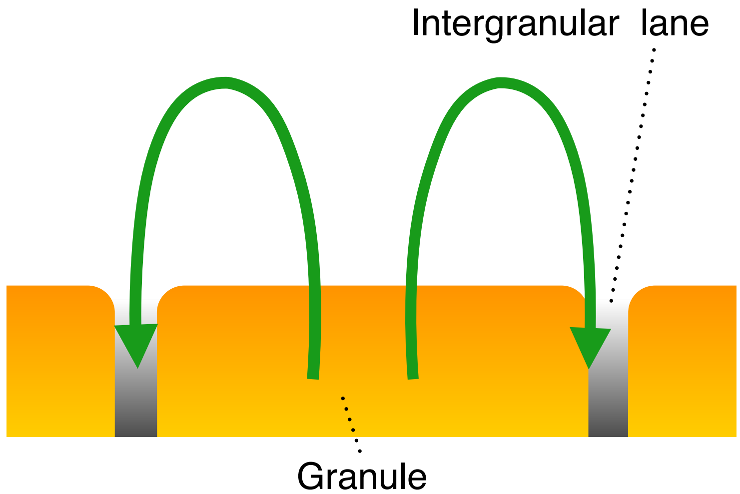

Figure 1.4: Schematic diagram of stationary convection. Arriving at the photosphere, ascending hot materials are decelerated and move to horizontal direction. After radiative cooling, it descends to subsurface.

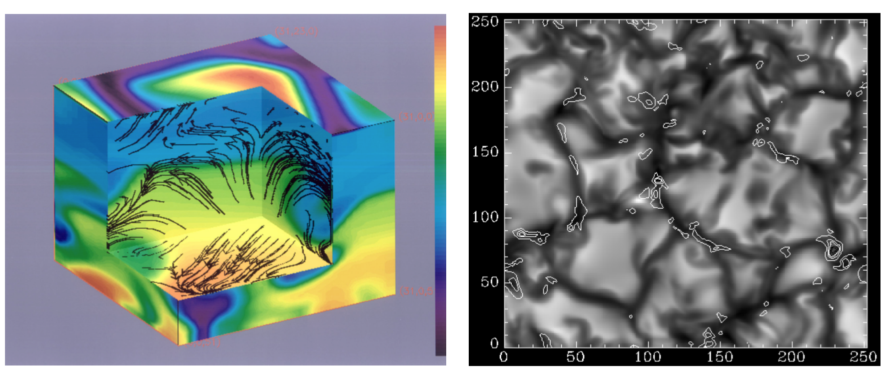

Figure 1.5: A numerical simulation of solar granulation (Stein & Nordlund 1998). *Left*: Velocity field in arrow and temperature structure in colored (blue = cool, red=hot). *Right*: An image of the intensity.

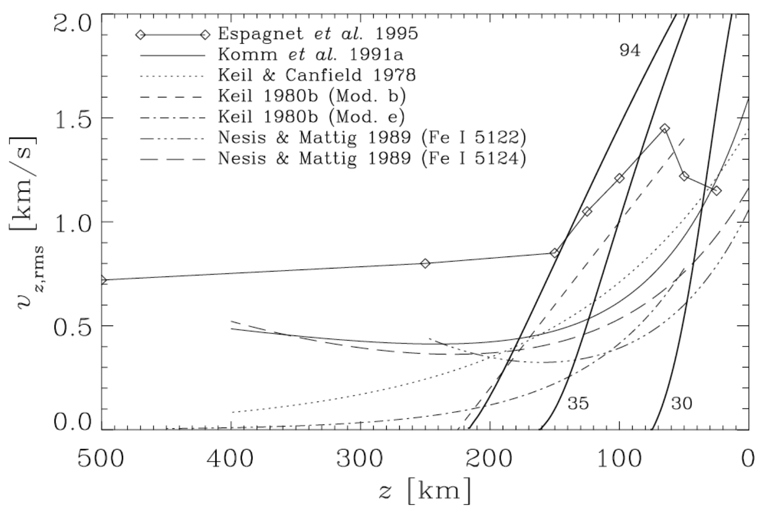

Figure 1.6: Vertical RMS velocity as a function of height (Kiefer et al. 2000).

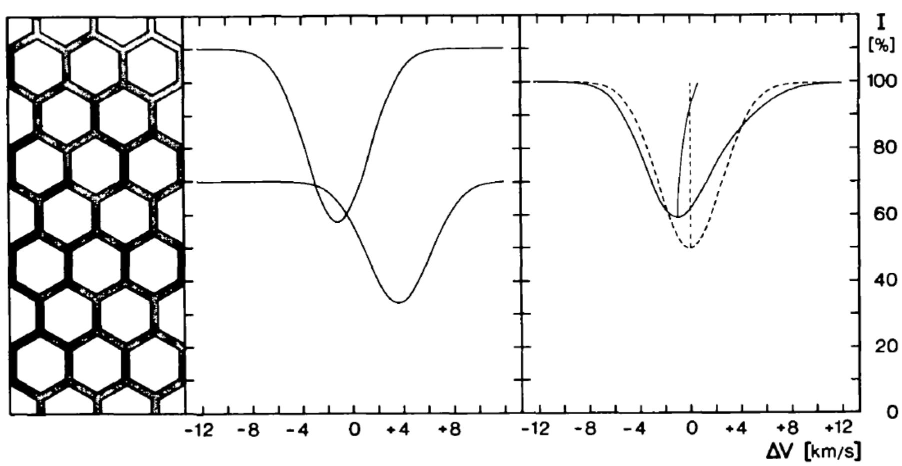

Figure 1.7: Process of how to form line asymmetry in the past (Dravins et al. 1981). *Left*: Spatial distribution on the photosphere. Regular hexagonal granular shape accounts for 75% of whole region separated narrow intergranular lane whose area is 25%. *Middle*: Individual line profile at granule and intergranular lane. *Right*: Observed blended with double lines in the middle panel. Solid line locates the center of line profile, which is called *bisector*. Bisector shows distorted shape, meaning line profile has an asymmetry.

1.3 5-min oscillations

Separating the oscillatory motion is needed to investigate pure granular convection. On the solar surface, in addition to granular convection, the observed velocity field includes oscillatory signals called as 5-min oscillations. In the spectroscopic data, it is critically important on investigating the dynamics of granular convection itself. Oscillatory signal has a 3-8 minutes period. In the solar photosphere, there are global periodic oscillations known as 5-min oscillations. It is an acoustics wave of the global eigenmode.

The 5-min oscillations was identified by Leighton et al. (1962). He recorded time series of the Doppler velocity on the solar surface, and detected a global periodic variation. The amplitude of 5-min oscillations is approximately 300m/s. It is not negligible for convective velocity (Ulrich 1970). Furthermore, 5-min oscillations not only affect the velocity field on the photosphere, but also cause minor change on intensity of granulations.

Fig. 1.8 is a schematic diagram for 5-min oscillations. These oscillatory motions are believed to be generated by the difference of pressure gradient with granular motion. It propagates through the solar interior. Because there is a steep gradient of density at the photosphere, compressive wave of limited eigenfrequency can propagate through the solar interior with sound speed. In Fig. 1.8, three p-mode waves, each with a different eigenfrequency, are shown by solid, dashed, and dotted lines, respectively. When a wave propagates to the interior, the compressive wave gradually changes the angle of propagating direction and is finally distorted in deep layer. After that, this wave moves to outward with changing its proceeding angle. When p mode arrives at the photosphere, an angle of incidence is vertical to solar surface. As a result, these oscillatory motions cause vertical velocity fluctuation. The dispersion relation of those oscillatory motions at the photosphere are clearly seen on k-ω diagram, which is transformed power for observed velocity at each spatial wave number and each temporal frequency through Fourier analysis. A wide field-of-view and long-term observation of *Michelson Doppler Imager (MDI)* on the *SOHO* spacecraft revealed the strong discernible p-mode as red ridges (Fig. 1.9). In

Fig. 1.9, multiple red ridges are concentrated on 2-5 mHz corresponding to 3-8 minutes, which is 5-min oscillations. Each of red ridges corresponds to individual p-modes drown in Fig. 1.8. Another strong power is discernible in lower frequency, less than 1 mHz. This corresponds to granular motion.

The property of 5-min oscillations varies with height. Deubner (1974) found the fact that the amplitude slightly increases with height. He made the k- ω diagram from several lines that are formed at different heights over the photosphere. 5-min oscillations are considered as a standing wave, because significant propagation of phase velocity at different heights have not been identified (Priest 2014).

To understand the 5-min oscillations' behavior, it requires high time cadence to identify the propagation of oscillatory motions. However, this high time resolution sampling affects badly on bisector analysis. Non-integrated spectroscopic data over time is low S/N which leads to degraded accuracy of velocity field.

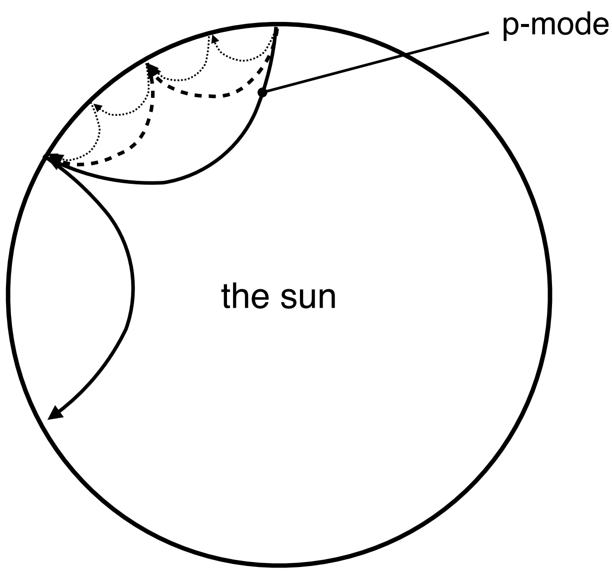

Figure 1.8: Schematic diagram showing oscillator motions in the sun.

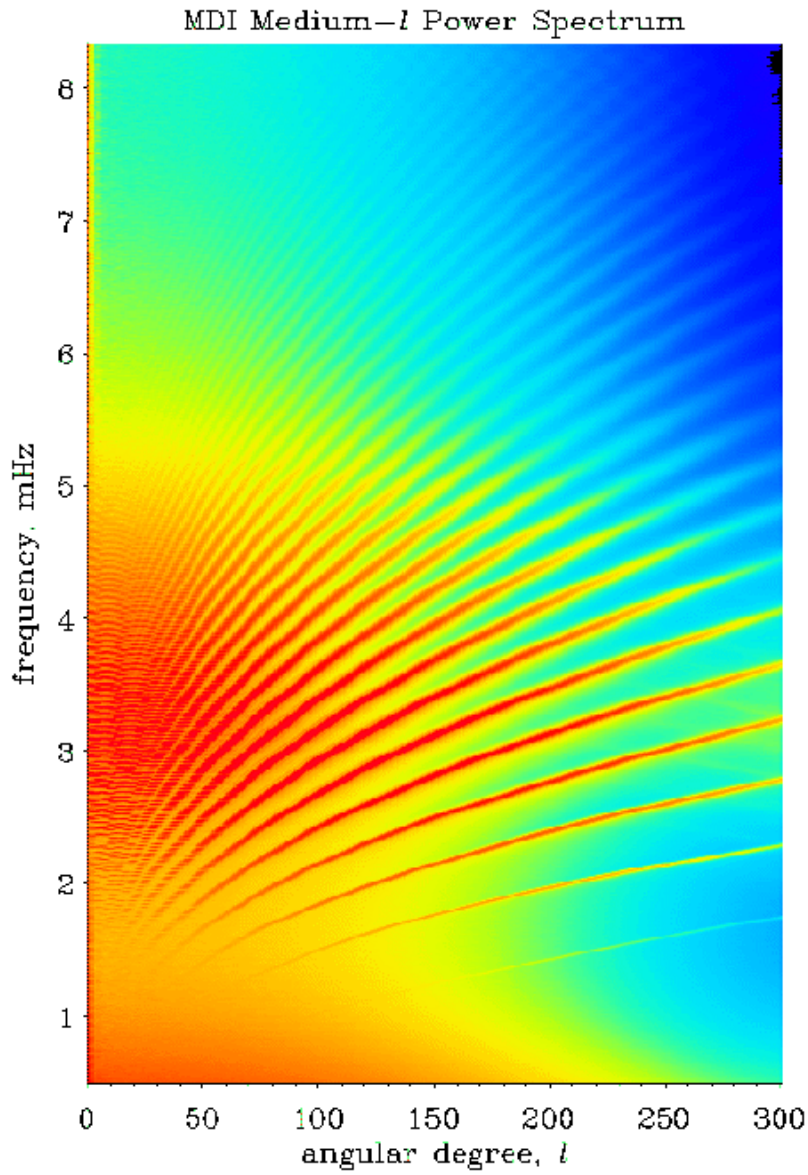

Figure 1.9: Power of 5-min oscillation. Horizontal axis shows spatial frequency. Vertical axis shows means time frequency. Horizontal axis means spatial wave number.

1.4 Purposes of this study

Investigations of the dynamical convection at the solar photosphere require observations and data analysis with addressing three key points; 1) Extracting the behaviors of velocity structures in the direction vertical to the solar surface, 2) spatially resolving granules and intergranular lanes, and 3) removing 5-min oscillations from the velocity data.

In this study, we tackled these key points. We analyzed the spectral line profile observed with Solar Optical Tescope (SOT) onboard *Hinode* by bisector analysis. The spectroscopic data from *Hinode* is ideal for addressing these three key points. Because the *Hinode* satellite observes from space, the SOT spectroscopic data has a diffraction limited 0.3" spatial resolution, which has much advantage compared with seeing-affecting ground-based observations. The width of the intergranular lane is roughly 0.3 ", which can be resolved with SOT observations. Second, high reliable intensity is obtained at each wavelength. The reliability of velocity calculated by bisector analysis, which utilizes the shape of line profile, is strongly affected by signal-to-noise at each wavelength. The SOT's spectroscopic data with $S/N \approx 1000$ makes intensity error negligible impacts. Furthermore, this space observation with low noise allows us to obtain the continuous series of spectroscopic data in a cadence of a few seconds. This high time cadence is impossible for ground-based telescope to perform owing to atmospheric seeing effect.

The goal of this paper is to derive the properties of 5-min oscillations and granular convection at different heights, after discriminating between oscillatory signals and convective one. In particular, the bisector analysis method combined with *Hinode*'s high spatial resolution data are expected to unveil the new properties of convective structure in granular region and intergranular region. Moreover, using derived pure convective structure, we attempt to understand the time evolution of convective structure during granular fragmentation. Fragmentation is the most frequent birth-mechanism of granules, which is 84.4% (Hirzberger et al. 1999).

My master thesis is organized as follows. In section 2, we describe the telescope and its instrument onboard the *Hinode* spacecraft, observations, and the data reduction. In section 3, we show our way to obtain the velocity at different heights and discriminate 5-min oscillations. Section 4 presents the results from the data analysis; the spatial distribution of velocity structures, the velocity structure of the convection in the vertical direction, the properties of the removed 5-min oscillations, and some examples of dynamical evolution of granules showing fragmentation. The derived results are discussed in section 5. In section 6, I summarize our findings and briefly discuss future works.

Chapter 2

Observations and data reduction

The data examined in the thesis was obtained from Solar Optical Telescope (SOT) onboard the *Hinode* spacecraft. In this chapter, the observations and the examined data are described with the data reduction applied to the data.

2.1 Observations

In this section, I described the *Hinode*/SOT and two datasets which are used to analyze the convective strucuture.

2.1.1 *Hinode* Solar Optical Telescope

The *Hinode* satellite (Kosugi et al. 2007) was launched in September 2006. It is equipped with three instruments : the EUV imaging Spectrometer (EIS) and the X-Ray Telescope (XRT), and the Solar Optical Telescope (SOT) (Tsuneta et al. 2008) (Fig. 2.1). The SOT's observing wavelength bands are in the visible light and diagnose gas dynamics and magnetic fields at the photosphere. This study on gas convection uses only the data from SOT.

The diameter of the SOT's primary mirror is 50 cm and its diffraction limit for 630 nm is $\sim 0.3''$, which approximately corresponds to 200 km on the solar surface. The diffracted imaging performance is archived with the development of the optical system (Suematsu et al. 2008) and the real-time stabilization of images on the focal plane detectors (Shimizu et al. 2008). The SOT focal plane package (FPP) has two instruments, i.e., Filtergraph (FG) and Spectro-polarimeter (SP), and they work together for diagnosing physical conditions, such as magnetic field strength and its three dimensional orientation, and Doppler velocity, in the photosphere. The optical schematic of the SOT is shown in Fig. 2.2. In this Figure, Spectro-polarimeter is painted in magenta.

The FG optical path consists of Broadband filter imager (BFI) and Narrowband filter instrument (NFI). BFI has 6 different interference filters, each of which is dedicated to CN 383.3 nm for photospheric network imaging, CH 430.5 nm (G-band) for magnetic elements, Ca II H 396.9 nm for chromospheric heating, 450.5 nm for blue continuum temperature, 555.1 nm for green continuum temperature and 668.4 nm for red continuum temperature, respectively (Table 2.1). From the BFI observations, only blue (450.5 nm) continuum images are used in this study, because blue continuum is the shortest wavelength among three continuum wavelengths. Smaller diffraction limit by using the short wavelength light allows us to obtain the image with sharp contrast.

The SP is designed to obtain the full 4 Stokes profiles (I, Q, U, V) of two magnetic sensitive spectral lines to investigate magnetic field vector at the photosphere. The SP is an off-axis Littrow Echelon spectrograph. Incident light is imaged at the slit plane. The light passing the slit are imaged at the grating by the Littrow mirror and the grating disperses the light in the wavelength direction. Finally it is imaged on the CCD by the Littrow mirror (Lites et al. 2013). The spectral range includes two Fe I lines at 630.15 nm and 630.25 nm, both of which are highly sensitive to magnetic fields. The spectral resolution of the SP is 0.03 nm and the sampling by CCD pixels is 0.0215 nm (Table 2.2). The SP obtains the spectral data at one time for one slit oriented along the solar North-South direction. When we need a 2-D spatial map of the spectral data, the folding mirror on the scanning mechanism moves the solar image on the slit in the East-West direction. The SP records the spectral data at each slit position. This is called *slit scan* observation (Fig. 2.3). It should be noted that the slit scan observations take a long duration (several tens of minutes to a few hours) for covering a wide field of view and the spectral data at each slit position is recorded at a different time.

In this study, we tried understanding the dynamical nature of gas convection at the solar surface. The magneto-convection, i.e., interaction of gas convection with magnetic fields, is much more important for physically understanding various questions, such as heating and dynamics of the upper atmosphere, but the inclusion of magnetic fields in the spectral profiles give more complications for interpreting the spectral profiles. Before investigating spectral profiles seen in magnetic regions (as a part of the Ph.D. dissertation), it is important to understand the dynamical nature of gas convection in the case of non-magnetic field influence.

BFI			
Field of View			218 × 109 arcsec (full FOV)
CCD			4k × 2k pixels (full FOV)
Spatial sampling			0.0541 arcsec/pixel (full resolution)
Spectral coverage			
Center (nm)	Width (nm)	Line of interest	Purpose
388.35	0.7	CN	Magnetic network imaging
396.85	0.3	Ca II H	Chromospheric heating
430.45	0.8	CH	Magnetic elements
450.45	0.4		Blue continuum temperature
555.05	0.4		Green continuum temperature
668.40	0.4		Red continuum temperature

Table 2.1: Characteristics of SOT's Broadband Filter Imager (BFI).

SP	
Field of View along slit	163.8 arcsec (N-S direction)
Spatial scan range	327.62 (transverse to slit, E-W direction)
Spatial sampling (slit)	0.16 arcsec
Spectral lines	Fe I 630.15 nm, Fe I 630.25nm
Spectral coverage	630.08 to 630.32 nm
Spectral resolution/sampling	3pm/2.15pm
Measurement of polarization	Stokes I, Q, U, V simoltaneously

Table 2.2: Characteristics of the spectro-polarimeter (SP).

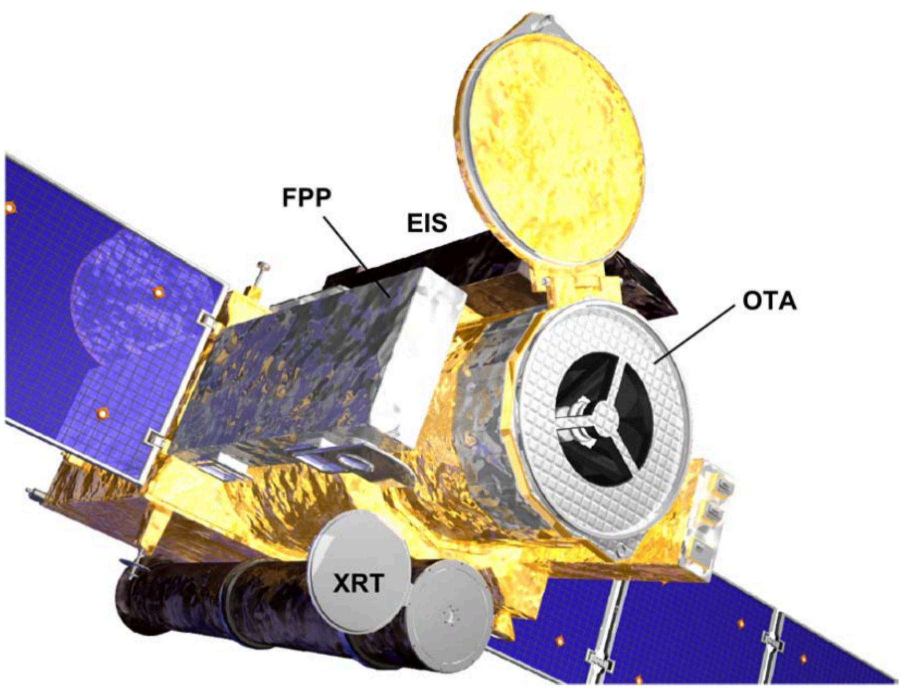

Figure 2.1: *Hinode* outlook from Tsuneta et al. (2008). SOT consists of the telescope and its focal plane package; The telescope (Optical Telescope Assembly, OTA) is a 50cm diffraction limited Gregorian Telescope. Focal plane package (FPP) including SP and FG is attached beside the telescope, which descriptions are written in the text.

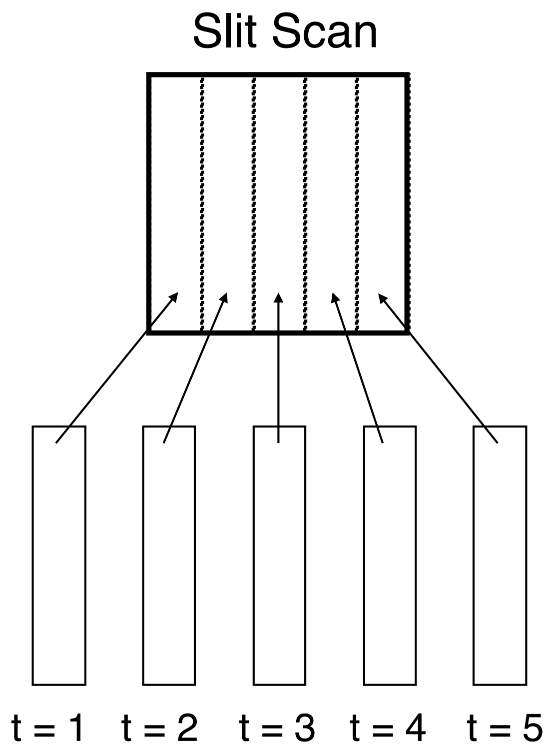

Figure 2.3: Schematic figure of *slit scan* observation. One image consists of several slit images, each of which is measured at a different time.

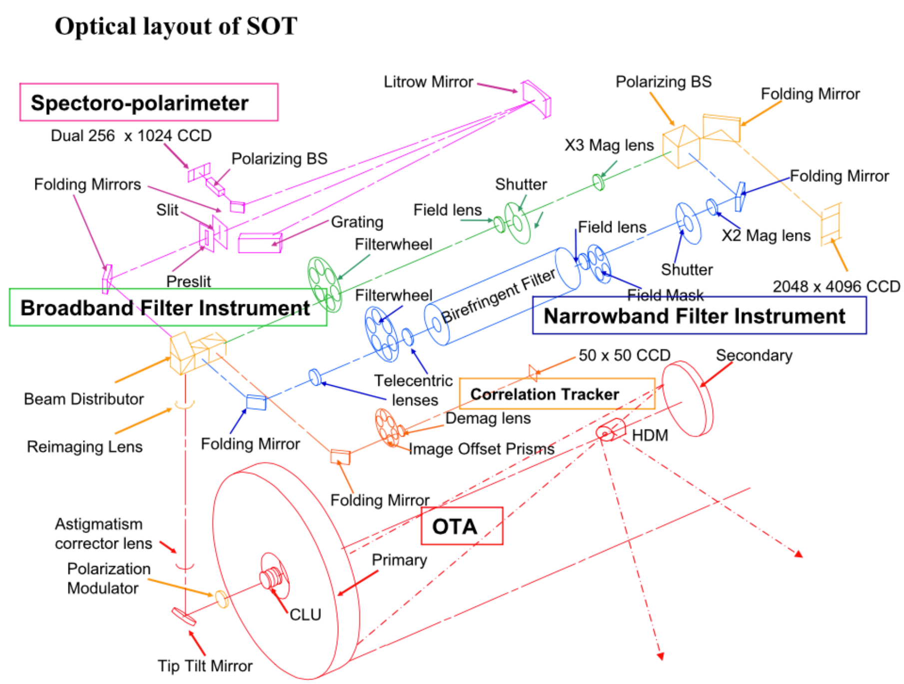

Figure 2.2: Optical layout of SOT. Extracted from Tsuneta et al. (2008)

2.1.2 Datasets examined

In this study, two data-sets were analyzed to investigate the dynamical structures of gas convection in the vertical direction at the photosphere. Dataset 1 is an existing data which is dedicated to investigate the 2 dimensional spatial distribution of the velocity field structures. On the other hand, we newly proposed the observation plan to obtain dataset 2, because there were no data being suited to investigate the successive dynamics of the granulation. This dataset is to unveil the property of the dynamics of the convective structures and 5-min oscillations at high temporal resolution.

Dataset 1 consists of only SP data with *slit scan* (Fig. 2.4). Specific information on this data-sets is listed in Table 2.3. In this observation, the Stokes profiles at two slits position with integration time of 1.6 second and two pixels along slit are summed. As a result of this integration and summing, spatial pixel size is 0.30" for East-West direction, and 0.32" for North-South. It takes 44 minutes to map the whole region. The region is located almost at the center of the solar disk; The slit position at the middle time of the scanning is (2".9, 7".8) at the solar heliocentric coordinate.

Dataset 2 is compose of both SP and FG data. The SP data is a high cadence time series of the spectral data, which is recorded at the same slit position all the time during the observation. The measurements at the fixed position without slit movement are called *sit and stare*. The SP slit scans obtained the spectroscopic data every about 2 second, allowing us to observe fast transformation of the convective structures, whereas the FG observation recorded every 30 seconds is designated to know the exact slit position on the evolving granules moved by the horizontal motion. A total of 1434 SP frames were recorded, while FG were 90. One of the FG blue continuum image from dataset 2 is shown in Fig. 2.5 and one of the SP spectral data in Fig. 2.6. A time sequence of SP continuum intensity at 630.1 nm averaged over 0.01 nm is shown in Fig.2.7. The intensity normalized by the continuum intensity averaged in the full pixels.

A high S/N (signal-to-noise) is achieved with the large number of input photons at each wavelength. For instance, Fig.2.6 shows one spectral data from dataset 2. The vertical axis is in unit of Data Number (DN). 1 DN corresponds to 100 incident photons. Thus, the number of photons in continuum wavelength (around 630.10 nm) is approximately $750,000$ photo counts. The photon noise assumed to be under the Poisson distribution, their standard deviation is $\sqrt{750,000} \simeq 866$ photon counts. This value is roughly 9 DN. Accordingly, The S/N is $7500/9 \simeq 833$. In the line core of Fe I 630.15 nm, DN is approximately 2,500, and its S/N is larger than 500.

The observed target of both datasets is the quiet region where the degree of polarization is less than 1% in the entire field of view, according to V/I_c, where I_c is continuum intensity of Stokes I, and V is the highest Stokes V signal at each spectral profile.

	SP
FOV (field of view)	219 ″(EW), 121 ″(NS)
FOV (pix unit)	685 × 384 pixels
Position	2 ″.93, 7 ″.81
Pixel size (x,y)	0 ″.30, 0 ″.32
Time per position	1.6 sec
Start Time	2009/2/14/15:00 UT
End time	2009/2/14/15:44 UT

Table 2.3: Description of Data-set 1. Y-direction(NS) of pixel size means the direction along the SP slit, and X-direction(EW) of pixel size represents the direction to slit scan.

	SP	FG
FOV (field of view)	0 ″.16 (EW) × 81 ″.6(NS)	19 ″.2(EW) × 88 ″.9(NS)
Pixel size (x,y)	0 ″.16, 0 ″.16	0 ″.11, 0 ″.11
Time cadence	1.6 second	30 second
Exposure time		60m second
The number of frames	1434	90
Start Time	2014/07/06/22:56	
End time	2014/07/06/23:41	

Table 2.4: Description of Data-set 2.

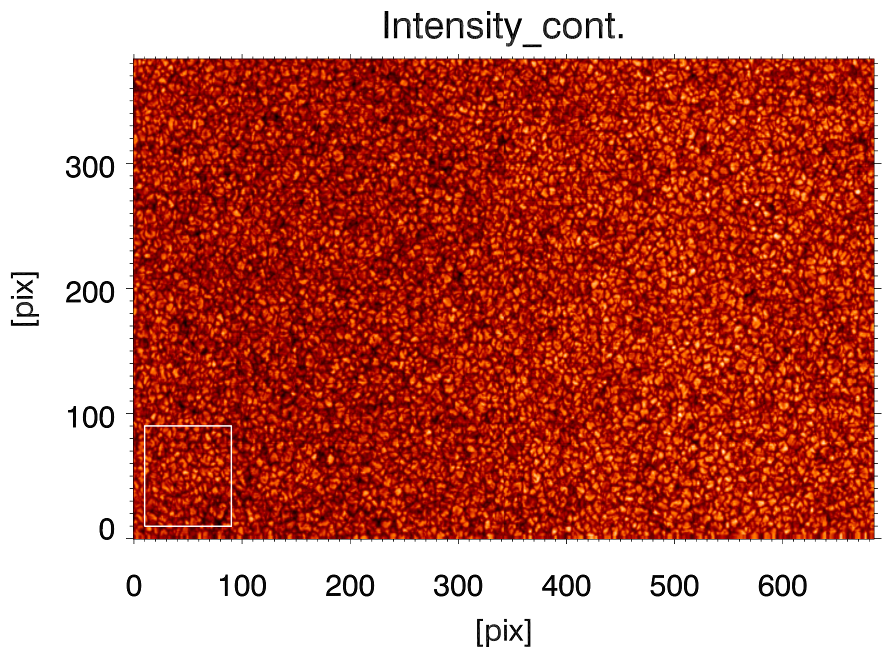

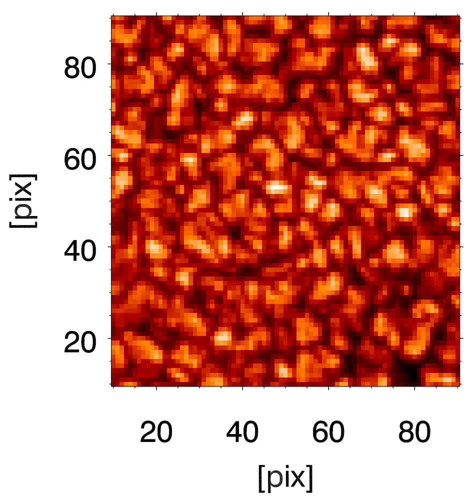

Figure 2.4: An continuum intensity of dataset 1. *Upper panel*: Whole view of the observation. *Lower panel*: Enlarged image for the region surrounded by white square on the upper panel.

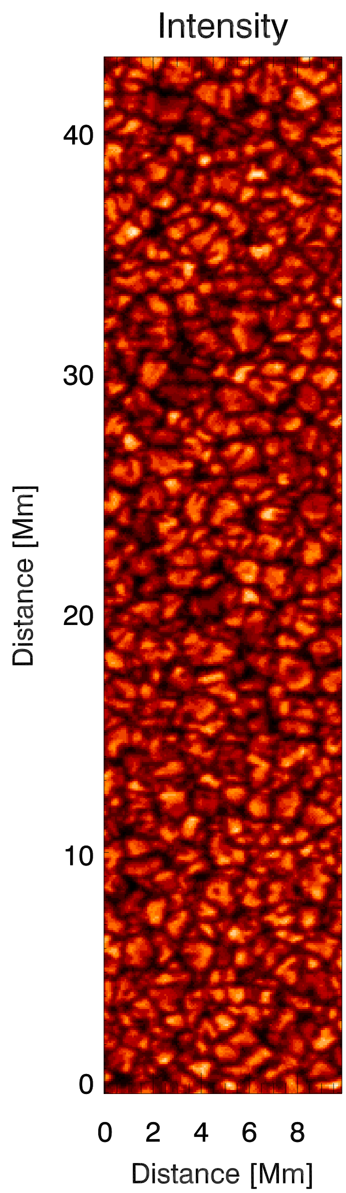

Figure 2.5: One of the FG blue continuum images from dataset 2. 0.”16 corresponds to roughly 0.11 Mm.

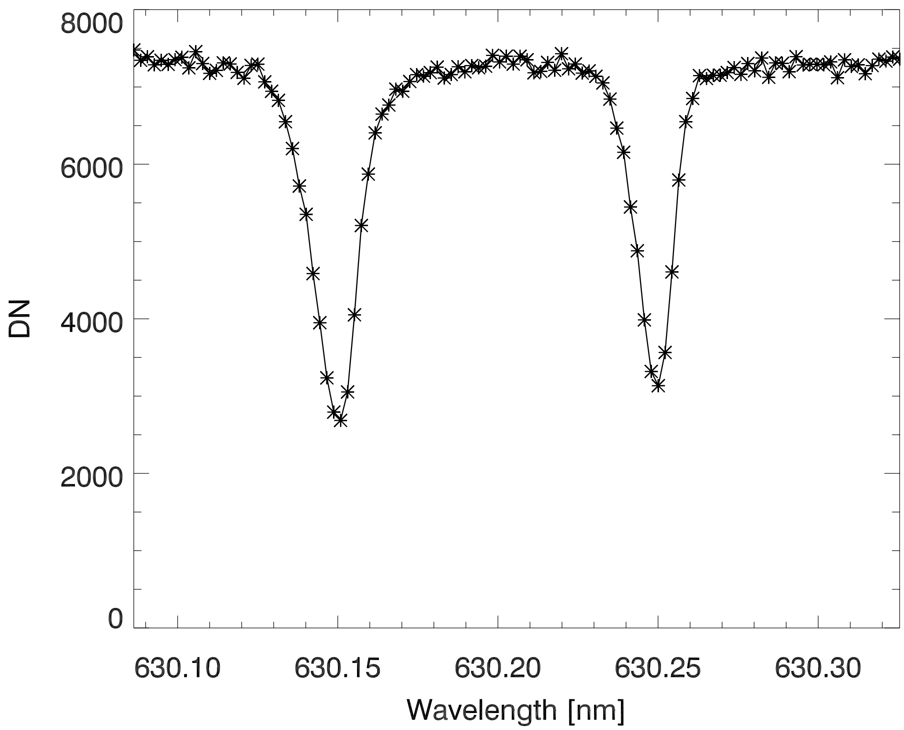

Figure 2.6: Spectral data.

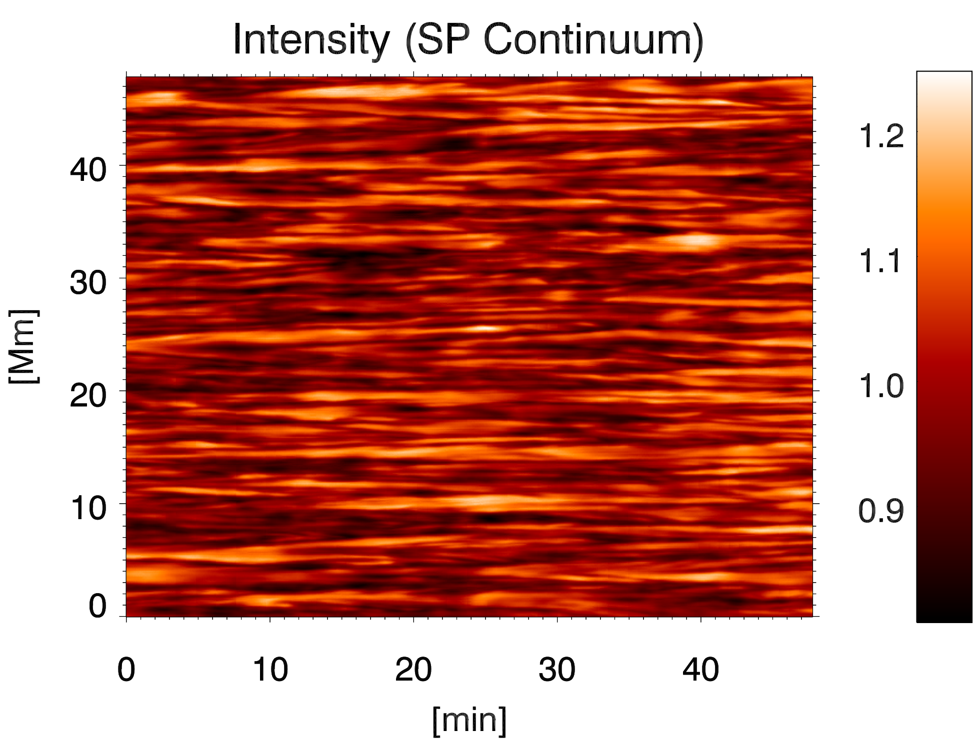

Figure 2.7: Time-distance map of continuum intensity which is at 630.1 nm averaged over 0.01 nm. The vertical axis is the slit direction.

2.2 Data calibration

The SP data was calibrated by using the standard calibration routine SP_PREP, which is available in SSW (Solar SoftWare) (Lites & Ichimoto 2013). The SP_PREP routine performs the calibration including i) dark-field correction, ii) flat-field correction, iii) compensation for residual $I \rightarrow Q$, U, and V crosstalk, iv) the removal of periodic wavelength shifts in the period of the spacecraft orbit (about 98 minutes), caused by the thermal deformation of the instrument optics and orbital Doppler shift. v) The calibration of intensity variation along the SP slit caused by tiny variation of the slit width. This correction is based on pre-launched sunlight calibration data. FG_PREP was also used to calibrate FG data. It also performs some processing including, dark-field correction and flat-field correction.

Regarding the absolute wavelength calibration, we utilized the wavelength calibrated by the SP_PREP routine but we had a rough estimation of wavelength errors by using the mean line profile synthesized from observations. The wavelength of the spatially averaged line profile is slightly blue shifted on the photosphere, which is called *convective blue shift*. Line profiles in granular region contribute more to the mean line profile, causing convective blue shift, because it covers a slightly larger fraction of the total area on the photosphere. Each absorption line reflects at different heights respectively, convective blue shift varies for each line. Dravins et al. (1981) investigated convective blue shift with 311 absorption lines. According to their reports, convective blue shift of Fe I 630.15 nm is roughly 200 m/s, which has an error of 100 m/s. In our analysis, the velocity of the mean line profile shows 140 m/s. The difference from Dravins et al. (1981) is 60 m/s and thus the error would be 160 m/s at the worst in our results.

2.3 SP - FG data co-alignment

In dataset 2, the SP spectral data was recorded for the fixed slit position and it is impossible to know from where the spectral data comes in dynamically evolving granule patterns. The FG blue continuum images, which are normalized spatially in the field of view, are used to identify where the SP slit (width is 0.16 arcsec) is placed in the granulation pattern. Co-aligning the SP slit position on the FG images with high accuracy is achieved by searching where the intensity difference between the SP continuum and FG continuum is minimized.

At first, the pixel scale of the FG data was rescaled to match to that of the SP data. After this, to identify the position of SP slit, we put the intensity of SP slit to FG intensity map and calculated the Root Mean Square (RMS) on its difference (Fig. 2.8) for each of the pixel shift to all the pixel positions. Fig. 2.8 shows three examples of the RMS calculation. In the top of the figure, to derive the RMS of the difference between SP and FG for the 4 pixels superposed on each other, the calculated RMS was given to the center pixel of the slit in the RMS data array (see right panel). This procedure was implemented one by one. After deriving this RMS map (Fig. 2.9), we extracted the position where the minimum value is observed, giving the best co-alignment position. This processing was applied to all the SP slit data compared with the FG continuum image that was taken at the closest time with each SP data. As a result, SP intensity slit located on the FG map of intensity at each time is shown in Fig. 2.10. It is apparent from this figure that the FG Intensity patterns is well matched with the SP slit image. Fig.2.11 is a scatter plot of the SP slit continuum intensity and the co-aligned FG intensity, showing a good correlation between them.

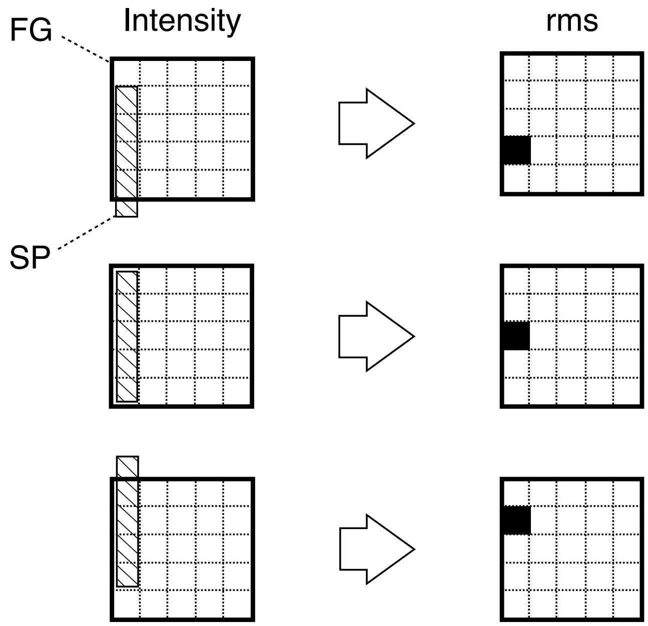

Figure 2.8: Alignment between SP and FG. *Left column*: An FG blue continuum image with three examples of pixel shift for the compared SP slit continuum data. *Right column*: The RMS of the intensity difference is calculated and is given to the center pixel of the slit in the RMS data array.

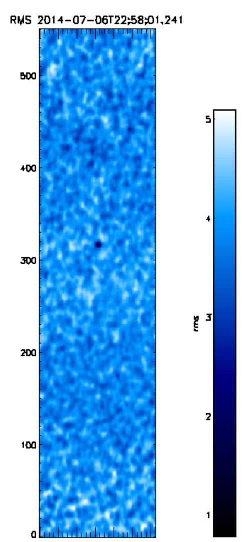

Figure 2.9: RMS map of the difference between SP continuum and FG continuum. Note that in the center there is a dark dot where the lowest difference, meaning the best-coaligned position.

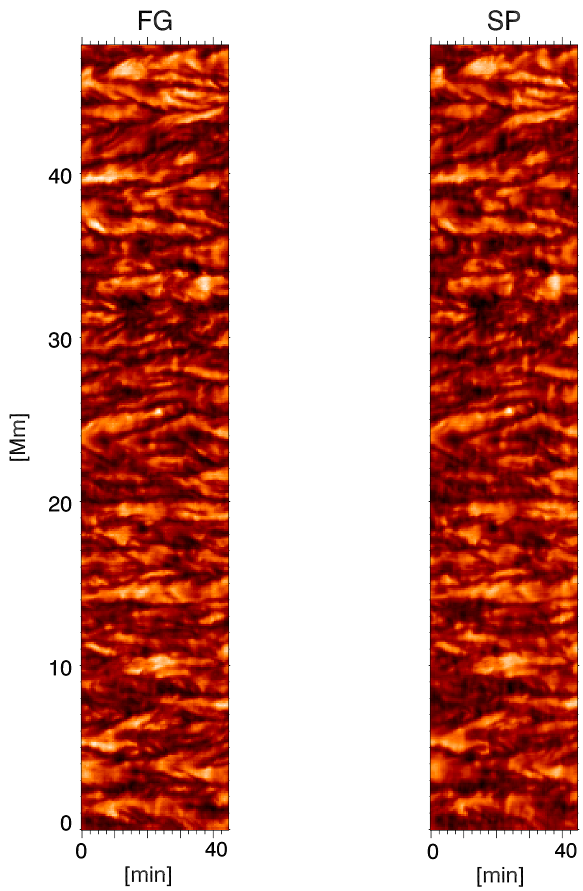

Figure 2.10: The time evolution of the FG blue continuum intensity at the SP slit position of the co-aligned FG data (left), compared to that of the SP continuum intensity (right).

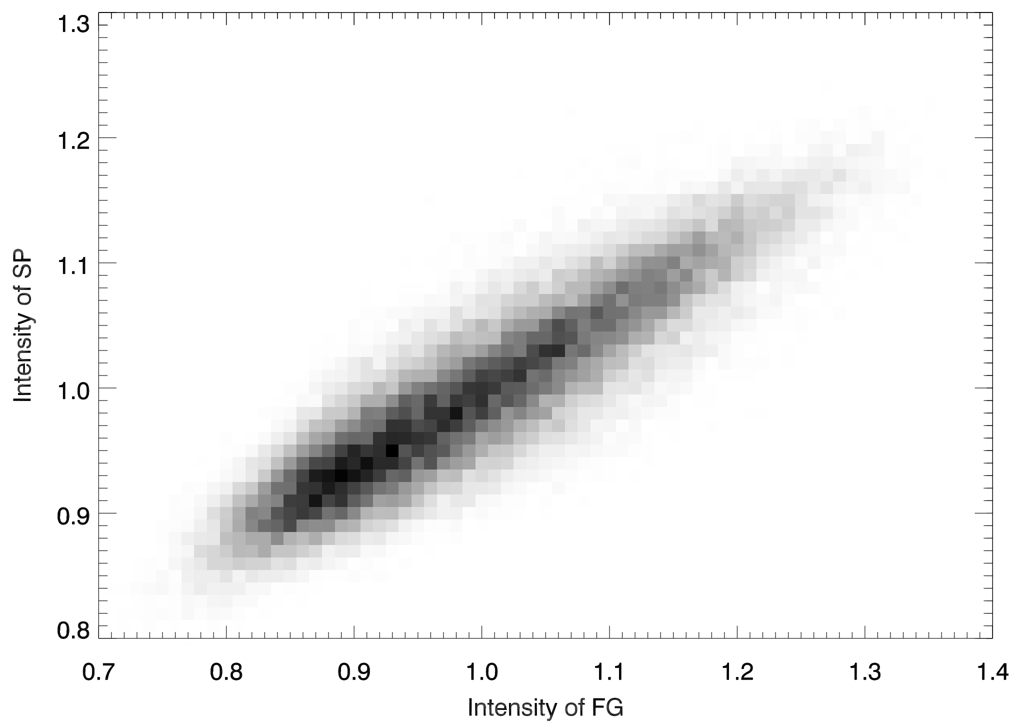

Figure 2.11: Scatter plot between FG intensity and SP continuum intensity.

Chapter 3

Analysis methods

This chapter describes two key analysis methods for deriving the line-of-sight velocity structures as a function of height: 1) Bisector analysis for describing the asymmetry shape of the observed Fe I 630.15 nm line, and 2) Removing the 5-minutes oscillations component from the time series of the velocity data.

3.1 Absorption line property

In this section, we introduce the concept for deriving the *Doppler velocity* at different heights in the photosphere.
In astrophysics, the general method for deriving velocity field is to utilize the wavelength shift of a spectral line (absorption line in this study) in spectroscopic data. The wavelength shift from the original wavelength of the spectral line is called *Doppler shift*. This basic physical phenomenon is as follows: When a radiating object moves along the direction toward an observer, the wavelength position of the spectral line is shifted by the speed of the object. The speed of the moving gas parcel v is given by

$$v = c\frac{\Delta\lambda}{\lambda_0}, \tag{3.1}$$

where c is the speed of light, λ_0 is the wavelength of the absorption line without the motion, and $\Delta\lambda$ is doppler shift. In this study, 3.0×10^5 km/s and 630.15 nm are used in c and λ_0, respectively.

Next, we will discuss how to obtain the information as a function of the height, by using the radiative transfer. Let us treat the radiative transfer equation, which consists of emission term and absorption term (Rybicki & Lightman 1979, Gray 2008, Stix 2004). Here, we assume the absorption coefficient κ is defined by

$$dI_\lambda = -\kappa_\lambda \rho I_\lambda ds, \tag{3.2}$$

where ρ is the density of the medium the light passes, λ is the wavelength, I is the intensity of the incident light and ds is the distance light travels. On the other hand, emission coefficient j is defined by

$$dI_\lambda = j_\lambda \rho ds. \tag{3.3}$$

Thus, radiative transfer equation, which consists of emission and absorption terms, is written as,

$$dI_\lambda = -\kappa_\lambda \rho I_\lambda ds + j_\lambda \rho ds. \tag{3.4}$$

Let us introduce *an optical depth*, which is defined by

$$d\tau_\lambda = \kappa_\lambda \rho ds, \tag{3.5}$$

or its integral,

$$\tau_\lambda(s) = \int_{s_0}^{s} \kappa_\lambda \rho ds. \tag{3.6}$$

If we substitute (3.5) for (3.4), the radiative transfer is

$$\frac{dI_\lambda}{d\tau_\lambda} = -I_\lambda + S_\lambda. \tag{3.7}$$

Here, S is a *source function*, i.e. the ratio between the emission coefficient and the absorption coefficient:

$$S_\lambda = \frac{j_\lambda}{\kappa_\lambda}. \tag{3.8}$$

The formal solution of (3.7) is

$$I_\lambda(\tau_\lambda) = I_\lambda(\tau_{0\lambda})\exp\big[-(\tau_{0\lambda} - \tau_\lambda)\big] + \int_{\tau_\lambda}^{\tau_{0\lambda}} S(\tau'_\lambda)\exp\big[-(\tau'_\lambda - \tau_\lambda)\big]\tau'_\lambda, \tag{3.9}$$

where $\tau_{0\lambda}$ is an optical depth at some level of reference. When we integrate from $\tau_\lambda = 0$, where we observer, to $\tau_{0\lambda}$, i.e. deep into the sun, we obtain the total emergent intensity,

$$I_\lambda(0) = \int_0^\infty S_\lambda(\tau_\lambda)\exp(-\tau_\lambda)d\tau_\lambda. \tag{3.10}$$

The linear change of source function as a function of optical depth well match in the solar photosphere,

$$S_\lambda(\tau) = a\tau_\lambda + b. \tag{3.11}$$

If we substitute (3.11) for (3.10), it is clear that most emergent intensity reflects on $\tau = 1$.

κ_λ is total coefficient absorption. We must distinguish between line absorption and continuum absorption.

$$\kappa_\lambda = \kappa_c + \kappa_l. \tag{3.12}$$

where κ_l is the line absorption coefficient and it depends on bound-bound transition. Its transition is caused by incident photon, which enhances the level of electrons to higher level. An excited level has a fixed energy because of quantization, and thus the bound-bound transition gives a certain wavelength λ_0. In the photosphere, particles have a thermal velocity, leading to spreading κ at λ_0 by Doppler shifts. Thus, an enhanced absorption coefficient is broadening according to Maxwellian distribution (Fig. 3.1). We can conclude the fact: A) An absorption coefficient has a peak at the line core and it decreases toward the wings of the line profile.

Next, we treat the absorption coefficient being related to where the emission reflects on. When κ_λ has a high value, the layer of $\tau_\lambda = 1$ becomes shallower according to (3.6). As a result, emission we observe reflects on higher layer in the photosphere. This is abstractly explained in Fig. 3.2. In the left panel of this figure, the light coming from upper side penetrates the medium with little decrease because of low absorption coefficient, accordingly most parts of light originates from backside. On the other hand, in the right panel, the light with higher absorption coefficient loses its intensity originating from backside, hence the observed light is dominantly generated at shallower medium, because the medium not only absorbs the light but also newly radiates (see the second term in the right-hand side of (3.4)). We can establish the fact: B) the observed light with higher absorption coefficient is formed at the shallower part, while it with lower absorption coefficient is originates from deeper.

Combining A) and B) means that the line core is formed at the higher portion of the line formation range, while the wings are formed at the lower layer. In this study, we focus on the fact that higher intensity close to the continuum level in the line profile reflects on lower layer, whereas lower intensity near to the line core represents higher layer in the photosphere.

According to the calculation by a solar atmospheric model (Vernazza et al. 1981), averaged one dimensional model, the line core intensity of Fe I 630.15 nm shows approximately 300 km above the $\tau = 1$ height of the continuum at 500 nm (Fig. 3.3). *The contribution function* represents the integrand of (3.10), $S_\lambda(\tau_\lambda)\exp(-\tau_\lambda)$, meaning the observed emission consisting of mainly around peak of 310 km. Note that, this calculation based on a mean atmospheric model, including granules and intergranular lanes. The local temperature structure influences on each line formation height.

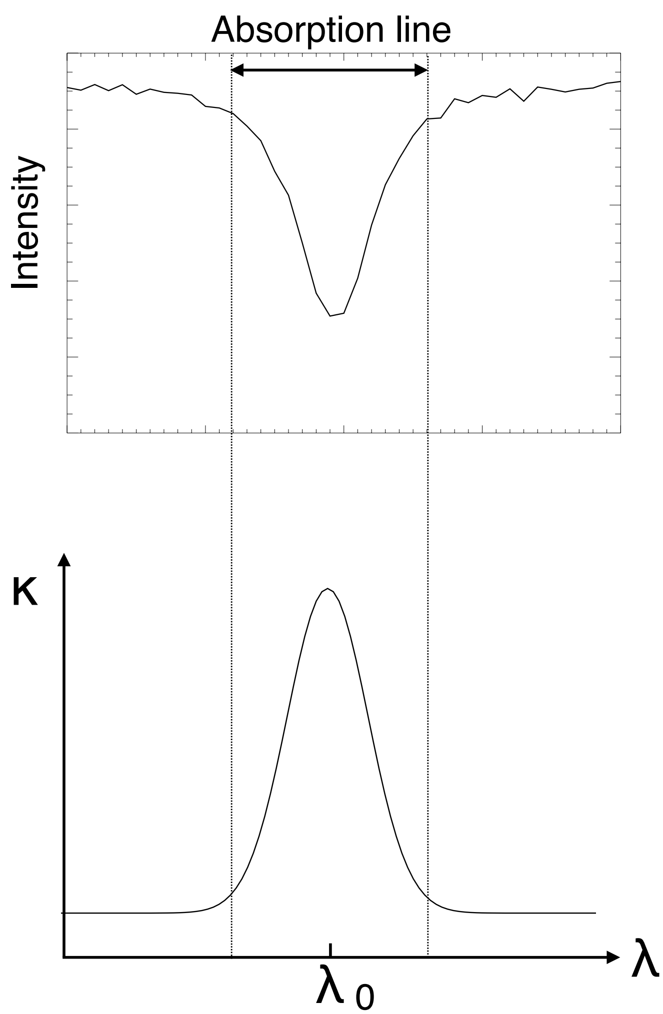

Figure 3.1: Schematic diagram of *absorption coefficient*. *Top*: The observed absorption line. *Bottom*: Absorption coefficient profile. The transition energy corresponds to λ_0. Absorption coefficient profile has Maxwellian distribution, because absorption medium has thermal velocity.

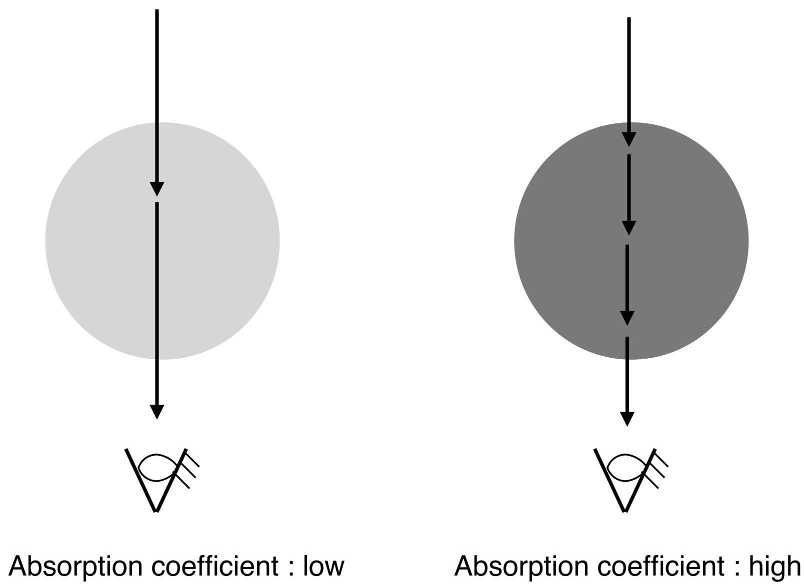

Figure 3.2: Schematic diagram of where coming light originate from. *Left panel*: In the case that light has low absorption coefficient. *Right panel*: In the case that light has high absorption coefficient.

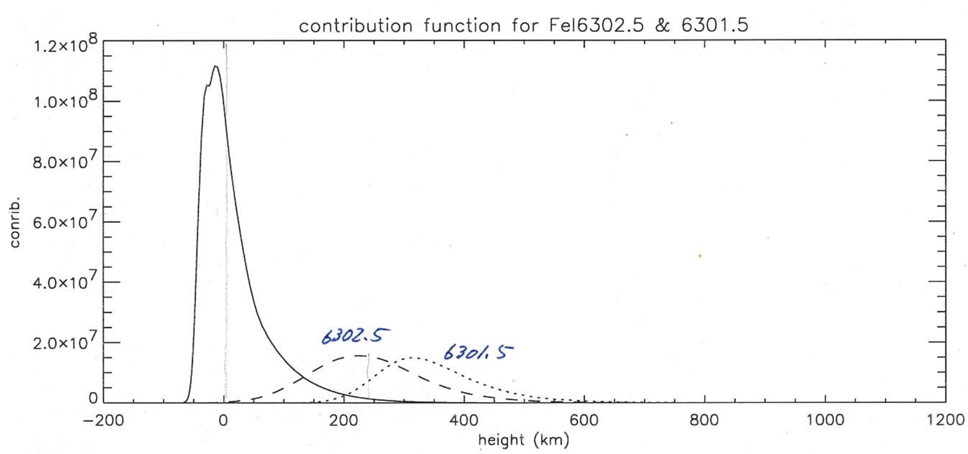

Figure 3.3: Contribution function of Fe I 630.15nm and 630.25 nm. This figure was made by Prof. K. Ichimoto in 1995.

3.2 Bisector analysis

The spectral profiles of the observed absorption lines are actually not symmetric in the wavelength, as shown in Fig. 3.4. The asymmetry observed in the line profile is characterized by *bisector*, which is the line dividing the profile into two equal parts and thus gives the center wavelength at each intensity level. Fig. 3.4 (b) and (d) show the bisector lines for each spectral profile. Since the lower atmospheric layer is observed at the line wings than at the line core, the bisector line tells how large line-of-sight velocity exists at each height in the line forming layer. In this study, to obtain velocity at different heights, we calculated the Doppler shift through (3.1) at each intensity. As mentioned previously, each intensity is normalized by the continuum intensity averaged in all the pixels. The intensity levels every the intensity step of 0.05 are used to obtain the bisector line of line profile, as illustrated in Fig. 3.5. The linear interpolation was used to estimate the profile positions (white circles) at an intensity level and the white circles gives the bisector point (white square). The wavelength shift $\Delta\lambda$ is a deviation of the white square from the original line center position. We can determine the wavelength shift at each intensity. As a result, a wavelength distance, between *white square* in this Fig. 3.5 and original line center position, are regarded as $\Delta\lambda$ being substituted into (3.1) to order to derive the Doppler velocity.

The bisectors derived at the intensity close to the continuum as well as close to the line core are not used in the further analysis because of inaccurate determination of the bisector positions. Considering the fact that a certain intensity reflects the same temperature, we introduce a criterion to determine the intensity range for calculating velocity: we chose 0.10-0.15 of I/I_0 below the continuum intensity as the highest intensity level near the continuum, and the intensity by 0.05-0.10 I/I_0 higher from the line core intensity as the lowest intensity level, where I/I_0 is the normalized intensity level. The line depth tends to be larger in granular region and smaller in intergranular region. Line profile originating from granular region has typically higher continuum intensity ($I/I_0 > 1$) and the line core is deeper (lower intensity). This example of granule is shown in Fig. 3.4 (a) and (b). The maximum intensity is approximately 1.13 and the minimum intensity is roughly 0.26 in this case. The bisector is derived in the intensity range between 0.30 and 1.00, and the bisector is calculated at the 15 levels of intensity. On the other hand, the line profiles formed at intergranular lanes typically has lower continuum intensity and higher intensity in line core, meaning that the number of intensity levels for bisector is smaller than at the granular region. This example is illustrated in Fig. 3.4 (c) and (d); maximum intensity is approximately 0.92 and minimum is roughly 0.32. The obtained intensity range between 0.35 to 0.80, the number of total calculable point is 10. The bisector is derived in the intensity range between 0.40 and 0.75 in most of the data.

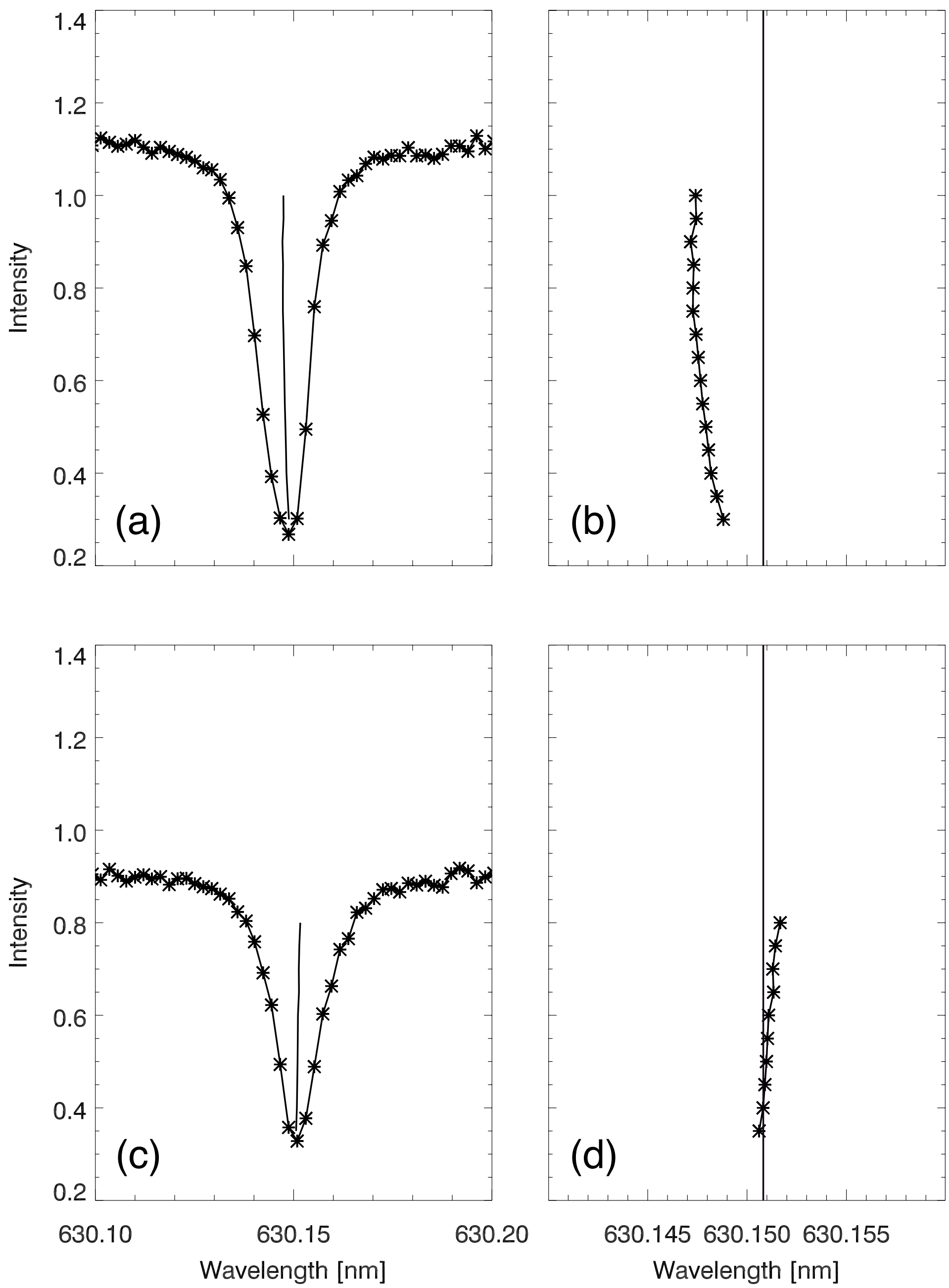

Figure 3.4: (a). Example of an absorption line (Fe I 630.15 nm) in a granule. The solid line drawn in the center of the absorption line is a *bisector*. (b). An enlarged view of (a). The vertical solid line is a center of the line without the influence of Doppler shift caused by the moving parcel. (c). Example of an absorption line (Fe I 630.15 nm) in an intergranular lane (d). An enlarged view of (c).

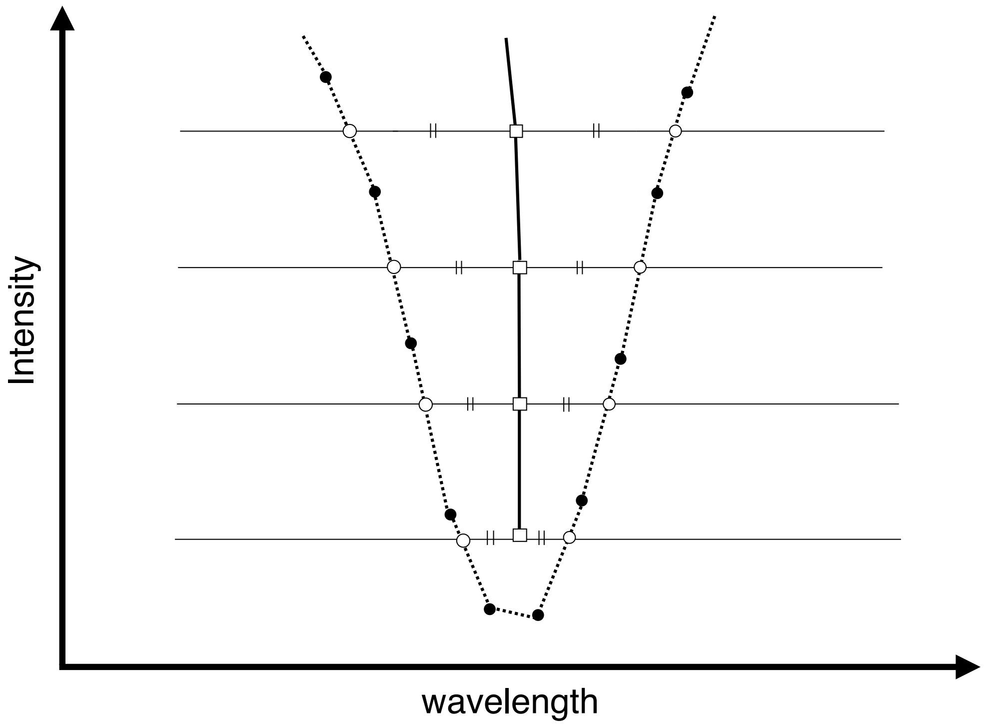

Figure 3.5: A schematic diagram describing how to obtain the bisector. Linear interpolation among observed points for each intensity. *Dark circle*: Observed points. *Dotted line*: Absorption line profile. *Horizontal solid line*: Given intensity. The interval between these two lines is intensity difference of 0.05. *White circle*: Interpolated point among observed points at given intensity. *White square*: The center of line profile at given intensity. *Distorted solid line*: Bisector connecting white squares.

3.3 Separating 5 min oscillations from spectral data

Since the typical amplitude of 5 min oscillations is roughly 300 m/s (Ulrich 1970), the 5-min oscillations component should be separated from the spectral data to determine the behaviors of convective motions. It is apparent in Fig.3.6 that a periodic oscillatory behavior exists in the time evolution of line-of-sight velocity observed at a certain point and that the period of the oscillatory variation is about 5 minutes.

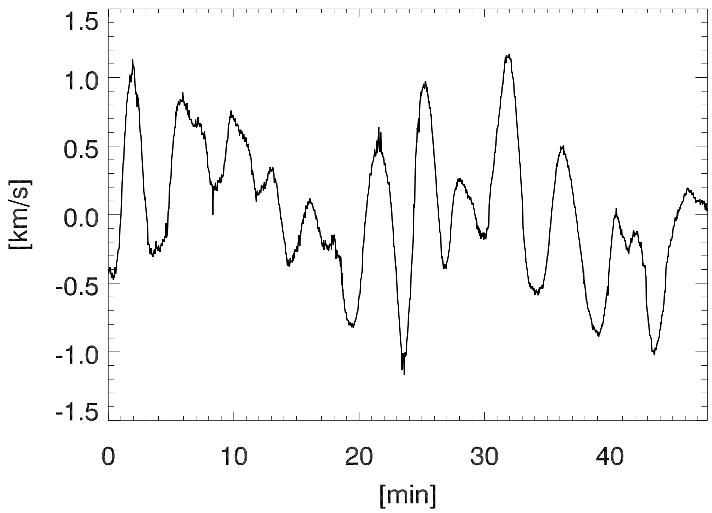

Figure 3.6: The time evolution of line-of-sight velocity observed at a certain point. This time profile gives the temporal evolution of velocities at a certain intensity level (or height) determined by the method described in section 3.1.

Their oscillatory amplitude seems to show a few hundred m/s, which is similar to what has been reported. As a matter of course, without removing this oscillatory component, we cannot determine quantitative behaviors of convections at the solar surface.

A general method to remove the 5 min oscillation component is applying Fourier analysis. The k-ω diagram derived with the Fourier analysis is generally used for the time series of two-dimensional spatial images, however the data examined in this study is the spectral data measured with a single slit. We apply the following Fourier method only to the dataset 2, which is the time series of the spectral data with the slit staying at the fixed position on the solar disk center. The time series of velocity $v(y,t)$ is expressed by the following formula (3.13) using Fourier expansion f:

$$v(y,t) = \int f(k_y, \omega)\exp[i(k_y y + \omega t)]dk_y d\omega, \tag{3.13}$$

where y is a position along the slit, k_y is a spatial wave number along the slit, ω is a frequency and t is time. The power spectrum

$$P(k_y, \omega) = ff^*, \tag{3.14}$$

where asterisk $*$ shows a complex conjugate.

To distinguish between the pure convective velocity and 5-min oscillations, after creating the k-ω diagram, we apply *a subsonic filter* (Title et al. 1989) to separate the 5-min oscillation component from the convection component. In this study, the subsonic filter is applied to dataset 2. This separating process is composed of three steps.

The first step is to transform the two-dimensional (spatial and time) velocity map to k-ω diagram thorough the Fourier transformation. Fig. 3.7 is the k-ω diagram transformed through Fourier analysis at height of intensity ($I/I_0 = 0.40$). Two strong power regions (seen as red) can be seen in the diagram. Note that Fig. 3.7 does not show clear discrete p mode ridges, different from Fig. 1.9 in Chapter 1. This is because the duration of the dataset 2 is only 45 minutes and the area covered by the slit is only 81 arcsec, while it needs long duration and large area observation to draw a discrete p mode ridge in region of low spatial and frequency. The strong power around 2-5 mHz and 0.0 - 0.3 Mm^{-1} can be considered as the 5-min oscillation component, because its location on both time and spatial frequency has good agreement with more reliable results such as Fig. 1.9, derived with the large-field-of-view and long duration data.

The second step is to apply the subsonic filter to the k-ω diagram. In the k-ω diagram, the signals at the phase velocity k/ω $>$ 7 km/s, which is a sound speed on the photosphere and considered as the 5 min oscillations component, because p-mode acoustic waves propagates with the speed of sound. This means that p-mode emerges in the area above the boundary we set. This boundary is depicted in Fig. 3.7 as a dashed line in an inclined direction. The boundary should not be applied at the lower frequency area in the k-ω diagram, because strong signals (in red) below 2 mHz exist in the spatial frequency below 0.2 Mm^{-1} and they had better to be considered as a part of the granular convection.

To avoid the undesirable separation, all components under the 2 mHz, which are regarded as the lowest frequency of 5-min oscillations, are incorporated in pure granular motions (dashed line in the horizontal direction on Fig. 3.7).

The last step is to separate two components, i.e., 5-min oscillations and pure granular convection on the k-ω diagram, and to re-convert each diagram to the velocity data through the Fourier inverse transformation.

The subsonic filter described above is applied to the velocity time-distance maps, each of which is obtained for each intensity level in the spectral profile. The convection time-space map and the 5-min oscillation time-space map are obtained at different heights. Their results will be discussed in section 4.2.

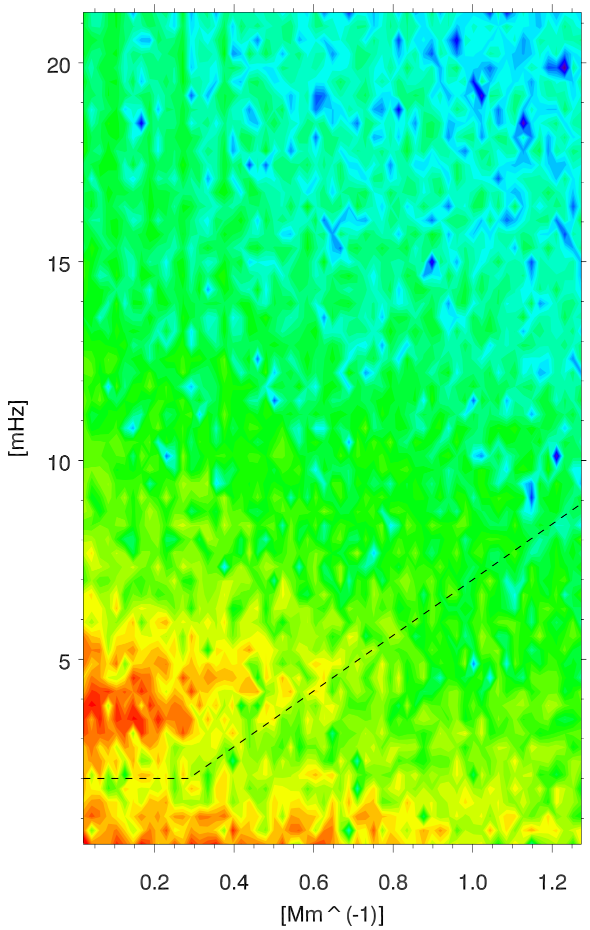

Figure 3.7: k-ω diagram at height of intensity $I/I_0 = 0.40$. Black dashed line is a boundary to discriminate between pure granular convective motion in lower part and 5-min oscillation in higher part.

Chapter 4

Results

This chapter describes results from the analysis. In section 4.1, the velocity field from the scanning data, data set 1, is obtained with bisector analysis. The aim there is to obtain the spatial distribution of the velocity field and to see the basic character of the bisector analysis. In section 4.2, the high-cadence data at the fixed position is analyzed and the main purpose is to distinct the pure convective motion and 5-minutes oscillation by use of the k-ω diagram of the velocity field. In section 4.3, I analyzed the temporal evolution of vertical velocity structures during the granular dynamics, e.g. their disappearance and appearance.

4.1 Spatial distribution of the Doppler velocity field

We investigate spatial distribution of the Doppler velocity field on the solar surface by using dataset 1 and bisector analysis. Fig. 4.1 shows the result of this analysis. The panel (a) shows the distribution of continuum intensity I_0 which is spatial normalized over wavelength from at 630.1 nm averaged over 0.01 nm. The panel (b) shows the distribution of the Doppler velocity derived from the Gaussian fitting, which is commonly used in the various papers. The panels (c) - (f) shows the distribution of the Doppler velocity from the bisector analysis. The line core shows the shallower part in the atmosphere and the wings do the deeper, which are explained in section 3.1. Hence, the panel (c) shows the Doppler velocity field in the deepest layer, and the panel (f) does the shallowest one. We limit the analysis in the range from $I/I_0 = 0.40 - 0.75$. It is because other intensity levels do not have adequately the amount of obtained pixels, less than 90% of the total spatial area. All the panels have the same field of view, 27 " x 29 " or equivalently 80 Mm x 80 Mm. Their color scales are also same range of velocity value from -2 km/s to 2 km/s. We can see four characters from the comparison of the panels (c)-(f). First, the contrast of the velocity field is larger at the lower layers. For example, the contrast in the panel (c) is more clear than that in the panel (f). This means the existence of strong flows of both upward and downward directions in the lower layer. On the other hand, at the higher layers, the contrast is small, meaning weaker flows at the both directions. Third, the size of velocity pattern becomes larger in the deeper layer. Considering that the velocity pattern corresponds to the granular pattern, which will be confirmed in section 5.2, it implies that the size of granule is larger in the lower layer. There are several small velocity granules at the lower layer and larger ones appears at the higher layer ($I/I_0 = 0.40$). Larger size velocity patterns are observed at the higher layers ($I/I_0 = 0.50, 0.40$). At higher layers, it seems that large cellular upflow patterns incorporate the granules with smaller size seen at the lower layers. Fourth, we can see that the strong up regions in the higher layer corresponds to the center of the larger granule cells in the higher layer. In particular, the strong upflow regions seen at the lower layer still remain at the higher layer; One of examples is seen at 70, 50 Mm in Fig. 4.1). The pattern of velocity field with Gaussian fitting is similar to that of one at the higher layer (Fig. 4.1 (f)).

Fig. 4.2 is the number distributions of Doppler velocity of different intensity levels. We can see two tendencies. First, the distribution is wider at the lower layer and the fraction at the peak of the distribution is lower. Second, the peak of the distribution varies from 0.3 km/s to zero with height. These characters are consistent with the idea of that, there are strong velocity fields at the lowerlayer rather than higher layer, it will be discussed in section 5.2. The distribution by gaussian fitting has the most shallow shape, and the peak of this locates in nearly the same value as that of intensity of 0.4.

Fig. 4.3 shows the relation between Doppler velocity and continuum intensity at each height. At all the heights, the continuum intensity is higher when upflow exists, and is lower with downflow. While the slope of the scatter plot with a sigma of between 0.41 to 0.42 for all heights becomes flatter in the shallower layer. This means that the magnitude of velocity field depends on a height. Intensity of higher than 1.1 shows mostly upward motion, and that of less than 0.9 represents predominantly the downward motion and small number of weak upflow, holding a tendency of positive slope.
Next this correlation between the Doppler velocity field and intensity is investigated. A correlation coefficient A is defined as follows,

$$A = \frac{\sum_{i=1}^{n}(x_i - \overline{x})(y_i - \overline{y})}{\sqrt{\sum_{i=1}^{n}(x_i - \overline{x})^2}\sqrt{\sum_{i=1}^{n}(y_i - \overline{y})^2}}, \tag{4.1}$$

where x and y are variable numbers whose correlation we want to find, overline of x and y represents their averaged value. Fig. 4.4 is a correlation coefficient of the relation between the Doppler velocity and the corresponding continuum intensity, as a function of the intensity level used for deriving the Doppler velocity. The intensity range between 0.40 and 0.75, marked by the dashed lines, has a reliable result. The correlation coefficient decreases significantly with changing the intensity level from 0.75 to 0.40. By the way, in Fig. 4.1, Gaussian fitting result is also shown with the bisector results derived at different intensity levels. This fitting is based on a symmetric line profile, which is equivalent with that velocity fields are constant over height. To understand what derived velocity with Gaussian fitting shows, we compared its value with our bisector analysis results. Each line profile of Fe I 630.15 nm with wavelength from 630.1nm to 630.2 nm (Fig. 2.6) is fitted with a Gaussian function profile. Derived Doppler velocity with Gaussian fitting is calculated from wavelength shift between the center of the best-fitted Gaussian profile and the line center without motion. The panel (c) shows the sharpest correlation with an sigma of 0.10. Hence I conclude that the Doppler velocity derived by Gaussian fitting corresponds to higher layer. It is naturally understood because the fitting profile is mainly subjected to the shape of core profile.

In many researches, the Gaussian fitting of the spectrum is commonly used to derive the Doppler velocity. I compare the Doppler velocity field from such a derivation with those from the bisector analysis. The aim is to understand which height of the velocity is derived by Gaussian fitting. Fig.4.5 shows the correlation between the velocity from the Gaussian fitting and the bisector analysis. Three panels show the comparison with the different Doppler velocities in the bisector analysis. The panel (a) shows the averaged velocity derived by averaging the velocities obtained at intensity levels with the bisector analysis. The panel (b) represents the bisector velocity derived at the highest intensity level, close to the continuum intensity, for each spectral line. and (c) means the bisector velocity derived at the lowest intensity level, near the line core, for each spectral line. Velocity by fitted Gaussian profile shows a good correlation with one calculated by bisector analysis (Fig. 4.5 (a)). The absolute velocity calculated by bisector analysis is roughly identical to value by Gaussian fitting. Because velocity field of bisector analysis is nearly equivalent to that of Gaussian fitting, this bisector analysis can be regraded as a profitable tool to investigate the convective structure. The panel (c) holds a small scatter, compared to the panel (b), meaning the velocity field by Gaussian fitting represents at the higher layer.

As described above, these results are presented from dataset 1. We obtained the signature that is a increasing size distribution and decreasing the velocity with height. However, note that all the results in this chapter are for the Doppler velocities containing both convection and 5-minutes oscillation. As explained in section 1.2, the amplitude of 5-minutes oscillation is in the same order of the magnitude with that of convective motion. It is difficult to separate these velocity structures with dataset 1 because it takes 44 minutes for making this scanned map, which is much longer than 5 minutes. We need to analyze dataset 2, whose temporal interval is 2 seconds and much smaller than 5 minutes, to obtain the pure convective motion.

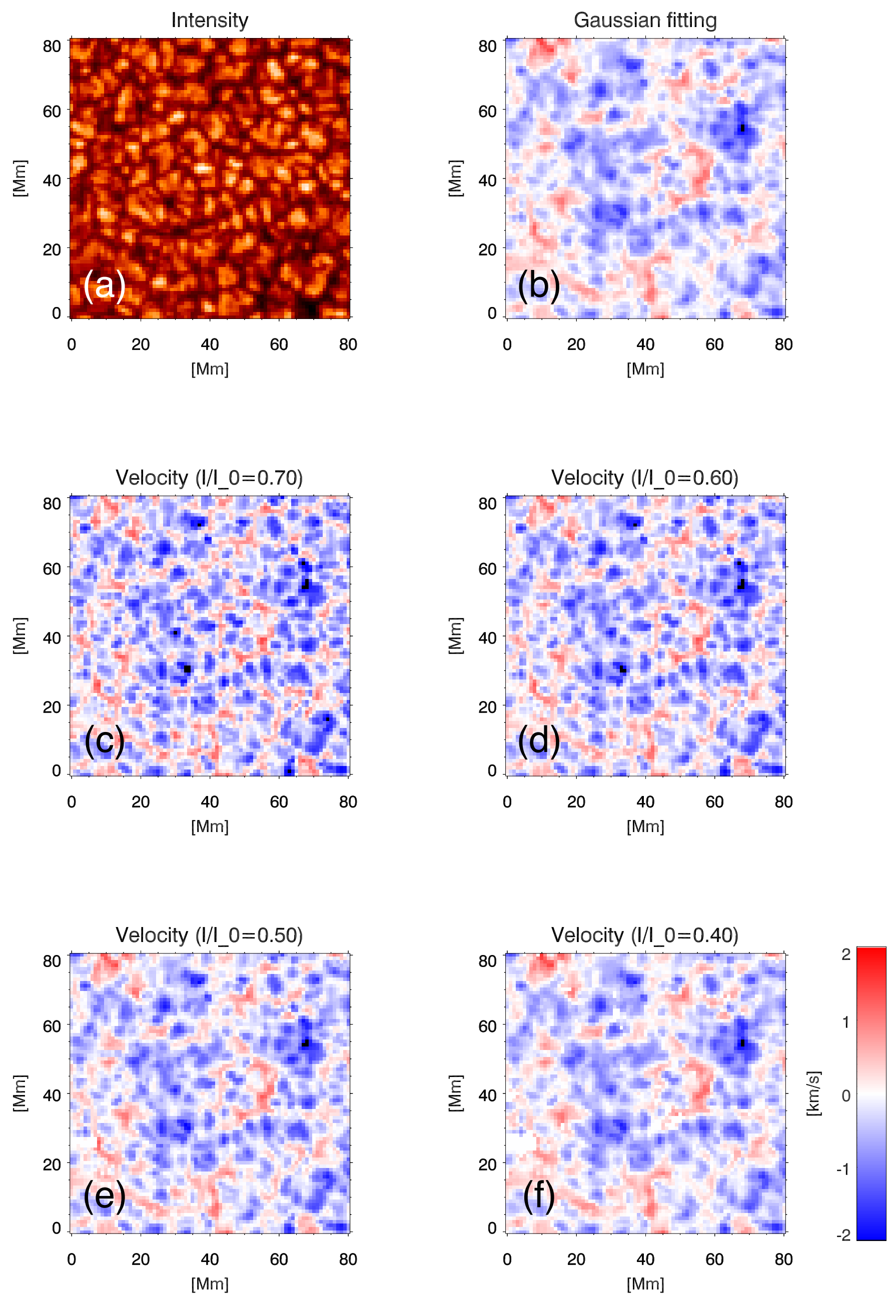

Figure 4.1: The distribution of continuum intensity image is shown in (a). Doppler velocity field are shown in (b) with Gaussian fitting, and at 4 intensity levels (c-f) with the bisector analysis. The positive (red) is the downward direction and negative (blue) is upward.

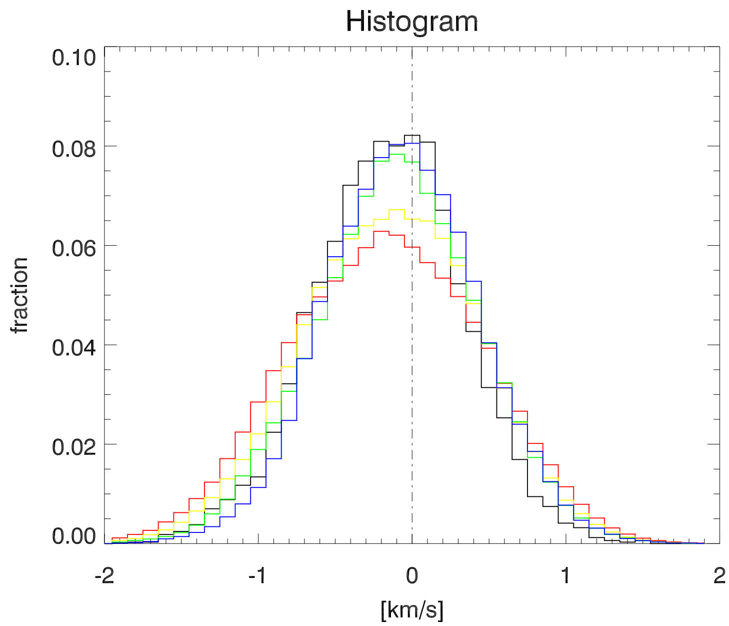

Figure 4.2: The number distribution of the Doppler velocity derived at each intensity levels with the bisector analysis. Blue: $I/I_0 = 0.4$. Green: $I/I_0 = 0.5$, Yellow: $I/I_0 = 0.6$. Red: $I/I_0 = 0.7$. Black: the number distribution of the velocity from the Gaussian fitting. The positive is the downward direction and the negative upward.

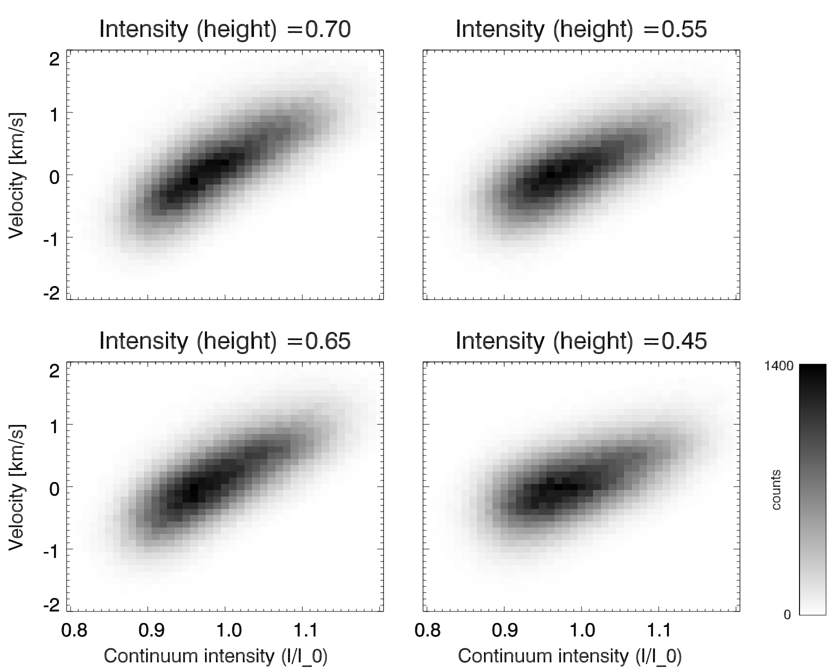

Figure 4.3: The relation of the Doppler velocity derived at 4 different intensity levels to the continuum intensity. The positive is the downflow direction and negative upward.

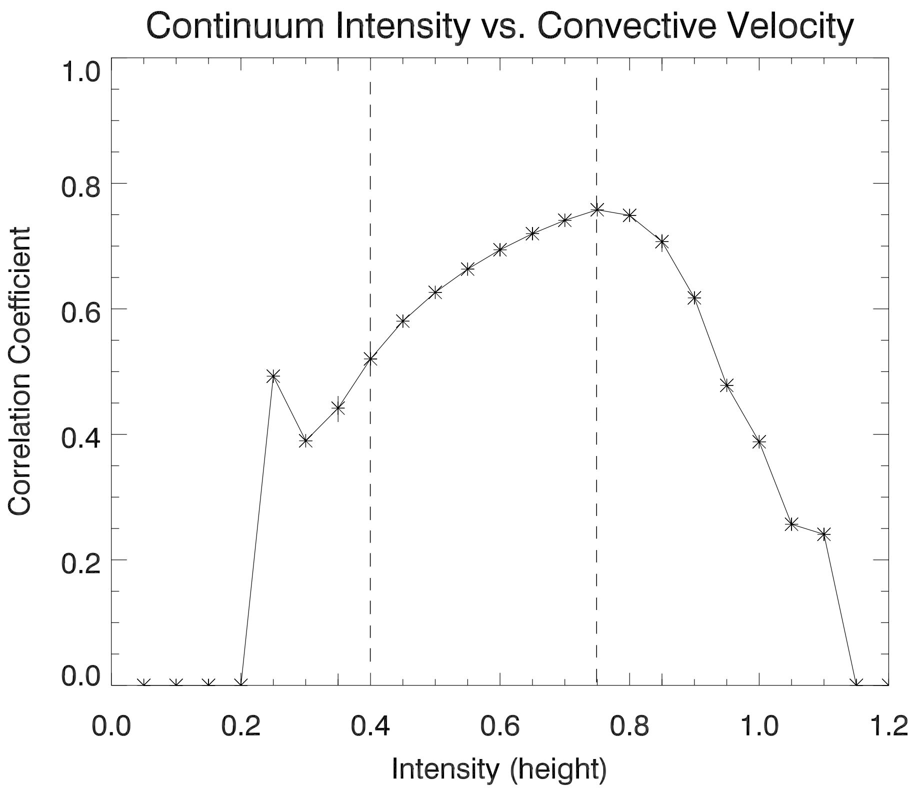

Figure 4.4: Correlation coefficient of the relation between the Doppler velocity and the continuum intensity, as a function of the intensity level used for deriving the Doppler velocity with the bisector analysis.

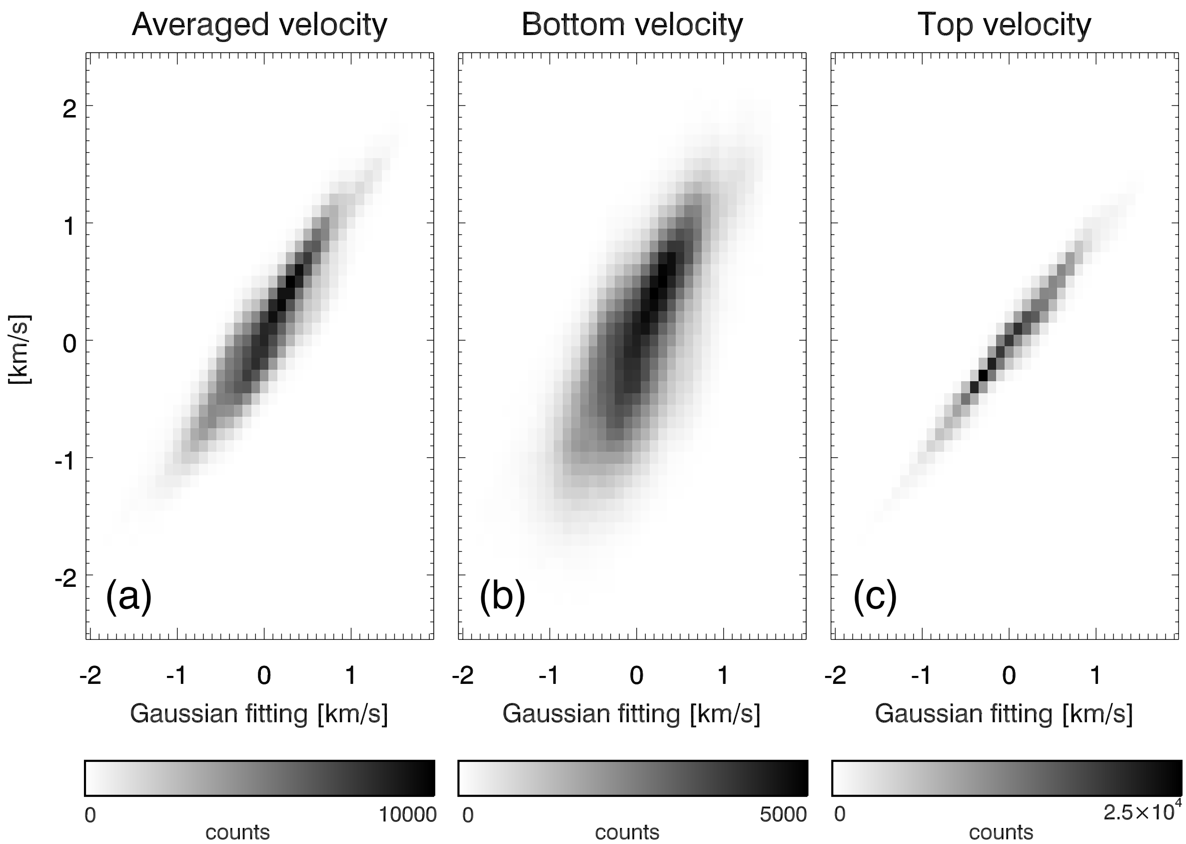

Figure 4.5: Comparison between the Doppler velocity derived by Gaussian fitting and those from the bisector analysis. (a) The averaged velocity derived by averaging the overall velocities obtained at intensity levels with the bisector analysis, used intensity levels are explained in section 3.1. (b) The bisector velocity derived at the highest intensity level, close to the continuum intensity, for each spectral line. (c) The bisector velocity derived at the lowest intensity level, near the line core, for each spectral line.

4.2 Separation of convection and oscillations

In this section, we separate the convective motions and velocity signals of 5-min oscillations. We need dataset 2, sit-and-stare mode observation data. Temporal series of spectral profile at certain time are obtained in the sit-sand-stare mode as explained in Section 2.1.2. Hence we can obtain time-distance map in dataset 2.

Fig. 4.6 shows the time-distance map of the Doppler velocity by applying bisector analysis to dataset 2. Similar to the results presented in section 4.1, stronger velocities are observed in both upward (blue) and downward (red) directions at the higher intensity levels. Their velocities are weaker at the lower intensity levels ($I/I_0 = 0.40$) close to the line core. On these diagrams, red colored island patterns, considered as 5-min oscillations, seem to be superposed on horizontal blue thread-like features, regraded as a granular convective motion. These periods of these variations are approximately 5 minutes, could be regraded as a 5-min oscillations. In the diagrams for the intensity level of 0.80 and 0.40, velocity was not derived at several points, which are denoted by white color, because either the continuum intensity is too low or the line core is high. The deficiency occurs in some part, making it difficult to separate the convective signal and 5-min oscillations through the Fourier transformation. In the diagrams for the intensity levels higher than 0.80 and lower than 0.40, more white areas are recognized. Hence our analysis is limited to the intensity level between 0.40 and 0.80. The white areas are usually located within the downflow regions, because the smaller line depth is observed in downflow regions, which are located in intergranular lanes and outside granules.

Next we apply the Fourier transformation to the velocity diagrams and obtain the k-ω diagrams at each intensity level shown in Fig. 4.7. The signals originated from the 5-min oscillations are discernible in range between 0 to 0.4 Mm^{-1} and 2 to 5 mHz (red and yellow in the figure). The power in that region increases with height.

In the next step, the subsonic filter was applied to the k-ω diagram in order to separate the velocities of pure convection and 5-min oscillation. The subsonic filter employed in this thesis is explained in section 3.3 and shown in Fig. 3.7. The region above the filter is considered as the velocity component of 5-min oscillations, while the region below the filter as velocity component of the convective motions. After the separation, inverse Fourier transform was applied and we obtained the velocities of the convective motion and the 5-min oscillations. These processes were performed at the time-distance diagram for the each intensity level. Fig. 4.8 shows the velocity diagrams before and after these processes. Fig. 4.8 (a) is an original time-distance diagram before the separation. Fig.

4.8 (b) and (c) shows the velocity diagrams of the pure convection and the 5-min oscillations respectively through the separation. It is clear from Fig.4.8 (b) that the oscillatory signals are well removed with the subsonic filter. Thread like patterns represent temporal evolution of granules at the slit position. Next I focused on the typical velocity field for convective motion and 5-min oscillations at each intensity level. Fig. 4.9 is the convection patterns for each intensity level, derived with the subsonic filter. The amplitude of the convection-oriented velocity patterns, including upflow and downflow, seems to be becomes smaller with height from the deeper layer to the higher layer. This means that strong upflows penetrate toward the higher layers, but the speed of upflows is gradually reduced with height. The time-distance velocity diagram Fig. 4.9 shows that blue intense threads match well with high continuum intensity, and upward velocity field is kept alive for the duration much longer than 10 minutes. Strong upward motion seems to be long duration and forms some high intensity feature, whose example is at the 5 -7 Mm position in the Fig. 4.9.

Finally, Fig. 4.10 is the correlation between the filtered velocity and the continuum intensity at 4 different intensity levels, i.e., 4 different heights. Note that transformation of scatter distribution with height: The slope of the correlation is steeper at the lower layer than the higher layer, meaning that at the lower layer trivial intensity affects largely on velocity amplitude rather than at the higher layer. This figure shows sharper correlation with a sigma of 0.33, 0.30, 0.26 and 0.23 for 0.70, 0.65, 0.55 and 0.45 of intensity level, compared to Fig. 4.3 of around 0.42 for all heights. The correlation between the continuum intensity and velocity in the vertical direction becomes good after removing 5-min oscillation component.

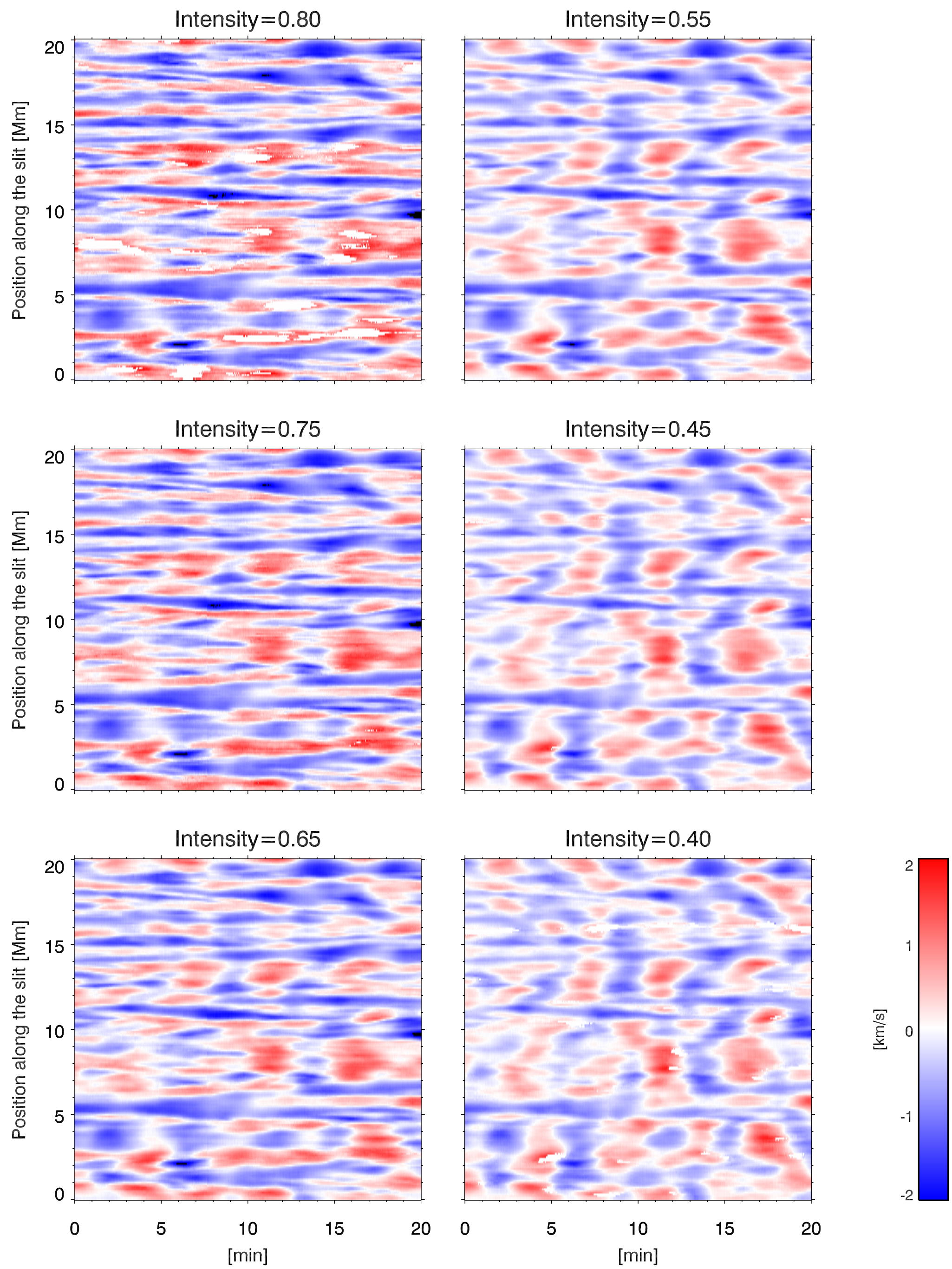

Figure 4.6: Time-distance diagram of the Doppler velocity derived at different intensity level. The intensity levels are 0.80, 0.75, 0.65, 0.55, 0.45, and 0.40 with height. The red color (positive velocity) shows downward velocity and blue does upflow velocity.

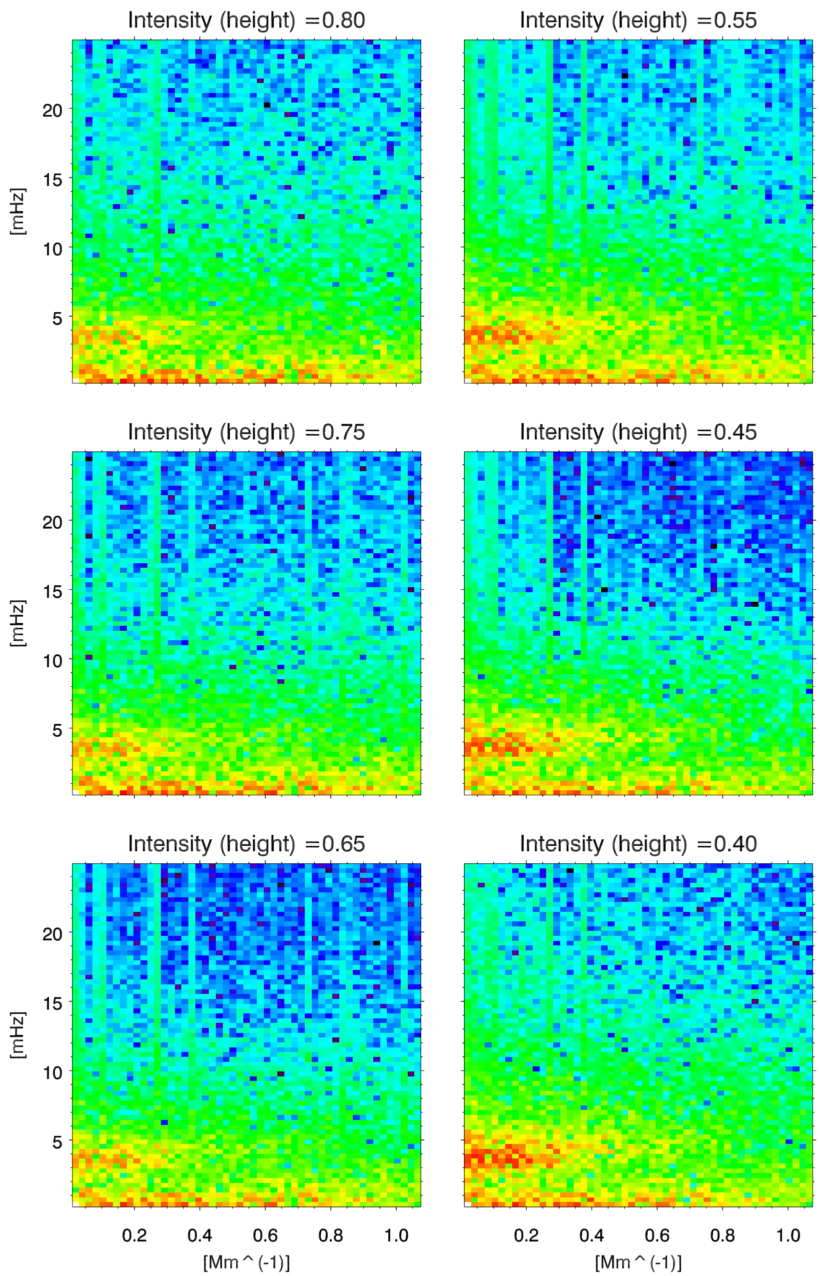

Figure 4.7: The k-ω diagrams derived from time-distance diagrams in Fig. 4.6. The horizontal axis is the wave number k Mm^{-1} and the vertical axis is the frequency ω mHz.

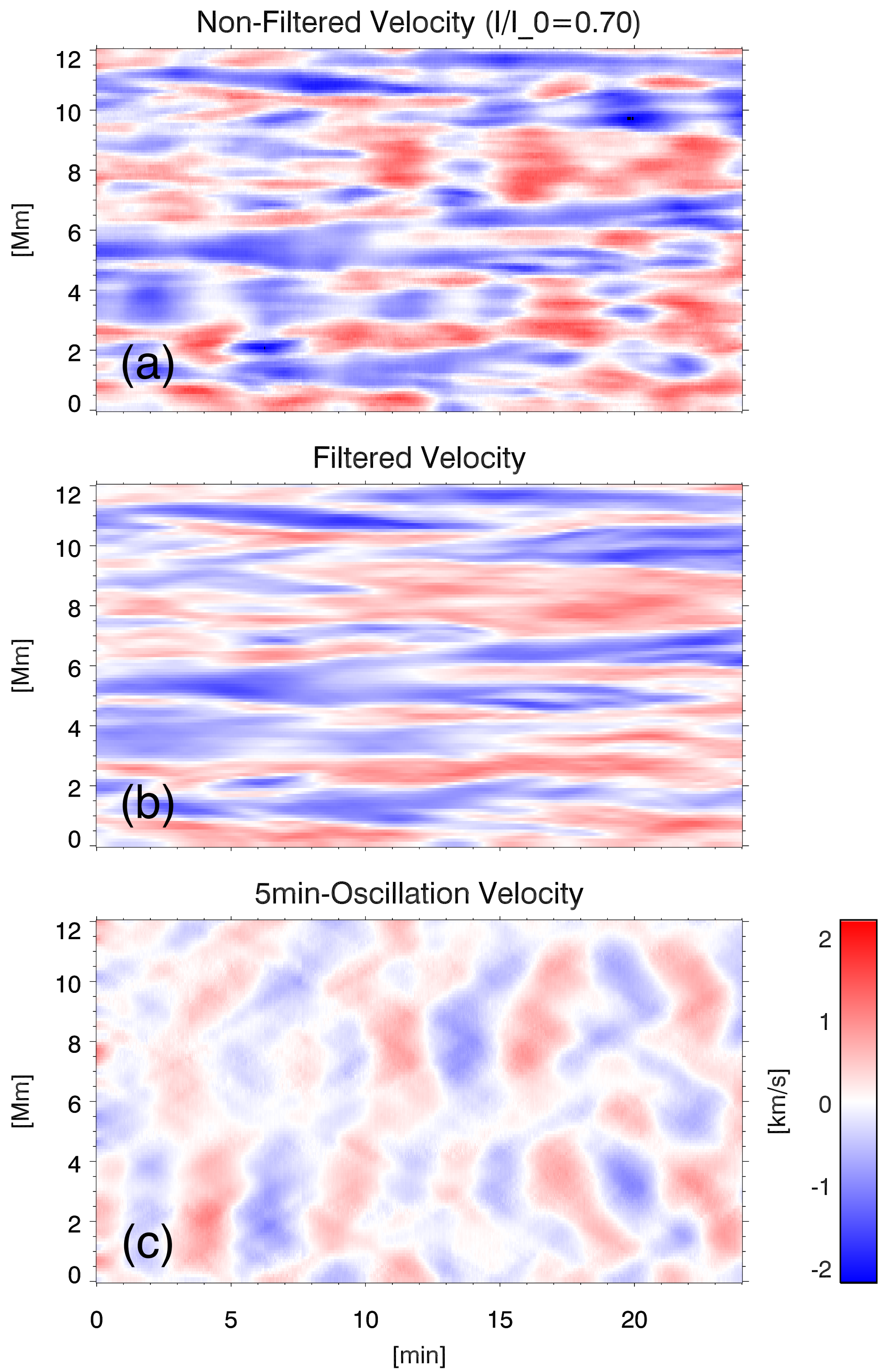

Figure 4.8: Time-distance diagrams of the Doppler velocity for the intensity level of $I/I_0 = 0.70$ before and after the subsonic filtering. (a) Time-distance diagram before the filtering. (b) The time-distance diagram for convective motion after the filtering. (c) The time-distance diagram for 5-min oscillations after the filtering. The positive (red) is downward and negative (blue) is upward.

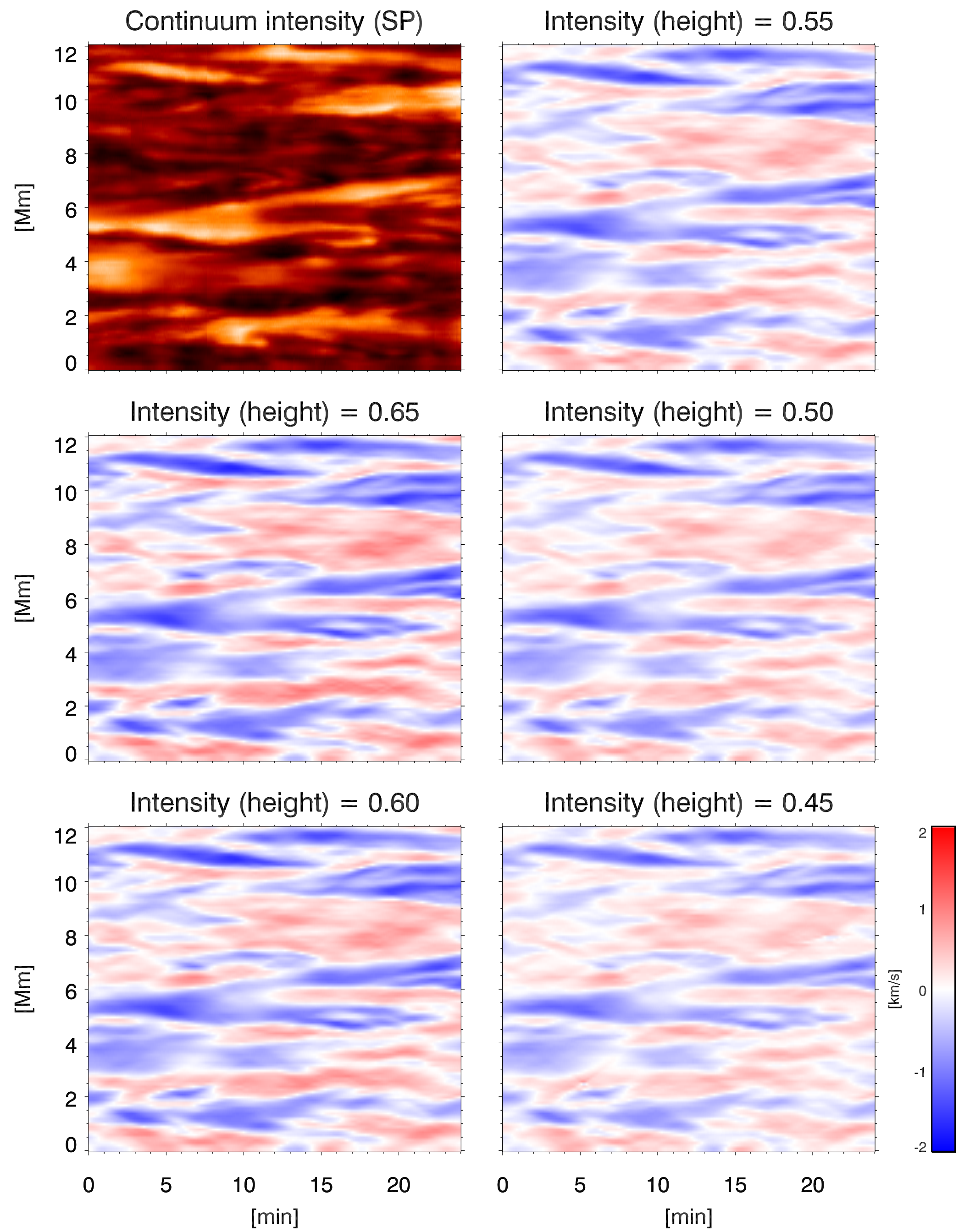

Figure 4.9: The time-distance diagram of the pure convective motion; for 5 different intensity levels and the panels correspond to the intensity level of 0.65, 0.60, 0.55, ⋯ 0.45 from up right to down right. The upper left panel is the continuum intensity. The positive (red) is downward and the negative is upward.

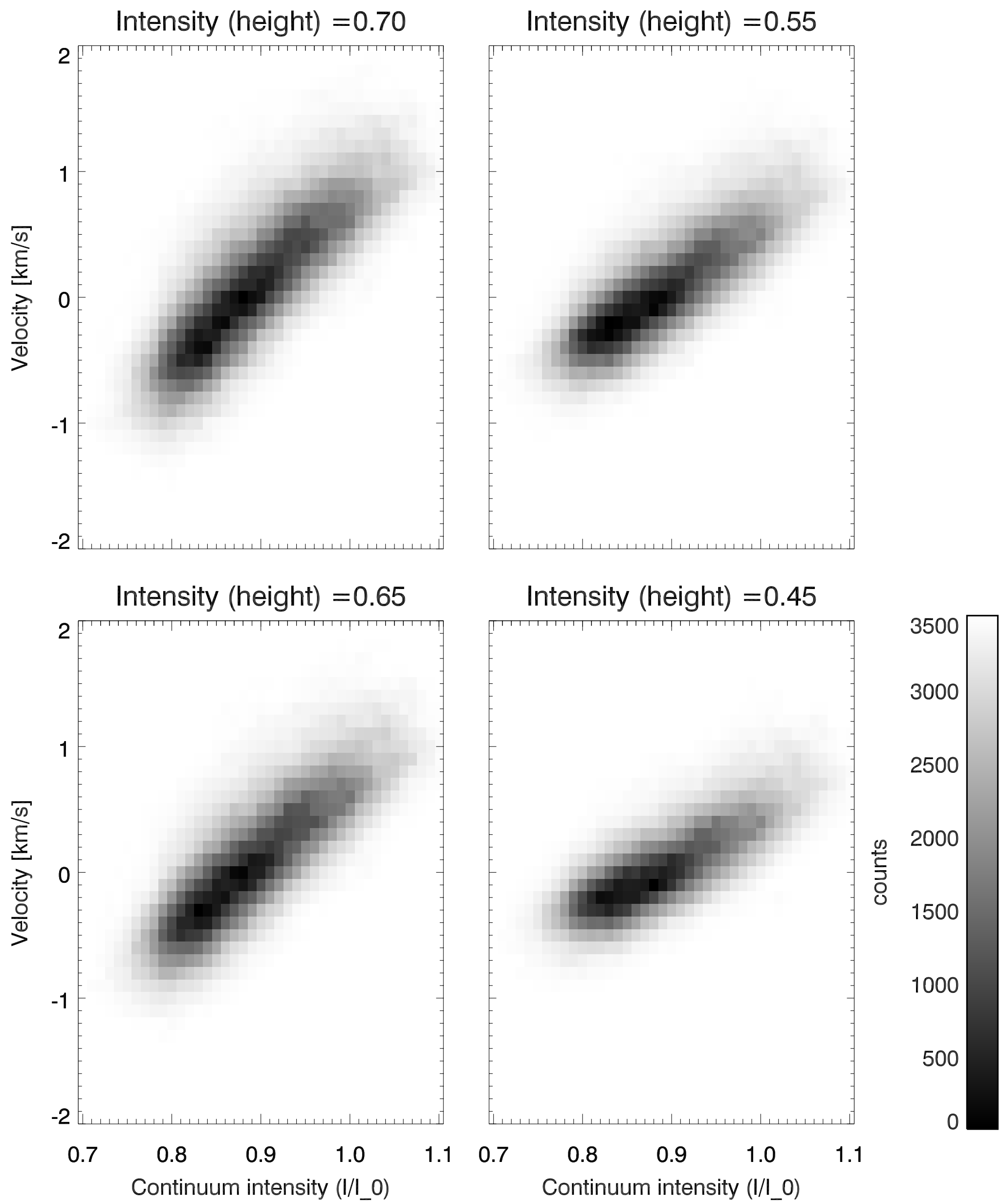

Figure 4.10: Scatter plots between the filtered velocity and the continuum intensity. The horizontal axis is the continuum intensity and the vertical is the RMS value of the Doppler velocity after removing the 5-min oscillation signal.

To investigate the distribution of velocity field at each height level, we created the histogram at each intensity level (Fig. 4.11). The non-filtered velocity has a wider distribution at the higher intensity level. From the filtered velocity histogram, the peak position of the distribution is shifted to +0.1 km/s, as the intensity level is decreased, i.e., going to higher layer. The shape of the histogram shows large asymmetry at the higher layer. At the downflow side, the number of the strong velocity more quickly decreases than the upward velocity. On the other hand, the histogram in 5-min oscillations has a symmetric profile for all the intensity levels, and the width of the distribution is larger at the higher layer, meaning that velocity field including both upward and downward increase s with height.

We also evaluate the skewness of the histograms for the quantitative evaluation of the asymmetry. Skewness, S, is defined as follow:

$$S = \sum_{i=1}^{n} \frac{(x_i - \overline{x})^3}{\sigma^3}, \tag{4.2}$$

where is a variable number whose skewness we want to find, $\overline{x}$ represents their averaged value, σ means is standard deviation. Fig. 4.12 shows skewness as a function of the intensity level in the spectral line for non-filtered, filtered and 5-min oscillation histograms. The sign of positive skewness means that upflows has wider distribution than downflows, i.e. there are large number of strong upward velocity fields. Non-filtered velocity and 5-min oscillations do not show a large variation with height. In the filtered velocity, skewness is around 0.05 at the intensity level of 0.75, i.e., at the lower layer, and it is gradually increased to 0.6 as going to the intensity level of 0.40, i.e. the higher layer. One interpretation of this asymmetry is that the stronger upflow survives until the higher layers and it makes the blue wing of the velocity histogram larger.

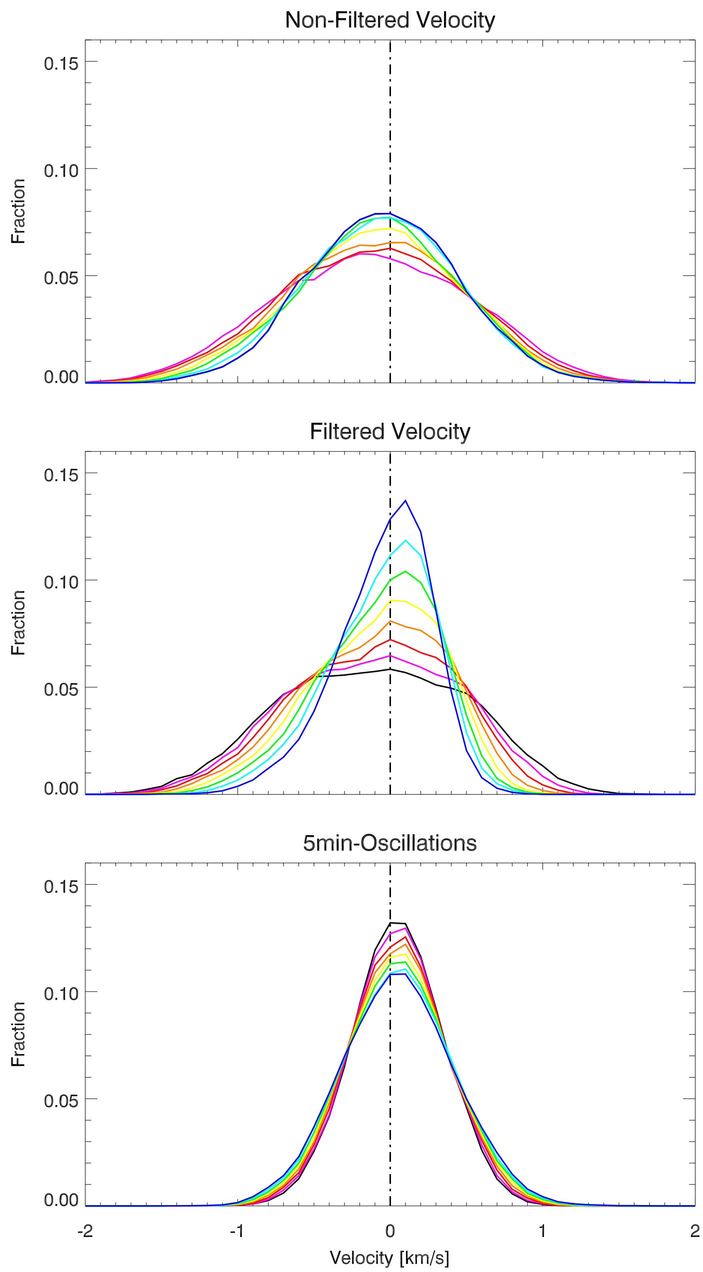

Figure 4.11: Histograms of original velocity, filtered convective velocity and 5-min oscillations. Colors show the intensity level in the spectral line, i.e. the height: Blue, light blue, green, yellow, orange, red, magenta, black equals to 0.40, 0.45, 0.50, 0.55 0.60, 0.65, 0.70, 0.75, respectively. The positive value is downward and negative is upward flow direction.

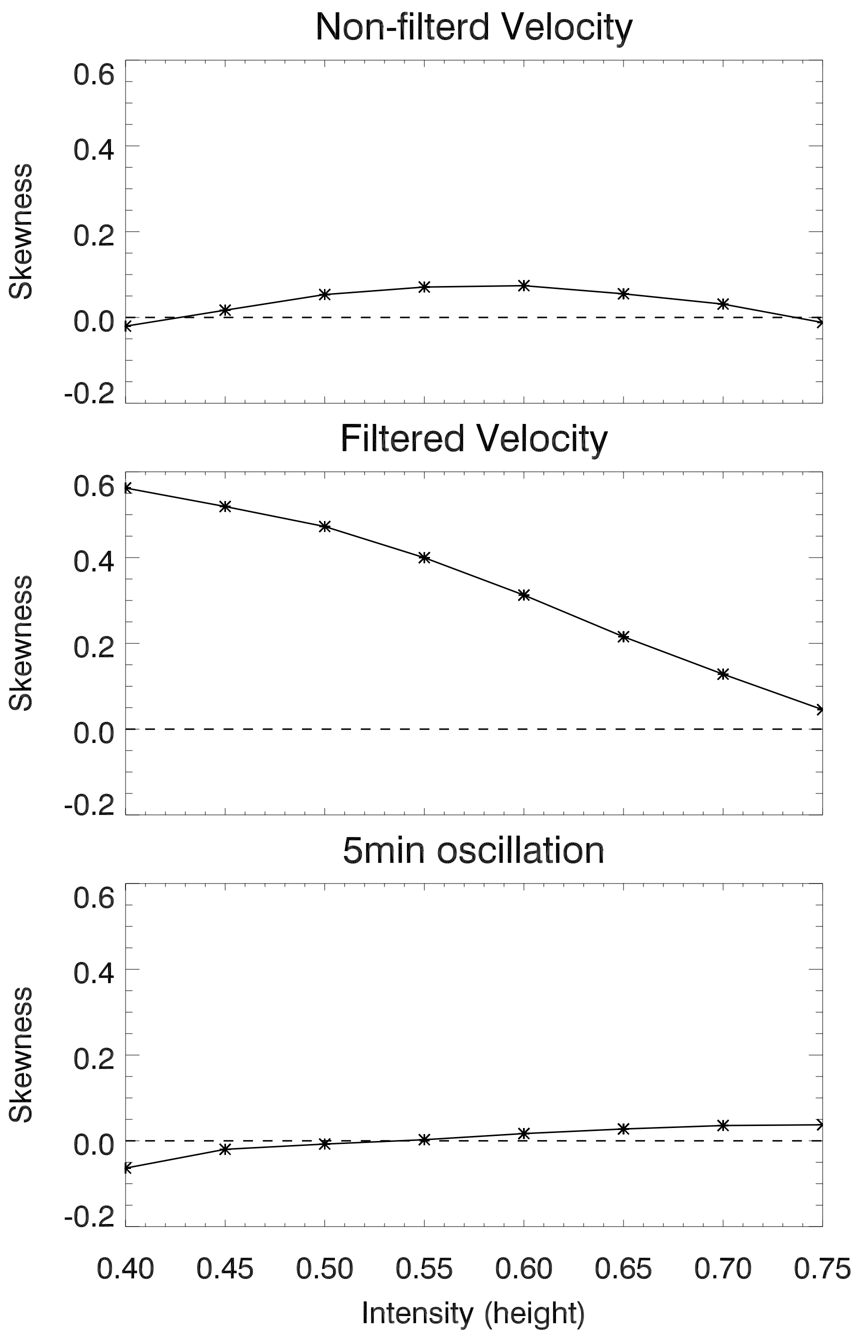

Figure 4.12: Skewness of the histograms (Fig. 4.11) as a function of the bisector intensity level. Positive skewness means that upflows are more dominant than downflows.

Next we investigate the height dependence of the velocity amplitudes. Fig. 4.13 shows the dependence of the root-mean-square of the original, the pure convection and 5-min oscillations velocity fields, on the different intensity levels. The range of the analysis is limited within the intensity level of 0.40 and 0.80 as explained in previous paragraph. The non-filtered velocity diagram, the RMS value of Doppler velocity gradually decreases from 0.7 km/s at the intensity level of 0.80 to 0.4 km/s at the intensity level of 0.40. The magnitude of convective motions is stronger at the lower layer and is gradually decreased toward at higher layer, because convective velocity decreases from 0.60 at the intensity level of 0.8 km/s to 0.3 km/s at the intensity level of 0.4. In contrast, the amplitude of 5-min oscillations is increased as going from the lower layer to the higher layer, because the RMS of 5-min oscillations increase from 0.3 km/s at the intensity level of 0.80 to 0.5 km/s at the intensity level of 0.40. These both convective and oscillatory tendencies depending on the height will be discussed in the term of the physical state of the photosphere in section 5.2. The amplitude of convective motion and 5-min oscillation are comparable at the intensity level of 0.45. At the higher than this intensity level, the Doppler signals by 5-min oscillations are chiefly dominant than the pure convective motions.

Next we compare this dependence of velocity amplitude with the granulation structure. The continuum intensity corresponds to the granular structure. Hence we investigate the height dependence of the RMS velocities with different continuum intensities. Fig. 4.14 shows the results of this. Four colors show different continuum intensity range; Red, green, blue, and black for the continuum intensity of lower than 0.9, between 0.9 and 1.0, between 1.0 and 1.1, higher than 1.1, respectively. The darkest continuum level, the red asterisks, corresponds to the intergranular lanes, whereas the brightest continuum intensity, the black one, corresponds to the granule. 5-min oscillations do not show significant difference among different continuum intensities. On the other hand, there is a significant difference in the amplitude of the pure convective velocity. In bright granules with the intensity higher than 1.1, the RMS velocity of upward flows exceeds 1.0 km at the intensity of 0.8, i.e., near the bottom of the photosphere. The RMS velocity is reduced to approximately 0.5 km/s as moving upward. At the top layer, the other color lines also show that the RMS velocity is decreased with height to about a half of the velocity observed at the bottom layer. The less the continuum intensity is, the less the RMS typical velocity is over height. The exception is the continuum intensity lower than 0.9, i.e., dark intergranular lanes, which show the RMS velocity (red) is slightly higher than that observed in the structures having the continuum intensity of 0.9-1.0 (green).

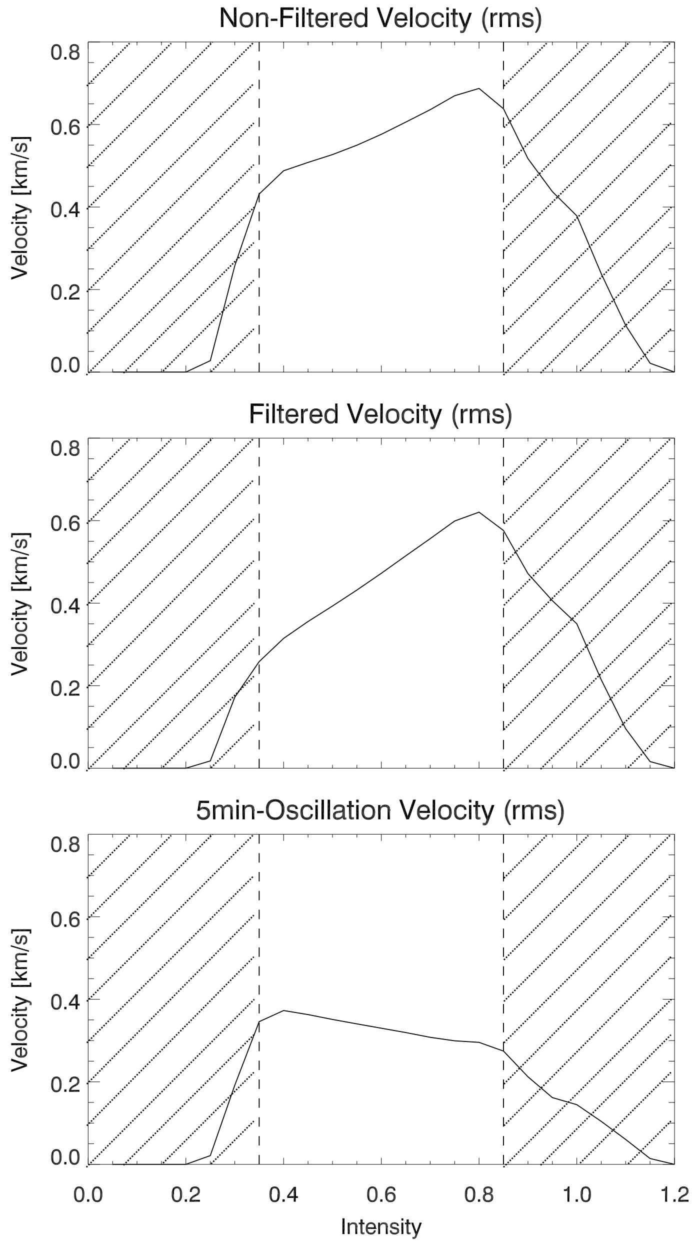

Figure 4.13: The Root-mean-square (RMS) value of the Doppler velocity in each time-distance diagram plotted as a function of the bisector intensity level. From the top to the bottom, the original velocity (non-filtered velocity), the velocity after removing the 5-min oscillations (filtered velocity), and 5-min oscillations. The intensity range between 0.35 and 0.85 gives a reliable result, as discussed in the text.

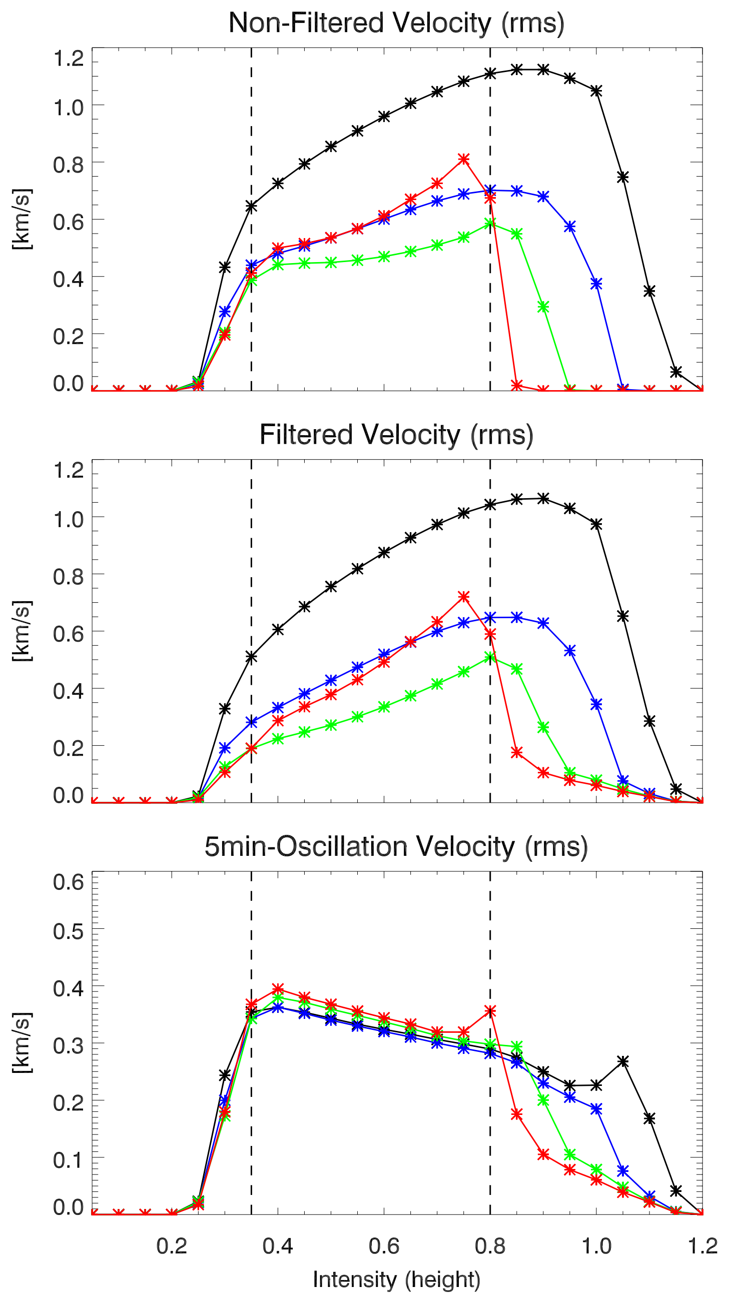

Figure 4.14: Same as Fig. 4.13, but for the different continuum intensity ranges: Red, green, blue, and black are for the continuum intensity of lower than 0.9, between 0.9 and 1.0, between 1.0 and 1.1, higher than 1.1, respectively. From the top to the bottom, the original velocity (non-filtered velocity), the velocity after removing the 5-min oscillations (filtered velocity), and 5-min oscillations. The bisector intensity level between 0.35 and 0.85 gives a reliable result, as discussed in the text.

4.3 Granular fragmentation

In this thesis, we also focus on the temporal evolution of the velocity structures in the vertical direction seen associated with the fragmentation of granules, in order to demonstrate the importance of knowing the vertical structures at the photosphere. We investigate the temporal evolution of velocity structure during the fragmentation of the convective cells (Fig. 4.9). We looks at the temporal evolution of the observed some typical convective structures using the convection patterns at each intensity level. First we pick up the fragmentation events in our observation. Filtergram images, not the spectral scanning data, is suitable for this purpose. Dataset 2 contains such a 4 filtergram images. Fig. 4.15 shows that blue continuum intensity, continuum intensity along slit, filtered velocity structure and 5-min oscillations from the top to the bottom at a certain moment. We can see a good correlation between the velocity field in the convective structures and blue continuum intensity. In the filtered velocity, downflow regions are located around dark regions, which has the intensity less than 1.0; at 0.6, 2.4, and 4.8 Mm from the left edge in the figure. There are remarkable two bright regions, larger than intensity 1.1, at 3.5 and 5.3 Mm. Strong upflows are located there. There is also a peculiar region which does not obey the standard relationship between the velocity and the convective structure. One example is that the fast upflow occurs at 1.9 Mm, where the continuum intensity is not so high, around 1.05. In contrast to the distribution of convective structure, the velocity field of 5-min oscillations does not seems to be affected by granular structure, i.e. continuum intensity.

Fig. 4.16 is the time sequence of Doppler velocities by convective motions (left) and by the 5-min oscillation (right) in the slit-height domain. The time interval of the sequence is 10 second. In this period, time variation of convective velocity field does not appear significantly, whereas the changes of 5-min oscillations are clearly seen at 1.4 and 4.5 Mm. The velocity structures by the 5-min oscillations are widely propagated, and they are not associated with the intensity morphology of granular structures.

In this paragraph, time evolution of filtered convective structure in granular fragmentation was just observed on the slit. Fig. 4.17, Fig. 4.18, Fig. 4.19 and Fig. 4.20 show the temporal evolution of convective structure. In each figure, the number given above each continuum image frame is the frame position in the series of FG images. Since FG images were taken every about 30 sec, the number can be used to know the time scale.

The example 1 in Fig. 4.17 is described. In image 0, granule has clear round shape. Next image 4, intensity of granular center starts to decrease, and drastically decrease in image 6. In the right part of image 4, intensity suddenly soar and upper velocity rises. Downward flow appears at higher layer over fragmented granular region in image 8 reaches the bottom in image 12.

The second example is shown in Fig. 4.18. In image 5, the intensity gradually drop in the center, keeping upflow. In the right side of this figure, bright granule is newly created through the fragmentation of old one. In image 8, dark region of the granular center is clearly seen. The downflow suddenly appears on the inergranular lane in image 10. In image 11, convective velocity structure is same as image 10, whereas the continuum intensity decreases and reach the 0.9 of continuum intensity.

The third example is shown in Fig. 4.19. In image 6, the granular has triangular shape next to left side of bright feature. Whole region of granule decrease their continuum intensity and upward velocity in image 13. The downflow appears at the higher layer in image 14. In image 15, downflow covers whole height. The continuum intensity decreases and dark intergranular region is formed.

Finally, the example 4 in Fig. 4.20 is described. In image 65, bright granule can be identified and has a strong upward velocity. The decrease of continuum intensity can be seen in image 70. In image 72, downward velocity appears at the higher layer. After 30 second, in the image 73, descending motion reaches the lower layer. Convective structure is almost same as image 72, continuum intensity keep decreasing.

Common feature among these four cases is that downflow signal appears at the top layer and gradually is developed toward the deeper layer after the center part of granule split. The downflow signal appears when the intensity is reduced to around 1.0. The development of the downflow from the top layer to the deep layer takes place in a short timescale, i.e., less than 30 sec, which is compared to the timescale of the evolution seen in typical convective structures in Fig. 4.16. Even after the downflow is dominated over the whole height, the continuum intensity continues to decrease and forms a dark intergranular lane.

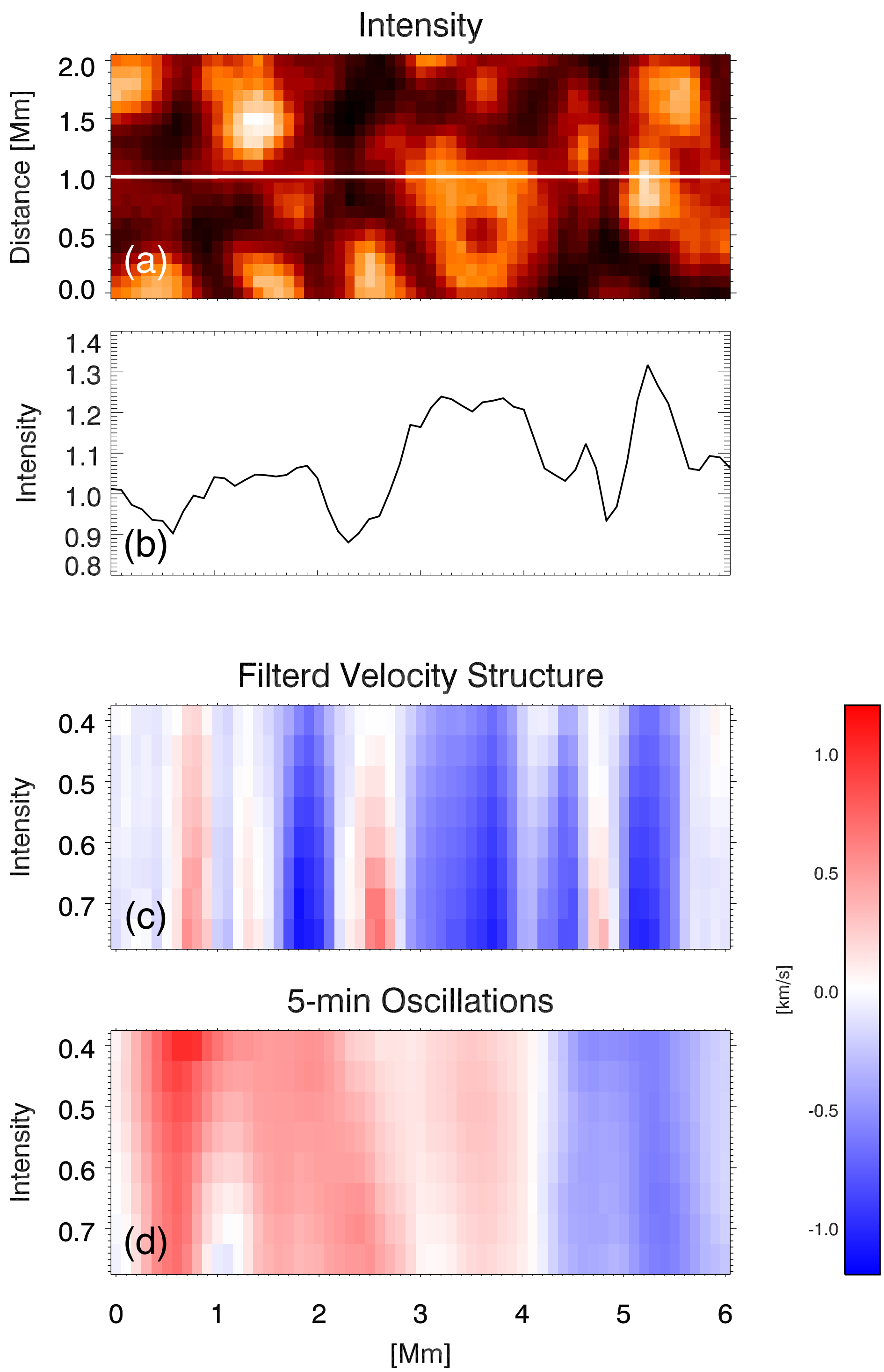

Figure 4.15: A snapshot of the space - bisector intensity level (i.e., height) map of the Doppler velocity (c) and the amplitude of 5-min oscillation component (d) for a slit, which position is given in the blue continuum image (a). (b) the intensity profile of the blue continuum at the slit. The data was acquired at 23:31:01 UT on 6 July 2014. The positive value (red) is downward and negative (blue) is upward flow direction.

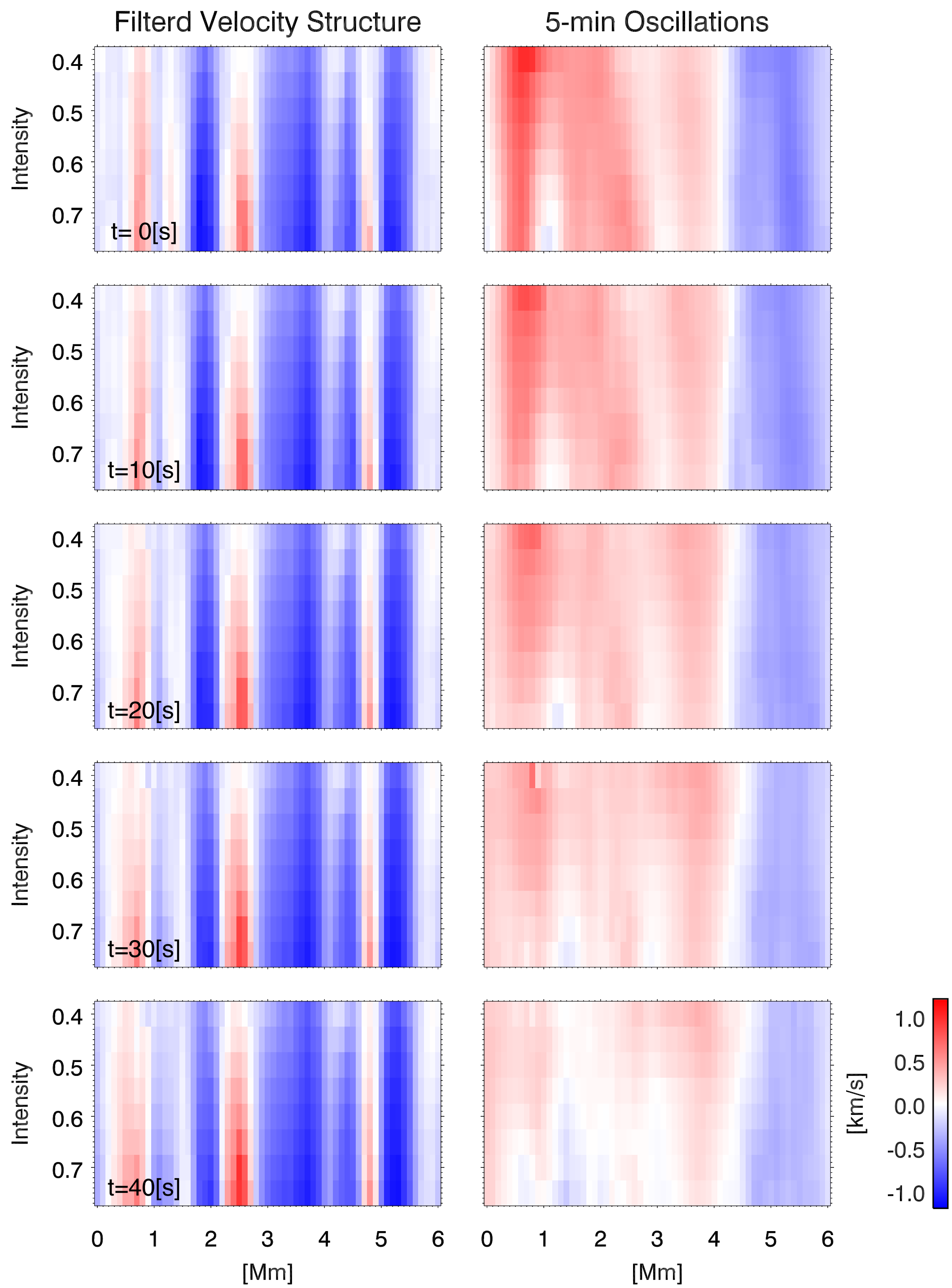

Figure 4.16: Time sequence of velocity field of convection and 5-min oscillations. *Left*: Filtered velocity. *Right*: 5-min oscillations. Time increases by 10 second between consecutive frames (from top to bottom). The positive value (red) is downward and negative (blue) is upward flow direction.

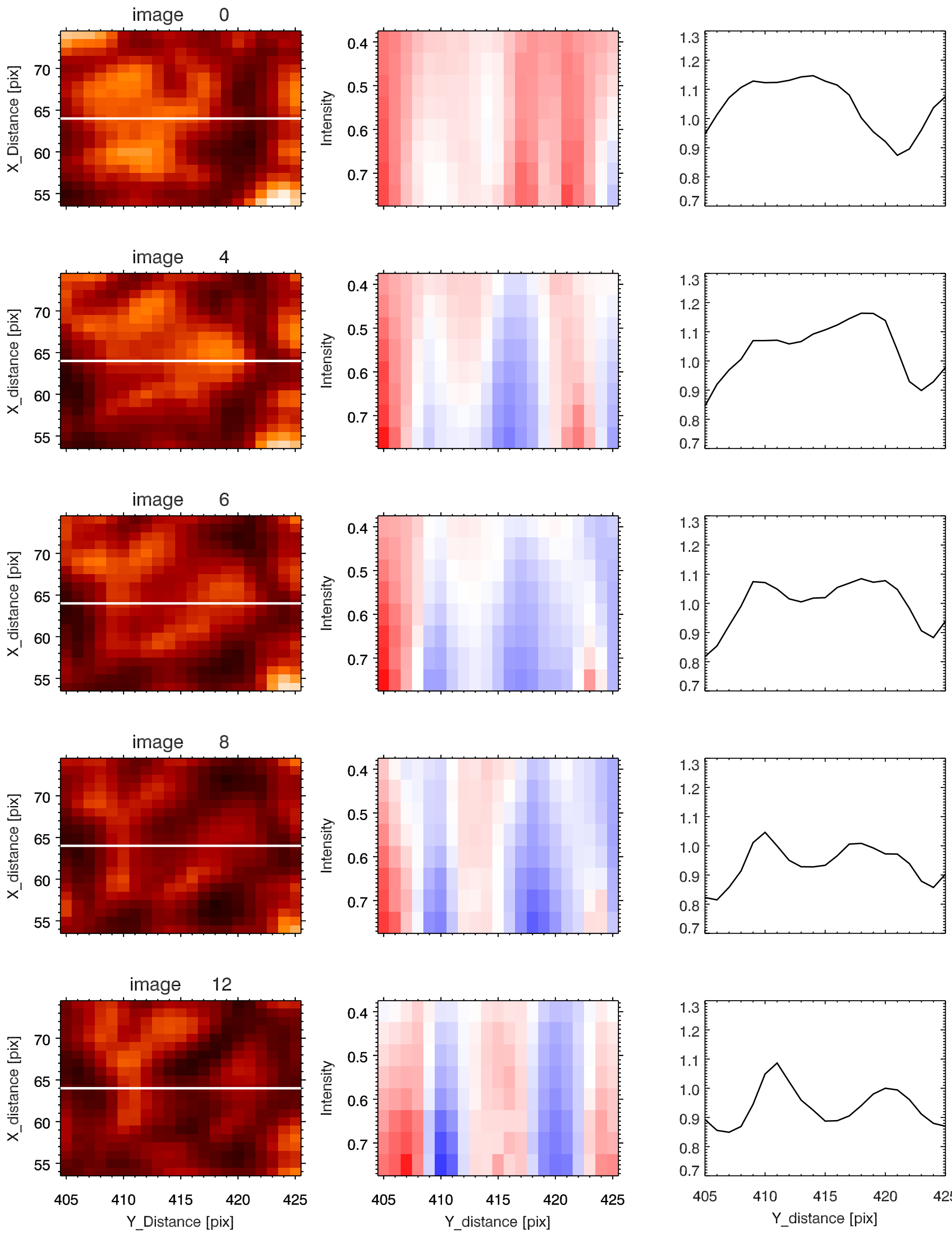

Figure 4.17: Time evolution of velocity structure in a fragmenting granule. This granule is defined as Example 1. *Left*: Blue continuum intensity. White line marks SP slit position. *Middle*: Filtered velocity structure along slit. *Right*: Blue continuum intensity along slit. The red shows downward and blue represents upward flow. One pixel size corresponds to roughly 0.11 Mm.

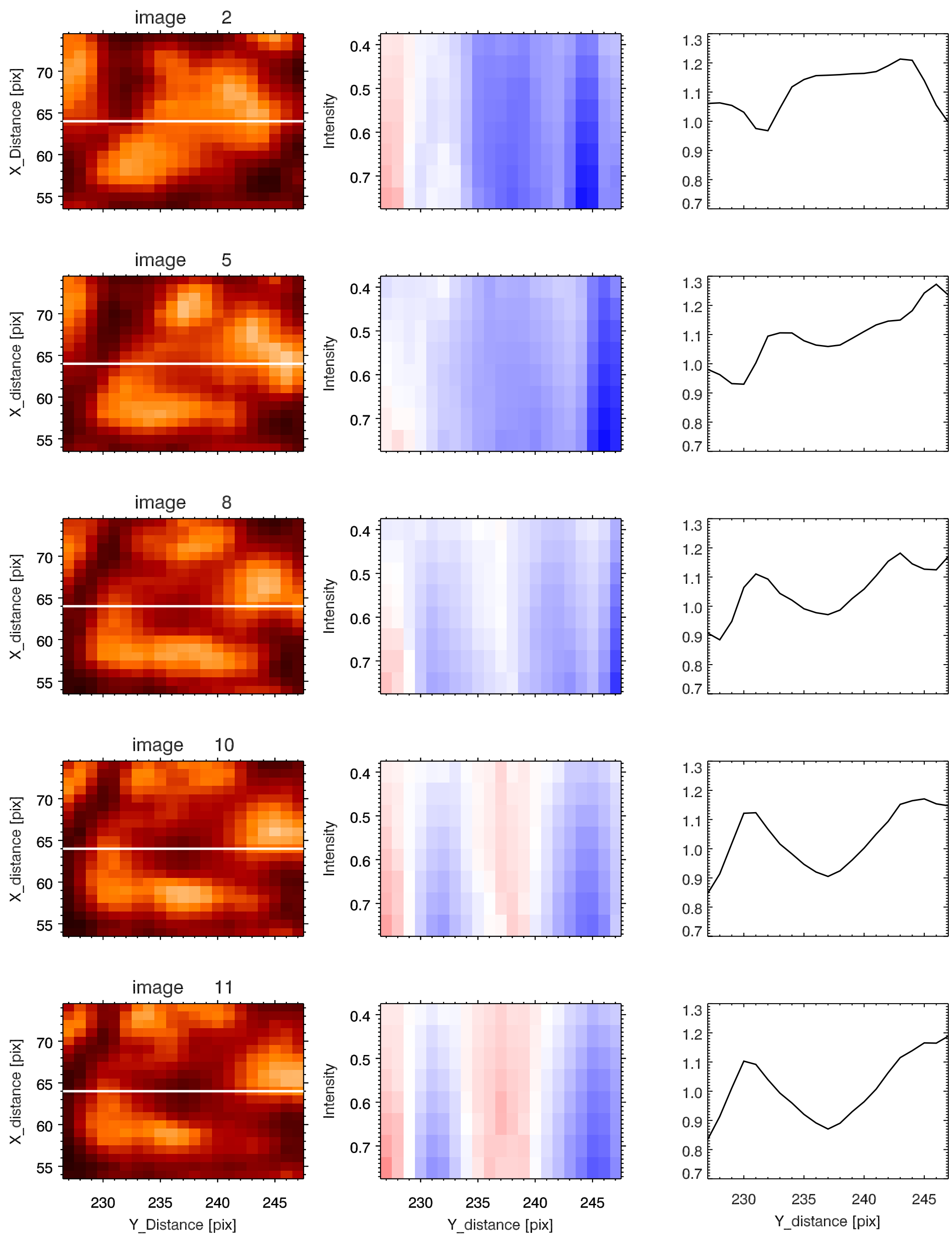

Figure 4.18: Time evolution of velocity structure in a fragmenting granule. This granule is defined as Example 2. The meaning of panels and axis are same as Fig.4.17.

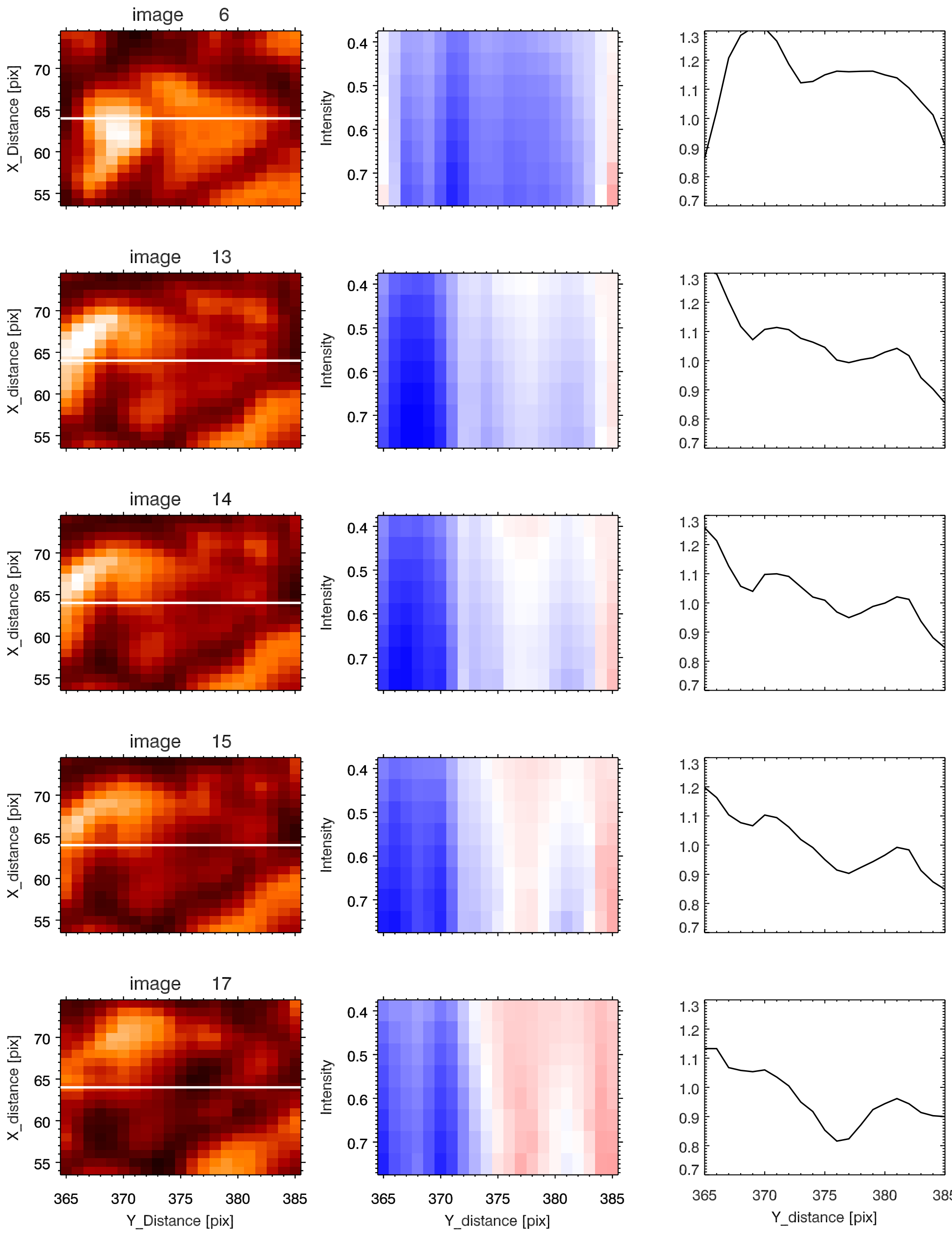

Figure 4.19: Time evolution of velocity structure in a fragmenting granule. This granule is defined as Example 3. The meaning of panels and axis are same as Fig.4.17.

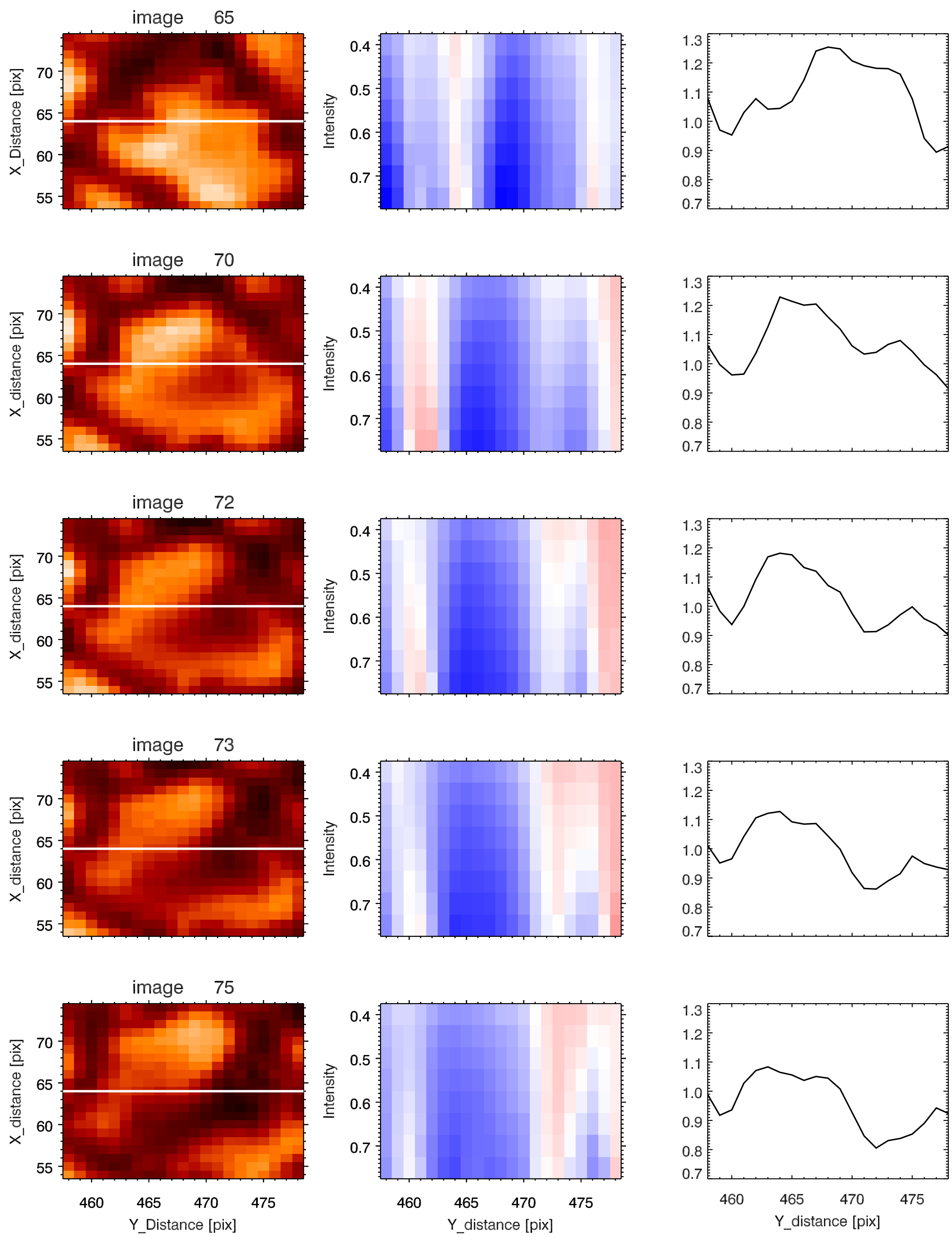

Figure 4.20: Time evolution of velocity structure in a fragmenting granule. This granule is defined as Example 4. The meaning of panels and axis are same as Fig.4.17.

Chapter 5

Discussions

5.1 Velocity field at different heights

5.1.1 Convective structure

We separated convective structure and 5-min oscillations from vertical velocity structure through Fourier transformation. Properties of 5-min oscillations and convective structure are derived. We discuss the convective structure from four point of views based on our results.

Hot upward materials are successively supplied from below the photosphere at a location for a fairly long duration, forming series of granules. Bright region matches well with upward velocity field (Fig. 4.9). Long life granules maintain the continuous upward motion. However, some parts of convective velocity field do not obey these correlations. These exceptional cases are seen during granular generation and extinction. At the beginning of granules, upward velocity field exist in relatively lower continuum intensity (see the coordinate from 0 to 5 min and 1 to 2 Mm; from 10 to 13 min and 9 to 10 Mm of Fig. 4.9). Upward velocity field is kept even after the end of some granules, nevertheless they also do not have a high continuum intensity (see the coordinate from 10 to 15 min and 10.50 to 10.10 Mm of Fig. 4.9). These facts indicate that upward gas flows are excited on the solar surface for the duration longer than the lifetime of granules. Supplying hot materials to the surface may form a bright feature, i.e., a granule. Thus, upflows can form granules, although high-intensity granules may not be generated only with weak upward flows.

Second, in a bright granule, strong upward motion keeps its velocity with little decreasing in the formation layer of the Fe I 630.15nm line. In most areas excepting the strong upflow regions, the velocity are decreased as going to the higher part of the formation layer. Fig. 4.11 and Fig. 4.12 show that the number distribution of convective velocity indicates strong asymmetry with height. In bright granules, upward velocity keeps its value with slightly decreasing at the higher layer. According to Fig. 4.14, the typical value of upward motions at the area with the continuum intensity higher than 1.1 is 0.65 km/s at higher layer. On the other hand, at most of the area with the continuum intensity lower than 1.1, both upward and downward velocities decrease to approximately 0.2 km/s.

Third, the tendency, which is increasing downward velocity with depth, is a surprising fact. The photospheric layer has been regarded as a convective stable layer by standard solar model. According to our result, granular region corresponds to convective stable layer on the ground that upward motion is decelerated with height. However, our results show that downflow is accelerated with depth, meaning that intergranular lane is not subjected to the standard solar model. I suggest a scenario to explain this acceleration: After ascending material is effectively affected by radiative cooling because of less density, it decreases the temperature and obtain high density. As a result, higher density materials, compared to surrounding, is more subjected to being gravitational pulled down, causing acceleration.

Fourth, we discuss the observed amplitude (in RMS) of convective velocity by comparing with a previous work. From Fig. 4.13, the vertical RMS velocity decreases from 0.65 km/s to 0.25 km/s with height. These values are significantly larger than those in the previous work (Kostik & Khomenko 2007). According to their result (Fig. 5.1), the upflow speed in granular region is decreased from 0.2 km/s to 0.1 km/s over 300 km which is an estimated maximum height of our studied range (see Fig.3.3 in section 3.1). Similarly, in intergranular region, the downflow speed is decreased from 0.2 km/s to 0.1 km/s. Since ground-based telescopes may capture the degraded spectral data due to the atmospheric seeing, the observed absorption lines are blended with blue and redshifted one, resulting in inaccuracy in the observed wavelength shift. Thus, the observed wavelength shift may be smaller than that obtained in our studies. It indicates that spectral data observed with high spatial resolution allows us to investigates the convective structure in detail.

5.1.2 Spatial 2-dimensional velocity structure and effect of 5-min oscillations

We analyzed dataset 1, the spatial two-dimensional map with slit scan mode. At first, we will discuss the character of upward and downward motion depending on the height. Both upward and downward velocities also decrease with height (Fig. 4.1and Fig. 4.2). This tendency is same as pure convective motion (section 5.1.1). The photospheric convection is an overshooting from subsurface which is a convective unstable layer. Because the photosphere is a convective stable layer, upward motion originating from the subsurface is decelerated with height. In the case of intergranular lane, downward velocity increases with depth. This may explained by the scenario described in section 5.1.1. This same tendency represents that velocity field including 5-min oscillations with slit scan mode can be applied to capture the character of three-dimensional convective structure.

From this paragraph, we will discuss a height dependence of the coincidence between the Doppler velocity and continuum intensity structure. At the lower layer, it seems that downward and upward flow corresponds well to granular structure. At higher layer, velocity field has larger spatial scale structure and the granular shape of convection is kept in the areas with strong upflows. It means that upward flows spread out horizontally with height and contribute to form a larger spatial scale of velocity field.

However, we should pay attention to one possibility that oscillatory motions characterize those properties. The correlation coefficient of velocity field drops with height (Fig. 4.4). It is obvious that oscillatory motions affect significantly on velocity field, in particular at higher layer. This is explained by character of both convection and oscillatory motions (Fig. 4.13). Convective velocity typically loses its velocity with height; Contradictory to decreasing convective velocity, oscillatory motions strengthen with height. At the height above intensity level of 0.45, typical velocity of 5-min oscillations becomes comparable to that of the convection. Since oscillatory velocity field has a spatial scale much wider than granular one, 5-min oscillations also contributes to form a larger spatial scale velocity field with height. Regardless of being affected by 5-min oscillations, strong upward region in bright granule keep their shape at the higher layer. According to Fig. 4.14, we can explain this reason. The RMS velocity of the convective motions is 0.65 km/s at higher than continuum intensity 1.1, while that of oscillatory motions is around 0.4 km/s. The RMS velocity becomes less than 0.3 km/s in the lower continuum intensity. Consequently, bright granules still keep upward patterns at higher layer, although oscillatory motions affect on velocity field. In lower continuum intensity mainly affected by oscillatory motions and may change their sign of vertical velocity.

5.1.3 5-min oscillations

Next, we discuss the property of the derived 5-min oscillations. At first, the verification of derived 5-min oscillations with our bisector method is shown by comparing our results with previous work. Our results show that the amplitude (in RMS) of 5min oscillations increase from 300 m/s to 400 m/s. This increasing amplitude is compatible with that in past works. Kostik & Khomenko (2007) applied bisector analysis to spectroscopic from a data of ground-based telescope (Fig. 5.1). According to their results, the amplitude

increases from the 300 m/s to 350 m/s with height from 100 km to 300 km. The height range of our results with Fe I 630.15 nm is roughly 0 - 300 km, and thus our result is in agreement with the Kostik & Khomenko (2007) result. In contrast to convective motion, it seems that the result of the oscillations based on ground-based telescope is not affected by atmospheric seeing because of the following two reasons. At first, Fig. 4.14 shows that there is no significant their amplitude dependence of the observed velocity amplitude on the continuum intensity. Thus, oscillatory motions appear on granular and intergranular regions equally independently of location. Second, the 5-min oscillation is a phenomenon with large scale. The spatial size of the 5-min oscillation signals is roughly over 3-4 Mm in the photosphere, which corresponds to 4"-6" (Fig. 4.8). These two results suggest that signals of 5-min oscillations can be observed on the velocity field data even if the observations have the spatial resolution lower than 1". As a result, ground-based observations could also capture the oscillatory signals adequately, even though atmospheric seeing degrades their spatial resolution.
(That means that the similar amplitude of velocity is observed at the location 4"-6" apart at the same time. The most of the boundary between blue and red colored region are declined on the Fig. 4.8 (c). This is a propagating phase difference,meaning that the incidence of wavefront of 5-min oscillations is not vertical to the surface.)

The fact that oscillatory motions strengthen their amplitude with height is not surprising when we consider the density changes in the photospheric atmosphere. In the solar atmosphere, the density is decreased toward the upper atmosphere, increasing the amplitude of the propagation waves as they propagate upward. According to Vernazza et al. (1981), the density decreases to one-tenth from the continuum level to the top of the line formation height of Fe I 630.15nm.

In the future, our bisector analysis would be a useful tool to investigate the behaviors of the 5-min oscillations in the atmosphere. Desirable dataset dedicated to analyze the 5-min oscillations should be observed for adequate long duration and in large field of view.

It is because longer and larger continuous observations enables us to depict the detailed power on the k-ω diagram in lower frequency and wave number. Those time and spatial range of spectroscopic data analyzed in this study are short to investigate it in detail: It has the slit length that is a half of the actual slit the instrument has; The duration of the observations analyzed in this study is just 44 minutes. Recently, we succeeded to obtain the spectral data with the full length slit 164 ″ and long-term 7 hours by using the *Hinode* satellite. The duration of the observation is ten times longer than that of observations used in this study. If a discrete ridge on k-ω diagram were discernible by using the new data, we may capture how one compressional wave behaves over height in detail.

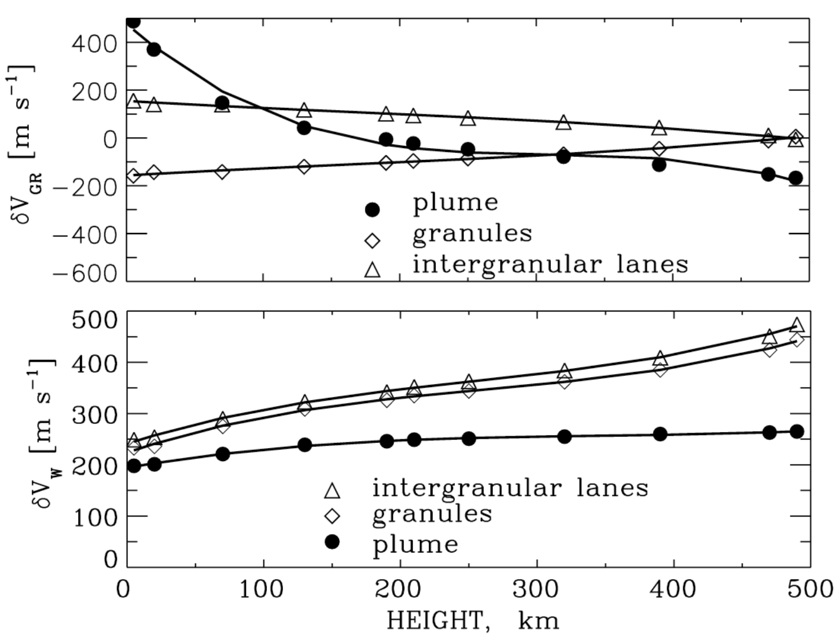

Figure 5.1: Velocity field with height (Kostik & Khomenko 2007). *Top*: Convective velocity with height. Positive value is downward velocity, and negative value is upward. *Bottom*: The amplitude of 5-min oscillations.

5.2 Granular fragmentation

In this study, we captured four examples that allow us to trace the time evolution of convective structure during granular fragmentation. At first, to compare these examples with the previous numerical and observational studies, we review the previous works here.

Based on numerical simulations, some authors have suggested physical process of fragmentation. Stein & Nordlund (1998) and Rast (1995) showed the granular fragmentation in radiative three-dimensional simulation and two-dimensional simulation, respectively. The scenario of fragmentation proposed by these researchers is summarized with Fig. 5.2 below: Hot gas materials are successively supplied from below the photosphere in the areas where granules are formed. The photosphere, which is a convective stable layer, behaves as a wall for ascending materials and pushes the hot materials to the horizontal directions (Fig. 5.2(a)). When the granule becomes too large, horizontal flows cannot push out all the supplied materials and a high-density parcel is developed near the center below the granule. Central excess pressure restrains ascending flow from penetrating through parcel (Fig. 5.2 (b)) and the ascending flow spreads around (Fig. 5.2 (c)). In the center, the high-density parcel loses the energy, and material loses its hot supply and decreases the temperature thorough radiative cooling. On the other hand, the pressure excess spreads out the ascending flows to the outside of the granule, resulting in that the periphery of granule obtains high intensity. A dark feature is newly formed at the high-density region and it is developed over the line formation height. As the dark feature is developed with time, it finally split the old granule into some smaller cells.

However, there are less numbers of observations discussing the fragmentation mechanism. Using time sequences of intensity and velocity field, a few researchers have tried to capture how granules are fragmented. By having ground-based observations with Vacuum Tower Telescope at Tenerife, Hirzberger et al. (2001) studied the intensity and velocity structures observed in 30 fragmented granule. In the fragmented area, velocity field gradually changes to downward with decreasing intensity. By analyzing three absorption lines formed at different heights, Berrilli et al. (2002) detected not only that the intensity decreases in the fragmented region, but also occurrence of upflows in the surrounding area of it. Their data was captured with THEMIS at Tenerife. These works have tried to capture the time evolution of vertical velocity structure. However, they could not identify the successive variation of velocity over height, owing to low time resolution. From another point of view, based on *Sunrise* observations, which is a 1-m aperture balloon-borne telescope, Palacios et al. (2012) insists that magnetic field appears newly in intergranular lane through the fragmentation.

Our results are compatible with the results from these previous studies. In fragmented area, intensity gradually decreases with time. The radiative cooling may cause the intensity to decrease. In addition, our results are compatible with the scenario of decreasing continuum intensity revealed by numerical simulations. The appearance of a high-density parcel in the fragmented area make high density material shift the level of $\tau = 1$ to higher layer. Since the temperature is lower at higher layer in the solar photosphere, it consequently leads to the reduced intensity there.

We found the new observational scenario of convective structure during fragmentation with high time cadence observations. In all cases, a downflow occurs at the top layer, and gradually descends to the bottom. The radiative cooling effectively works on materials at higher layer. Accordingly, downward motion is triggered at the top layer. After downward motion appears at the top, it takes less than 30 second to reach the bottom layer. The height between the continuum intensity and the line formation height is estimated around 300 km. The observed downward speed is less than 1km/s in all cases, and this speed is too small to arrive at the bottom in 30 second. It means, therefore, that velocity phase does not gradually propagate to the bottom. Rather, the radiative cooling becomes effective and forms a downward motion at the bottom layer with a short time delay.
In our examples, we did not detect significant character of the increasing intensity at the surrounding of the granules during the on-going fragmentation. Apparently, only one ex-

ample given in Fig. 4.18 shows increasing intensity in newly formed granules, while others do not show. In this study, we could not detect significant signal of increasing intensity, which is suggested by numerical simulations.

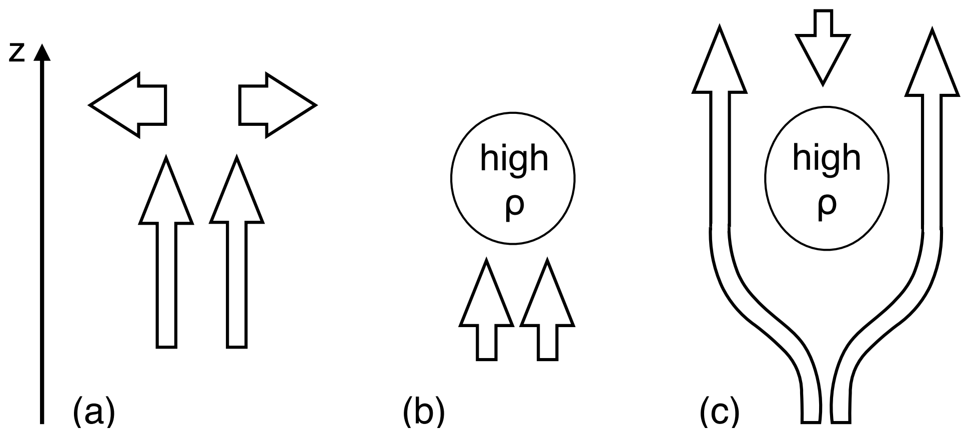

Figure 5.2: Schematic diagram of fragmentation mechanism. (a). Upflow continues to supply the materials and make a granule. These materials are pushed away horizontally. (b). Large granule cannot push out all supply from below the photosphere. High-density region occurs and prohibits upflow from penetrating. (c). High-density region cannot obtain the hot materials and radiative cooling causes downflow at the higher layer. At the same time, hot materials avoid the high-density region and ascend to periphery of granule.

Chapter 6

Summary and future prospects

In this study, we used the bisector analysis to investigate the vertical velocity structure of the gas convection in the solar photosphere. We separated both convective structure and 5-min oscillations from derived velocity field through the subsonic filter. Because we used the Fe I line at 630.15 nm, the vertical structure could be captured in the range roughly between 0 and 300 km in the photosphere.

Our results represent 3 points of convective structure: i) The time-distance velocity diagram shows that upflow velocity field in granule may be kept alive for the duration much longer than 10 minutes. ii) The number distribution of convective vertical velocities shows larger asymmetry toward the upward direction, as going to the higher portion of the photosphere. At higher layer, the RMS velocity observed in the pixels with the continuum intensity 10% or more brighter than the average is higher than 0.5 km/s, which is about 3 times faster than what is observed in the rest of the solar surface. iii) The RMS of downward velocity, in the continuum intensity 10% or more darker than the average, increases from 0.2 km/s to 0.6 km/s with depth.

The finding i) suggests that hot upward materials are successively supplied from below the photosphere, forming granules. According to ii) and iii), the following phenomenological picture is obtained: The strong upward velocity in bright granule reaches the higher portion of the atmosphere with less decreasing of the upward velocity, whereas the downflow in intergranular lane increases with depth. Convective motion in intergranular lane cannot be explained by mean atmospheric model in which the photosphere is a convective stable layer. One process can explain it: The cooling material tends to become a high-density and be pulled by gravity, causing acceleration of downflow. These dynamical properties of gas convection given in findings i) - iii) have not been investigated so far. In particular, we succeeded newly in founding the acceleration of downflow in interfranular lane, meaning the radiative cooling material behaves as the mentioned process.

Further interpretation of convective velocity needs to recognize the geometrical height where each intensity of Fe I 630.15 nm reflects on. In this study, we know only the mean height of the line core. Although the local temperature structure influences on each line formation height, an estimation of the mean geometrical height allows us to compare with the previous works in detail.

In the future, we will focus on at least two topics. One is an estimation of the energy that the 5-min oscillations give to the upper atmosphere. Sound waves may contribute to heating of the lower chromosphere. It is not easy to estimate the amount of the energy input by 5-min oscillations, because the propagation of phase velocity at different heights have not been identified significantly (Priest 2014). In this study, we captured the gradual increase of the amplitude of the 5-min oscillations along the vertical direction. If we detect the phase difference of the oscillatory signals observed at each height, we can know the phase velocity of the waves and may estimate how much energy the waves bring to the lower chromosphere.

Another study is understanding how the dynamics of convection give effects to the dynamics of magnetic flux tubes. In this study, we focused on the convection in the non-magnetic regions, in order to understand the behaviors of convection in case that no magnetic field exists in the atmosphere. The convection with magnetic field, i.e., magneto-convection, is more important for revealing the heating of the chromosphere and the corona. Recently, a numerical MHD simulation of the convection shows how the strong convective downflow beside a magnetic flux tube generates shocks and the waves propagating toward the upper atmosphere (Kato et al. 2011). The bisector analysis can be used to capture the dynamic evolution of downflows with the velocity structure in the vertical direction when they exist beside magnetic flux elements. Any progress of understanding the magneto-convection is a key for relating the dynamics of the convection to the energy transfer from the photosphere to the upper atmosphere. Such observing knowledge will significantly improve our understanding of the heating of the corona and chromosphere.

Appendix A: Velocity amplitude dependence on height at the downward

We directly investigate the velocity amplitude dependence on height. We concluded the fact that downflow is accelerated by using two results in section 4.2. One result of Fig. 4.10 shows, there are dominantly downward motion in less than continuum intensity of 0.9. The other result of Fig. 4.14 represents that RMS velocity less than 0.9 continuum intensity accelerating with depth. However, the RMS value includes both upward and downward flow. Here we more directly investigate those averaged values of convective velocity at each intensity level.

Fig. 6.1 shows the result of this analysis. Solid line in this figure shows averaged value of upward and downward flow respectively, and error bars indicate standard deviation at each intensity. It is difficult to determine the line center in our data set, the velocity measurement has an error bar of 0.16 km/s (section 2.2). We defined upward velocity as less than -0.16 km/s, while downward velocity more than 0.16 km/s. This figure shows that upward velocity decelerates from 0.65 km/s to 0.40 km/s with height, while downward velocity accelerates from 0.30 km/s to 0.50 km/s with depth.

We can directly conclude that downward flow accelerates with depth from this result.

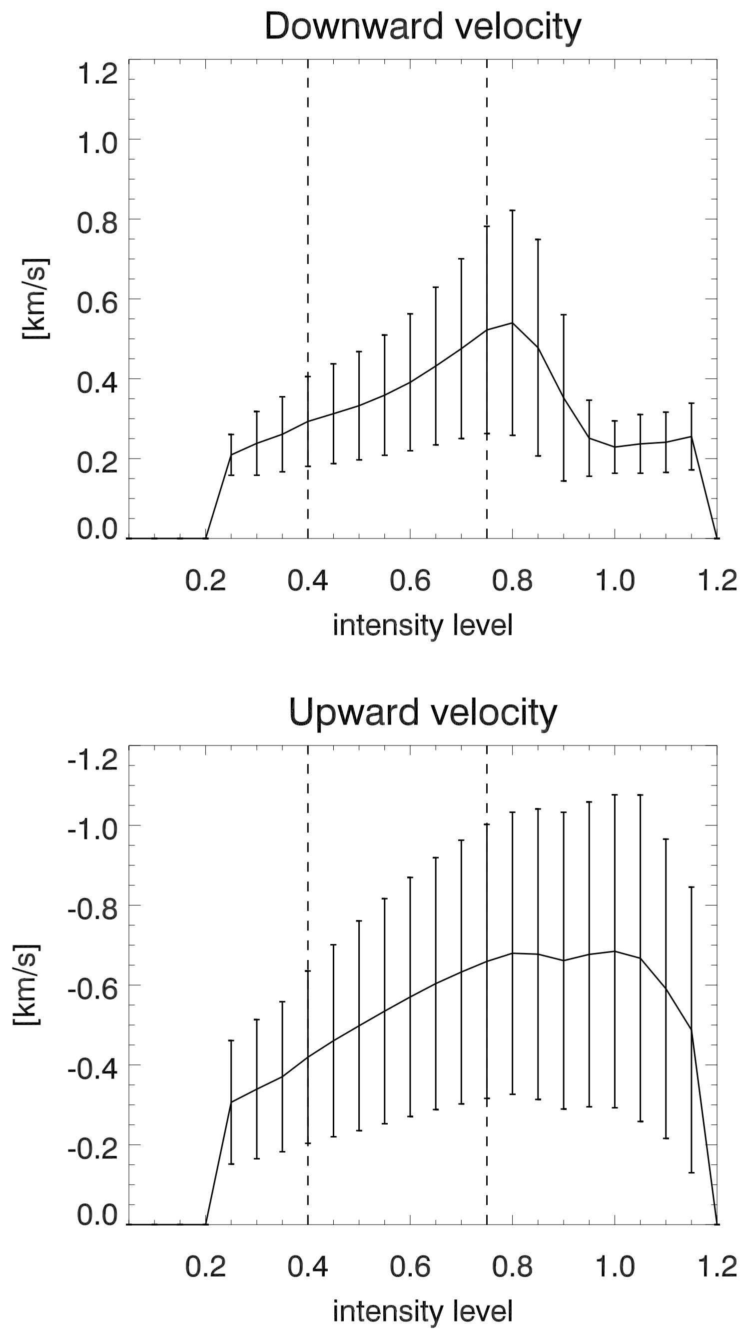

Figure 6.1: RMS of vertical velocity of upward and downward motion with height respectively. *Upper panel*: Downward velocity including more than 0.16 km/s of downflow speed. *Lower panel*: Upward velocity including less than -0.16 km/s of upflow speed. Error bars represent the standard deviation.

Appendix B: Results with different subsonic filtering

There is a possibility that the choice of subsonic filtering has a great effect on our results. We investigate the change of the results with different subsonic filtering here. Originally, we put the subsonic filtering 2 mHz and $\omega/k = 7$ km/s, 5-min oscillations components are above this frequency, and granulation components are below it. 5-min oscillations, however, are included in less than 2 mHz (Fig. 1.9). Hence, we change the boundary of 2 mHz to 1.5 mHz and see the different result. We do not change the boundary of $\omega/k = 7$ km/s, because there are weak powers in around this boundary. It is expected not to affect our results by changing that boundary.

We show the results corresponding to Fig. 4.8, 4.11, 4.13, 4.14, 4.18 and 6.1, which is connecting to main results and discussions. Fig.6.2 shows the time-distance velocity diagrams before and after with subsonic filter. Since remarkable change compared to Fig. 4.8 cannot be seen, original velocity field is transformed to convective velocity and 5-min oscillations successfully. Fig. 6.3 is the histogram at each intensity level for original, convective motion and 5-min oscillation velocity field. Histogram of convective motion indicates the strong asymmetry at the higher layer. That of 5-min oscillations become wider distribution with height, keeping symmetric shape. Those characters also can be seen in Fig. 4.11. Fig. 6.4 represents the dependence of the RMS of the original, the pure convection and 5-min oscillations velocity fields on the different intensity levels. The values of convective motion and 5-min oscillations are similar to that of Fig. 4.11. Fig. 6.5 shows the height dependence of the RMS velocities with different continuum intensities. The RMS of less than continuum intensity of 0.9 increases with depth. Their values are approximately same as Fig. 4.14. Fig. 6.6 indicates the time evolution of filtered convective structure in granular fragmentation. Although a weaker signals of downflow above the fragmented area in image 15 of this figure, the tendency that downward motion gradually changes from higher layer to lower layer remains unchanged. Fig. 6.7 shows the averaged values of convective velocity for upward and downward at each intensity level. Upward velocity decelerates from 0.65 km/s to 0.40 km/s with height, while downward velocity accelerates from 0.30 km/s to 0.50 km/s with depth. Their values are almost same as Fig.6.1.

From these comparisons, we can conclude that it does not show significant results changing the discussion.

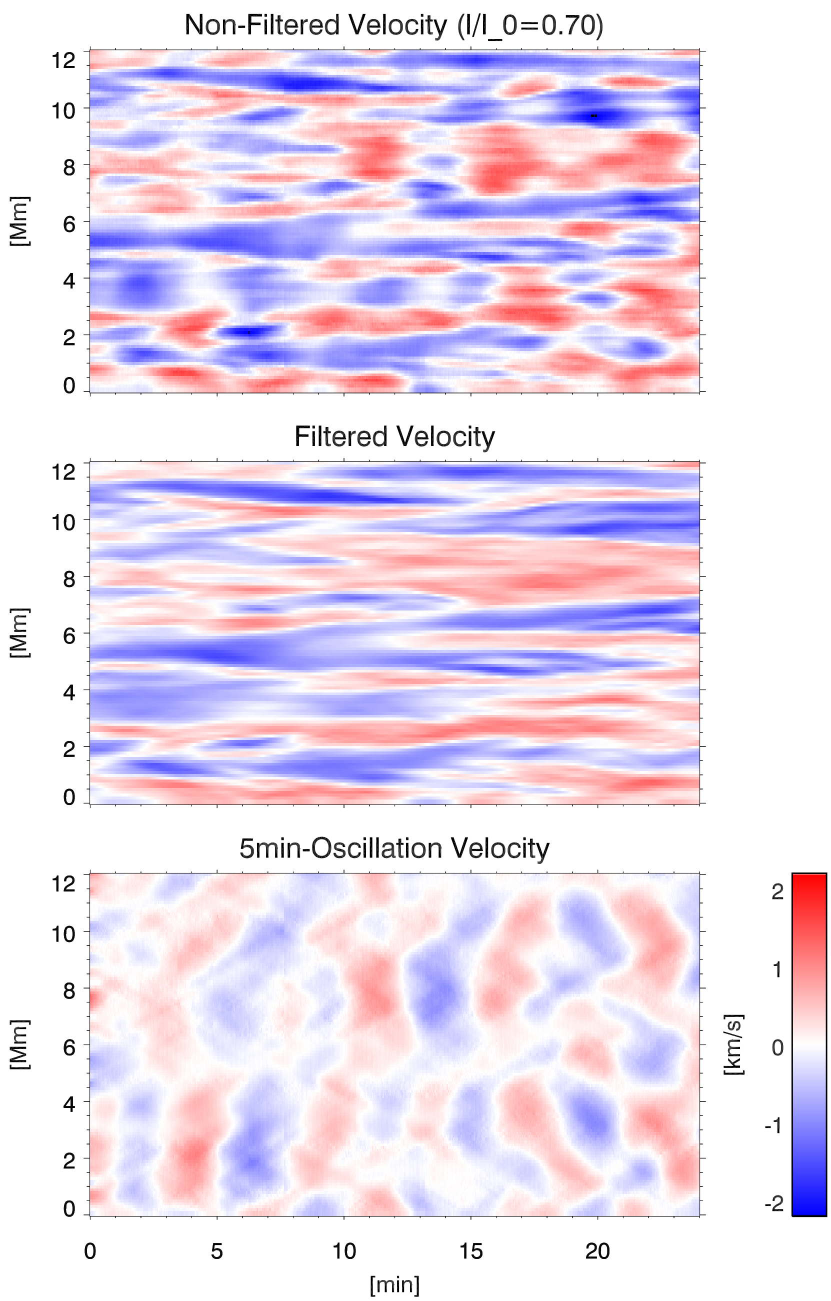

Figure 6.2: It is same as Fig. 4.8 but with the subsonic filtering of 1.5 mHz and $\omega/k = 7$ km/s.

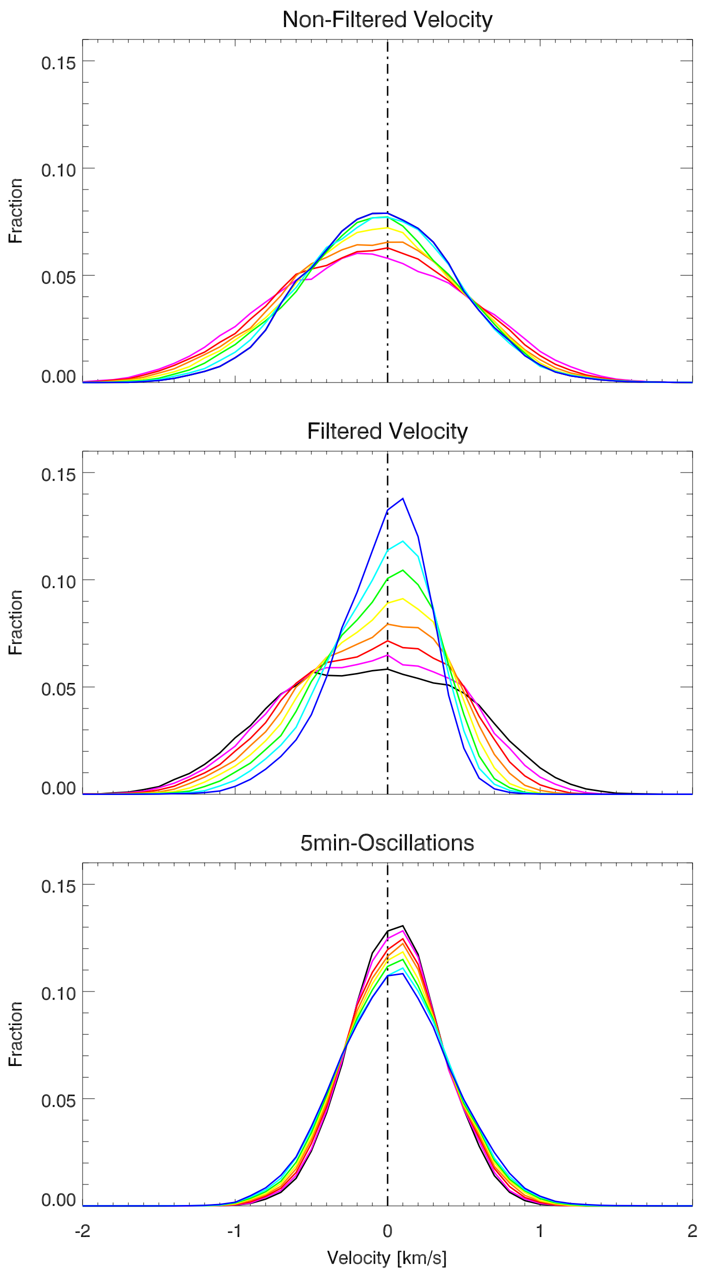

Figure 6.3: It is same as Fig. 4.11 but with the subsonic filtering of 1.5 mHz and $\omega/\mathrm{k} = 7$ km/s.

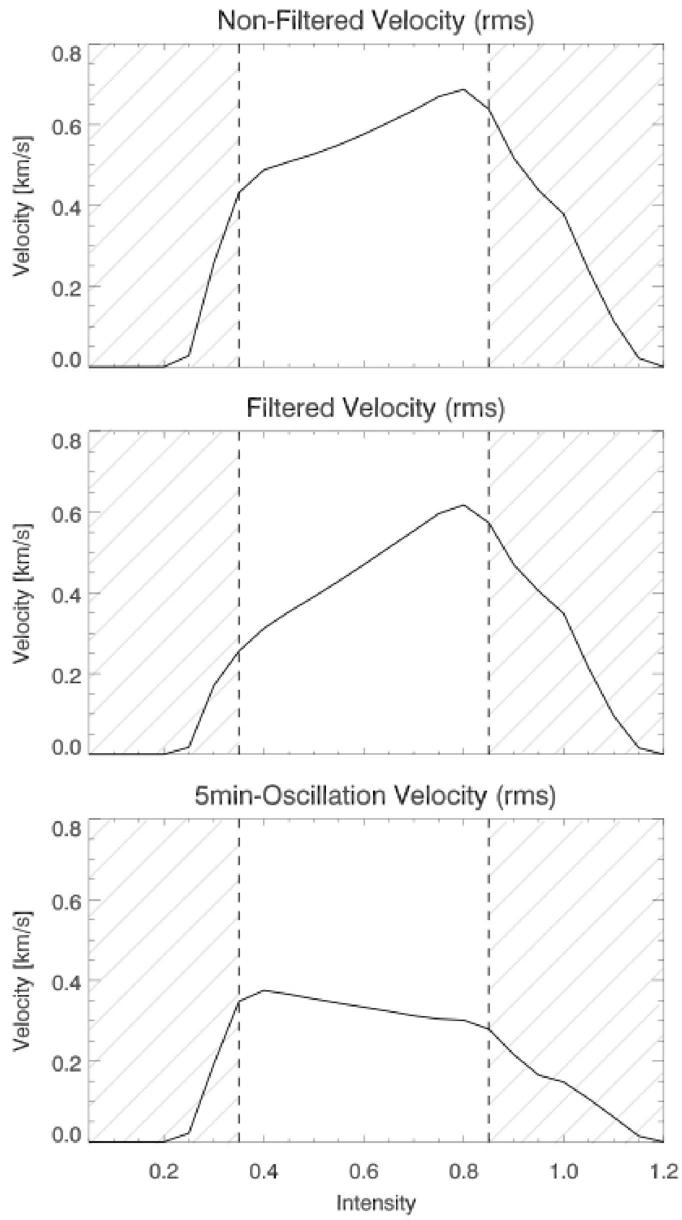

Figure 6.4: It is same as Fig. 4.13 but with the subsonic filtering of 1.5 mHz and $\omega/k =$ 7 km/s.

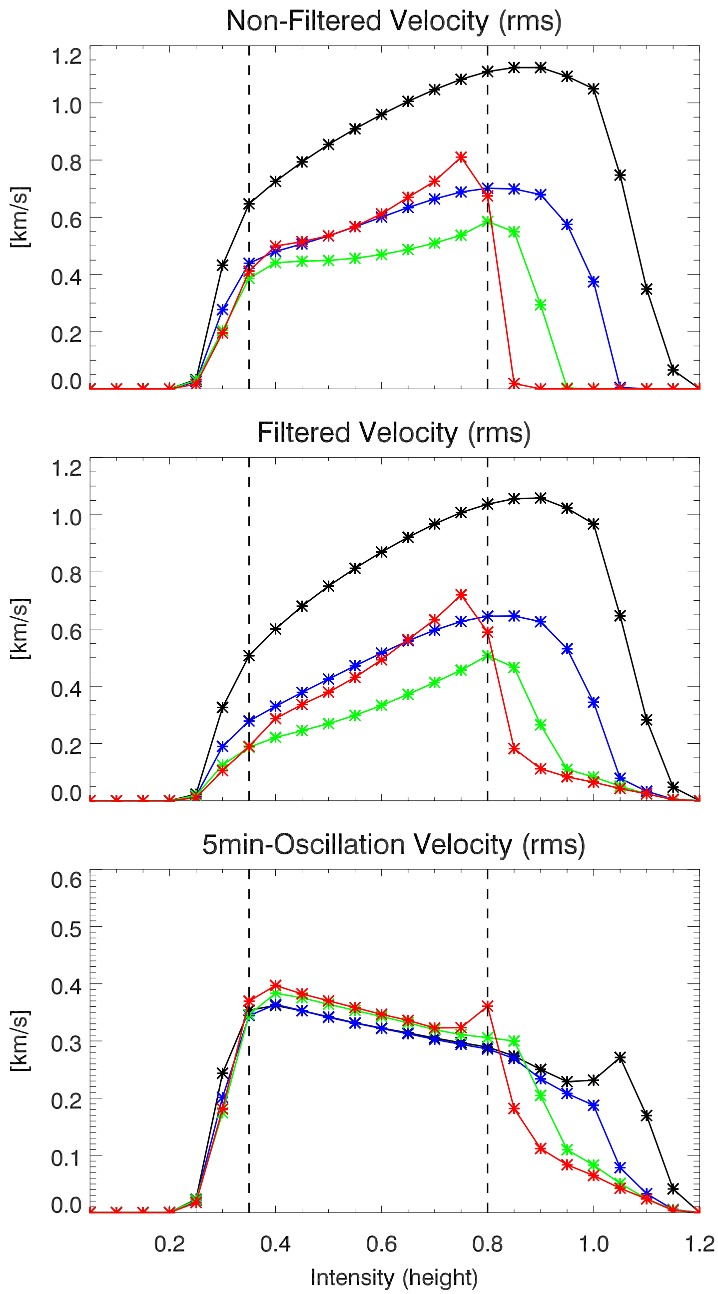

Figure 6.5: It is same as Fig. 4.14 but with the subsonic filtering of 1.5 mHz and $\omega/k = 7$ km/s.

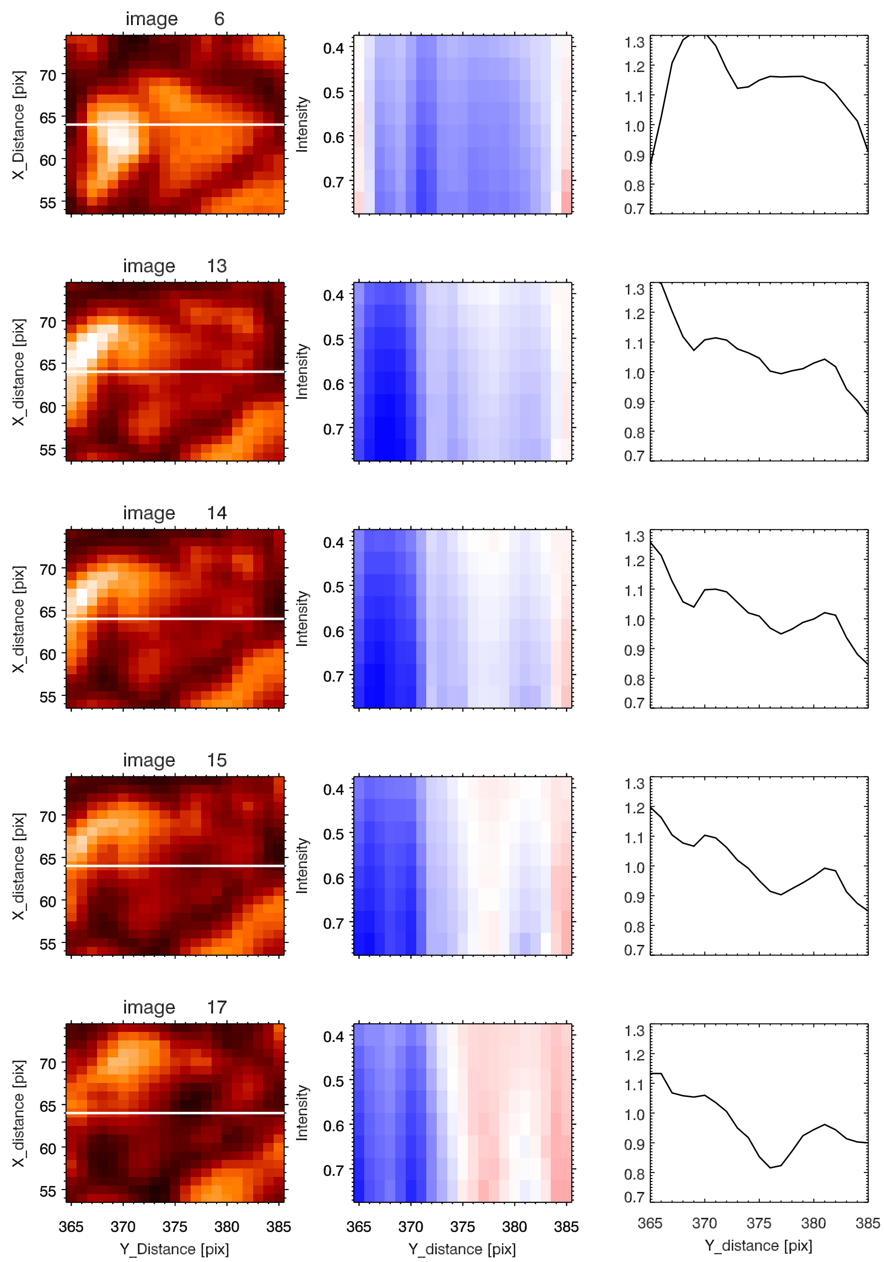

Figure 6.6: It is same as Fig. 4.18 but with the subsonic filtering of 1.5 mHz and $\omega/k = 7$ km/s.

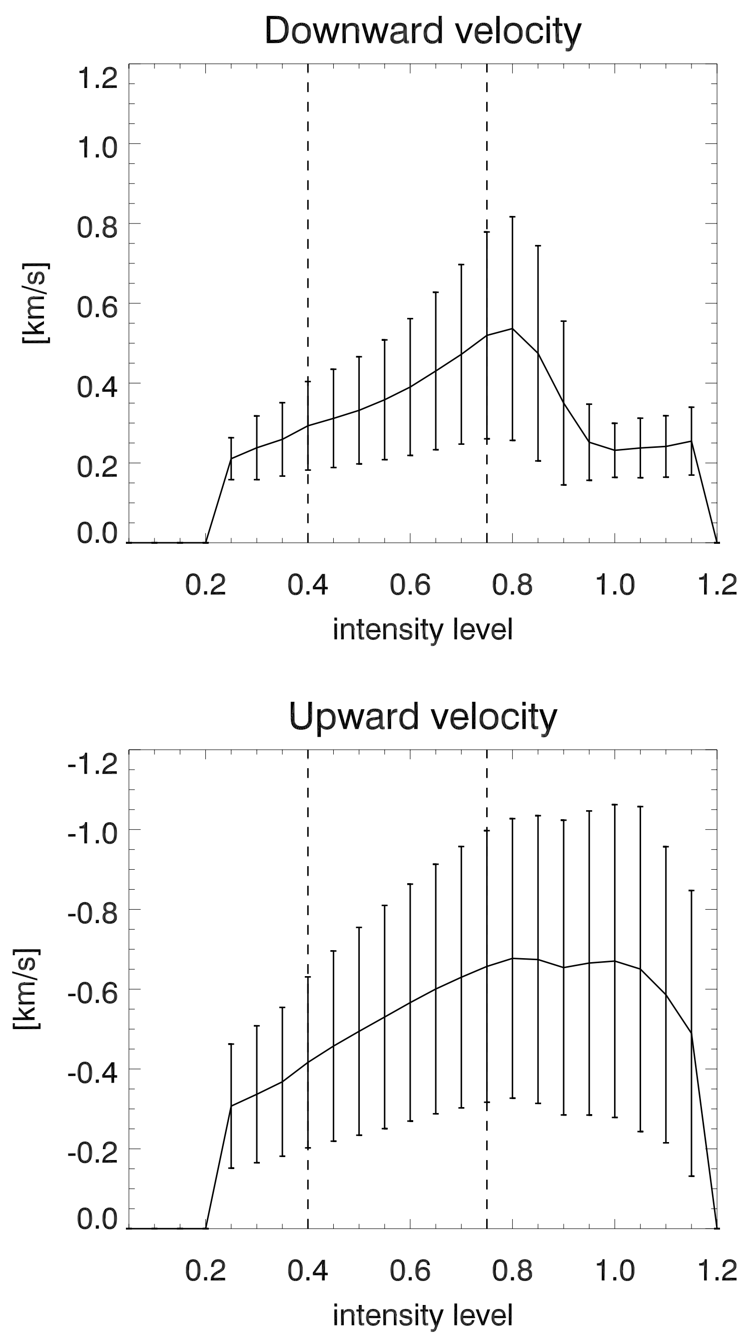

Figure 6.7: It is same as Fig. 6.1 but with the subsonic filtering of 1.5 mHz and $\omega/k =$ 7 km/s.

Bibliography

Berrilli, F., Consolini, G., Pietropaolo, E., et al. 2002, A&A, 381, 253

Berrilli, F., Florio, A., Consolini, G., et al. 1999, A&A, 344, L29

Deubner, F.-L. 1974, Sol. Phys., 39, 31

Dialetis, D., Macris, C., Prokakis, T., & Sarris, E. 1986, A&A, 168, 330

Dravins, D., Lindegren, L., & Nordlund, A. 1981, A&A, 96, 345

Durrant, C. J., Mattig, W., Nesis, A., Reiss, G., & Schmidt, W. 1979, Sol. Phys., 61, 251

Gray, D. F. 2008, The Observation and Analysis of Stellar Photospheres

Hirzberger, J., Bonet, J. A., Vázquez, M., & Hanslmeier, A. 1999, ApJ, 515, 441

Hirzberger, J., Koschinsky, M., Kneer, F., & Ritter, C. 2001, A&A, 367, 1011

Hirzberger, J., Vázquez, M., Bonet, J. A., Hanslmeier, A., & Sobotka, M. 1997, ApJ, 480, 406

Kato, Y., Steiner, O., Steffen, M., & Suematsu, Y. 2011, ApJL, 730, L24

Kiefer, M., Grabowski, U., Mattig, W., & Stix, M. 2000, A&A, 355, 381

Kostik, R., Khomenko, E., & Shchukina, N. 2009, A&A, 506, 1405

Kostik, R. I., & Khomenko, E. V. 2007, A&A, 476, 341

Kosugi, T., Matsuzaki, K., Sakao, T., et al. 2007, Sol. Phys., 243, 3

Leighton, R. B., Noyes, R. W., & Simon, G. W. 1962, ApJ, 135, 474

Lites, B. W., & Ichimoto, K. 2013, Sol. Phys., 283, 601

Lites, B. W., Akin, D. L., Card, G., et al. 2013, Sol. Phys., 283, 579

Maltagliati, L., & Righini, A. 2003, memsai, 74, 599

Palacios, J., Blanco Rodríguez, J., Vargas Domínguez, S., et al. 2012, ApJ, 537, A21

Priest, E. 2014, Magnetohydrodynamics of the Sun

Rast, M. P. 1995, ApJ, 443, 863

Roudier, T., Malherbe, J. M., Mein, P., et al. 2003, A&A, 409, 793

Roudier, T., & Muller, R. 1986, Sol. Phys., 107, 11

Rybicki, G. B., & Lightman, A. P. 1979, Radiative processes in astrophysics

Shimizu, T., Nagata, S., Tsuneta, S., et al. 2008, Sol. Phys., 249, 221

Stein, R. F., & Nordlund, Å. 1998, ApJ, 499, 914

Stix, M. 2004, The sun : an introduction

Suematsu, Y., Tsuneta, S., Ichimoto, K., et al. 2008, Sol. Phys., 249, 197

Title, A. M., Tarbell, T. D., Acton, L., Duncan, D., & Simon, G. W. 1986, Advances in Space Research, 6, 253

Title, A. M., Tarbell, T. D., Topka, K. P., et al. 1989, ApJ, 336, 475

Tsuneta, S., Ichimoto, K., Katsukawa, Y., et al. 2008, Sol. Phys., 249, 167

Ulrich, R. K. 1970, ApJ, 162, 993

Vernazza, J. E., Avrett, E. H., & Loeser, R. 1981, ApJS, 45, 635